

THE PHOTOCATALYTIC ACTIVITY OF PRASEODYMIUM DOPED
TITANIUM DIOXIDE

A THESIS SUBMITTED TO
THE GRADUATE SCHOOL OF NATURAL AND APPLIED SCIENCES
OF
MIDDLE EAST TECHNICAL UNIVERSITY

BY

DORUK DOĞU

IN PARTIAL FULFILLMENT OF THE REQUIREMENTS
FOR
THE DEGREE OF DOCTOR OF PHILOSOPHY
IN
MICRO AND NANOTECHNOLOGY

SEPTEMBER 2012

Approval of the thesis:

**THE PHOTOCATALYTIC ACTIVITY OF PRASEODYMIUM DOPED
TITANIUM DIOXIDE**

submitted by **DORUK DOĞU** in partial fulfillment of the requirements for the degree of **Doctor of Philosophy in Micro and Nanotechnology Department, Middle East Technical University** by,

Prof. Dr. Canan Özgen _____
Dean, Graduate School of **Natural and Applied Sciences**

Prof. Dr. Mürvet Volkan _____
Head of Department, **Micro and Nanotechnology**

Prof. Dr. Gürkan Karakaş _____
Supervisor, **Chemical Engineering Dept., METU**

Prof. Dr. Bilgehan Ögel _____
Co-Supervisor, **Metallurgical & Materials Eng. Dept., METU**

Examining Committee Members:

Prof. Dr. Hayrettin Yücel _____
Chemical Engineering Dept., METU

Prof. Dr. Gürkan Karakaş _____
Chemical Engineering Dept., METU

Prof. Dr. Deniz Üner _____
Chemical Engineering Dept., METU

Prof. Dr. Mehmet Parlak _____
Physics Dept., METU

Assist. Prof. Dr. H. Levent Hoşgün _____
Chemical Engineering Dept., Osman Gazi Univ.

Date: 21.09.2012

I hereby declare that all information in this document has been obtained and presented in accordance with academic rules and ethical conduct. I also declare that, as required by these rules and conduct, I have fully cited and referenced all material and results that are not original to this work.

Name, Last name: Doruk DOĞU

Signature:

ABSTRACT

THE PHOTOCATALYTIC ACTIVITY OF PRASEODYMIUM DOPED TITANIUM DIOXIDE

Dođu, Doruk

Ph. D. Department of Micro and Nanotechnology

Supervisor: Prof. Dr. Gürkan Karakaş

Co-Supervisor: Prof. Dr. Bilgehan Ögel

September 2012, 142 pages

In this study nanocrystalline TiO₂ was synthesized by a sol-gel process. The effect of praseodymium (Pr) doping and calcination conditions on the textural properties of nano structured particles and photocatalytic activity were examined. Samples were synthesized by hydrolyzation of titanium tetra isopropoxide (TTIP) and calcination at different temperatures. Characterizations of the samples were carried out using XRD, BET, XPS, TEM, and EDAX analyses. It was observed that anatase to rutile transformation is favored by higher calcination temperatures. The XRD analysis indicated that the anatase structure is stabilized by Pr doping and rutile phase formation at higher calcination temperatures is inhibited by the addition of Pr. It was also observed that Pr doping enhances the surface area and inhibit crystal growth. Phase stabilization effect of Pr doping was also confirmed by XPS results. EDAX analysis revealed that Pr is dispersed atomically in the crystal

structure. The Photoluminescence analysis by 325 nm excitation indicated the emissions at 608 and 621 nm which can be attributed by photon up-conversion. The photocatalytic activities of the samples were measured by methylene blue degradation and phenol mineralization reactions. The photocatalytic activities of the Pr doped samples were also found higher than undoped TiO₂ samples.

Keywords: Titanium dioxide, praseodymium, anatase, rutile, photocatalysis

ÖZ

PRASEODMIYUM İLE DOPINGLENMİŞ TİTANYUM DİOKSİTİN FOTOKATALİTİK AKTİVİTESİ

Doğu, Doruk

Doktor Mikro ve Nanoteknoloji Bölümü

Tez Yöneticisi: Prof. Dr. Gürkan Karakaş

Ortak Tez Yöneticisi: Prof. Dr. Bilgehan Ögel

Eylül 2012, 142 sayfa

Bu çalışmada sol-gel yöntemi kullanılarak nano yapıları TiO_2 sentezlenmiştir. Praseodymium (Pr) ile dopingleme ve kalsinasyon koşullarının nano yapıları parçacıklarının yapısal özellikleri ve fotokatalitik aktivitesi üzerindeki etkileri incelenmiştir. Örnekler titanium tetra izo-propoksitin hidrolizi ve çeşitli sıcaklıklarda kalsinasyonu ile üretilmiştir. Örneklerin karakterizasyonları XRD, BET, XPS, TEM ve EDAX kullanılarak yapılmıştır. Kalsinasyon sıcaklığındaki yükselmenin anatazdan rutil yapısına dönüşmeyi tetiklediği görülmüştür. XRD analizi anataz yapısının Pr eklenmesi ile dengelendiğini ve yüksek kalsinasyon sıcaklıklarındaki rutil faz transformasyonunu engellediğini göstermektedir. Pr ile dopinglemenin yüzey alanını arttırdığı ve kristal büyümesini engellediği de görülmüştür. Pr ile dopinglemenin faz dengeleyici özelliği XPS analizi ile de doğrulanmıştır. EDAX analizi Pr'nin kristal yapı içerisinde atomik olarak dağıldığını ortaya koymuştur. 325 nm

dalgaboyundaki uyarılma ile yapılan Fotoluminesans analizinde, foton yükseltmeyi işaret edebilecek, 608 ve 621nm'lerde ışımaya görülmüştür. Örneklerin fotokatalitik aktiviteleri metilem mavisini degradesyonu ve phenol mineralizasyonu reaksiyonları ile ölçülmüştür. Pr ile dopinglenmiş örneklerin fotokatalitik aktivitelerinin dopinglenmemiş TiO_2 örneklerine göre daha yüksek olduğu bulunmuştur.

Anahtar kelimeler: Titanyum dioksit, praseodymium, anataz, rutil, fotokataliz

To my family

ACKNOWLEDGEMENT

I would like to express my deepest gratitude to my supervisor Prof. Dr. Gürkan Karakaş for his inspiring academic guidance, valuable support, encouragement and patience. Not only he supported me academically but also helped me broaden my point of view in life.

I also wish to express my deep gratitude to my co-supervisor Prof. Dr. Bilgehan Ögel for his valuable support, encouragement and guidance. Besides his academic guidance he also helped me to change the way I comprehend the course of life.

Also I would like to greatly acknowledge my Ph.D. Examining Committee members, Prof. Dr. Deniz Üner and Prof. Dr. Mehmet Parlak for their enlightening comments and directions.

I should also thank Kerime Güney for her helps in activity test analyses and Necmi Avcı for XRD analyses. I also wish to thank Dr. Elif Tarhan Bor for her invaluable help with TEM analyses. I should also thank Saliha Kılıçarslan for surface area analyses, İlker Yıldız for XPS analyses, and Gizem Nogay and Mustafa Kulakçı for photoluminescence studies.

I like to acknowledge my former and present lab mates, especially Alp Yürüm, Bilal Bayram, Beril Korkmaz Erdural and Emre Yılmaz for supporting me with a nice and health working environment and their friendship. I would also like to thank Canan Şener, Zeynep Obalı, Kenan Cem Tokay, Seval Er and Gökhan Çelik for their helps and great friendship.

I want to extend my thanks to my colleagues from my company Vestel Defence Industry, especially my boss İbrahim Pamuk and my friends Derya Deniz, Burak Gençkan and Sıla Aksongur for their patience and their friendly approach.

I owe a special gratitude to my parents Timur Dođu and Gülşen Dođu for their great encouragement, support and assistance during my Ph.D studies and for raising me to become who I am today. Also I would like to thank my sister Burcu Yavuz, Esen Erkan and my whole family for always supporting and being with me.

Finally I would like to thank my wife Serap Dođu for her personal support, patience at all times and for her great encouragement.

TABLE OF CONTENTS

| | |
|---|-----|
| ABSTRACT..... | iv |
| ÖZ..... | vi |
| ACKNOWLEDGEMENT | ix |
| TABLE OF CONTENTS..... | xi |
| LIST OF TABLES..... | xiv |
| LIST OF FIGURES | xvi |
| CHAPTERS | |
| 1. INTRODUCTION | 1 |
| 2. LITERATURE REVIEW | 4 |
| 2.1. Semiconductors..... | 4 |
| 2.2. Titanium Dioxide | 7 |
| 2.3. Photocatalysis..... | 11 |
| 2.4. Methods to Improve the Photocatalytic Activity of TiO ₂ | 15 |
| 2.4.1. Electron Donors..... | 15 |
| 2.4.2. Carbonate Salts..... | 16 |
| 2.4.3. Noble Metal Loading | 18 |
| 2.4.4. Doping..... | 18 |

| | |
|--|----|
| 2.5. Photon Up-Conversion..... | 20 |
| 2.6. Photocatalytic Processes with TiO ₂ | 23 |
| 2.7. Synthesis Methods | 26 |
| 2.7.1. Sol-Gel Synthesis..... | 27 |
| 2.7.2. Other Synthesis Methods | 29 |
| 3. EXPERIMENTAL | 31 |
| 3.1. Preparation of Powder Samples | 31 |
| 3.2. Preparation of Thin Film Samples..... | 33 |
| 3.3. Characterization..... | 35 |
| 3.3.1. X-Ray Diffraction (XRD) | 35 |
| 3.3.2. Surface Area and Pore Size Distribution | 35 |
| 3.3.3. X-Ray Photoelectron Spectroscopy (XPS) | 35 |
| 3.3.4. Photoluminescence | 36 |
| 3.3.5. Photoresponse Experiments | 36 |
| 3.3.6. TEM Analysis | 37 |
| 3.4. Photocatalytic Activity Tests | 37 |
| 3.4.1. Methylene-Blue Degradation Test for Powder Samples..... | 37 |
| 3.4.2. Methylene-Blue Degradation Test for Thin Film Samples | 38 |
| 3.4.3. Phenol Mineralization Test for Powder Samples | 38 |
| 4. RESULTS AND DISCUSSION..... | 41 |

| | |
|---|-----|
| 4.1. Characterization..... | 41 |
| 4.1.1. X-Ray Diffraction | 42 |
| 4.1.2. Surface Area and Pore Size Distribution | 51 |
| 4.1.3. X-ray Photoelectron Spectroscopy (XPS) | 61 |
| 4.1.4. Photoluminescence | 69 |
| 4.1.5. Photoresponse | 71 |
| 4.1.6. TEM Analysis | 76 |
| 4.2. Photocatalytic Activity Tests | 82 |
| 4.2.1. Methylene-Blue Degradation Test for Powder Samples..... | 82 |
| 4.2.2. Methylene-Blue Degradation Test for Thin Film Samples | 87 |
| 4.2.3. Phenol Mineralization Test for Powder Samples | 91 |
| 5. CONCLUSIONS..... | 100 |
| APPENDICES | |
| REFERENCES | 103 |
| A. CALIBRATION STUDY OF UV_VIS SPECTROPHOTOMETER | 126 |
| B. TABULATED RESULTS OF EACH RUN | 134 |
| C. ANALYSIS OF REACTION TEST RESULTS IN TERMS OF REACTION RATE | 137 |
| CURRICULUM VITAE | 141 |

LIST OF TABLES

TABLES

| | |
|---|----|
| Table 1: Physical properties of different TiO ₂ crystal phases [59]..... | 10 |
| Table 2: The compositions and calcination temperatures of powder samples. | 33 |
| Table 3: Main absorption wavelengths of the species during the reaction ... | 39 |
| Table 4: XRD peaks of anatase and rutile with copper source | 43 |
| Table 5: The effect of calcination temperature on crystal structure; the XRD analysis of TiO ₂ and 1%Pr-TiO ₂ samples..... | 46 |
| Table 6: Crystallite sizes for the TiO ₂ and 1%Pr-TiO ₂ samples; The effect of calcination temperature..... | 47 |
| Table 7: Interplanar spacing and for some peaks of anatase in XRD diffractograms. | 50 |
| Table 8: Interplanar spacing for some peaks of rutile in XRD diffractograms. | 50 |
| Table 9: Surface area results of the samples..... | 52 |
| Table 10: Pore volume and diameter results of the samples | 53 |
| Table 11: XPS detailed scan energy intervals | 62 |
| Table 12: Band Gap Energies for the catalysts..... | 75 |
| Table 13: The principal X-Ray emission energies..... | 79 |

| | |
|--|-----|
| Table 14: Rate constants for the disappearance of phenol..... | 99 |
| Table 15: Calculated amounts of species formed during phenol mineralization reaction with TiO ₂ calcined at 500°C..... | 134 |
| Table 16: Calculated amounts of species formed during phenol mineralization reaction with 1%Pr-TiO ₂ calcined at 500°C..... | 134 |
| Table 17: Calculated amounts of species formed during phenol mineralization reaction with TiO ₂ calcined at 600°C..... | 135 |
| Table 18: Calculated amounts of species formed during phenol mineralization reaction with 1%Pr-TiO ₂ calcined at 600°C..... | 135 |
| Table 19: Calculated amounts of species formed during phenol mineralization reaction with TiO ₂ calcined at 650°C..... | 136 |
| Table 20: Calculated amounts of species formed during phenol mineralization reaction with 1%Pr-TiO ₂ calcined at 650°C..... | 136 |
| Table 21: -ln(C/C ₀) vs. time data for phenol..... | 137 |

LIST OF FIGURES

FIGURES

| | |
|--|----|
| Figure 1: Band structures of conductors, insulators and semiconductors | 6 |
| Figure 2: Direct and indirect band gap structures | 7 |
| Figure 3: Crystal structures of a) rutile, b) anatase, c) brookite [59]..... | 10 |
| Figure 4: Photoinduction of a TiO ₂ particle [66]..... | 12 |
| Figure 5: Band Gap structures of n-type and p-type semiconductors | 19 |
| Figure 6: Photon up-conversion; ground state absorption (GSA) process followed by an excited state absorption (ESA)..... | 21 |
| Figure 7: Photon up-conversion; co-operative sensitization, co-operative luminescence | 22 |
| Figure 8: Process scheme of sol-gel synthesis [205]..... | 28 |
| Figure 9: Synthesis procedure for powder catalyst samples..... | 32 |
| Figure 10: Dip coating apparatus..... | 34 |
| Figure 11: Reaction mechanism for the complete demineralization of phenol [67]..... | 40 |
| Figure 12: X-ray spectra for T400 and P400samples..... | 44 |
| Figure 13: X-ray spectra for T500 and P500 samples..... | 44 |
| Figure 14: X-ray spectra for T600 and P600samples..... | 45 |

| | |
|---|----|
| Figure 15: X-ray spectra for T650 and P650 samples..... | 45 |
| Figure 16: BET isotherm of TiO ₂ calcined at 400, 500, 600, 650°C | 54 |
| Figure 17: BET isotherm of TiO ₂ doped with 1%Pr calcined at 400, 500, 600, 650°C..... | 54 |
| Figure 18: BJH adsorption and desorption pore size distribution of TiO ₂ calcined at 400°C..... | 55 |
| Figure 19: BJH adsorption and desorption pore size distribution of TiO ₂ - Pr calcined at 400°C..... | 55 |
| Figure 20: BJH adsorption and desorption pore size distribution of TiO ₂ calcined at 500°C..... | 57 |
| Figure 21: BJH adsorption and desorption pore size distribution of TiO ₂ - Pr calcined at 500°C..... | 57 |
| Figure 22: BJH adsorption and desorption pore size distribution of TiO ₂ calcined at 600°C..... | 58 |
| Figure 23: BJH adsorption and desorption pore size distribution of TiO ₂ calcined at 650°C..... | 58 |
| Figure 24: BJH adsorption and desorption pore size distribution of TiO ₂ - Pr calcined at 600°C..... | 59 |
| Figure 25: BJH adsorption and desorption pore size distribution of TiO ₂ - Pr calcined at 650°C..... | 59 |
| Figure 26: XPS survey scan of Pure TiO ₂ and TiO ₂ -1%Pr calcined at 600°C | 62 |
| Figure 27: XPS Ti2p spectrum of Pure TiO ₂ and TiO ₂ -1%Pr calcined at 600°C | 63 |

| | |
|--|----|
| Figure 28: XPS O1s spectrum of Pure TiO ₂ and TiO ₂ -1%Pr calcined at 600°C | 63 |
| Figure 29: XPS Pr3d spectrum of Pure TiO ₂ and TiO ₂ -1%Pr calcined at 600°C | 64 |
| Figure 30: XPS Ti2p spectrum of TiO ₂ -20%Pr calcined at 500°C | 65 |
| Figure 31: XPS Pr3d spectrum of TiO ₂ -20%Pr calcined at 500°C | 65 |
| Figure 32: XPS O1s spectrum of TiO ₂ -20%Pr calcined at 500°C | 67 |
| Figure 33: O1s spectrum of TiO ₂ -20%Pr calcined at 600°C..... | 67 |
| Figure 34: XPS Pr4d spectrum of TiO ₂ -20%Pr calcined at 500°C | 68 |
| Figure 35: XRD spectrums of TiO ₂ -20%Pr catalysts calcined at 500, 600°C | 69 |
| Figure 36: Photoluminescence spectrums for T600 and P600 powder samples. | 70 |
| Figure 37: Photoluminescence spectrums for T600 and P600 thin film samples. | 71 |
| Figure 38: Photoresponse curves for different catalysts | 72 |
| Figure 39: Band gap calculation graph for direct band gap model | 73 |
| Figure 40: Band gap calculation graph for indirect band gap model | 74 |
| Figure 41: HRTEM photo of the catalyst containing 1%Pr and calcined at 600°C | 77 |
| Figure 42: HRTEM photo of the catalyst containing 20%Pr and calcined at 600°C | 78 |
| Figure 43: a) STEM image, Elemental mapping of 20%Pr-TiO ₂ b) Pr, c) Ti, d) Sum EDX spectrum | 80 |

| | |
|--|----|
| Figure 44: Point EDX analysis with 2nm beam for Pr and Ti with weight percentages; point 1: 77.5%Ti, 22.5%Pr, point 2: 87.8%Ti, 12.2%Pr, point 3: 76.1%Ti, 23.9%Pr, point 4: 3.3%Ti, 96.7%Pr. | 81 |
| Figure 45: UV-Visible Spectra of 2 ppm methylene blue solution | 83 |
| Figure 46: Methylene blue degradation on powder catalyst with time..... | 84 |
| Figure 47: UV-Visible Spectra at different times during the methylene blue degradation test over pure TiO ₂ catalyst calcined at 600°C | 85 |
| Figure 48: UV-Visible Spectra at different times during the methylene blue degradation test over 1%Pr-TiO ₂ catalyst calcined at 600°C. | 85 |
| Figure 49: UV-Visible Spectra at different times during the methylene blue degradation test over pure TiO ₂ calcined at 500°C. | 86 |
| Figure 50: UV-Visible Spectra at different times during the methylene blue degradation test over 1%Pr-TiO ₂ calcined at 500°C. | 86 |
| Figure 51: UV-Visible spectra of thin film catalysts | 87 |
| Figure 52: UV-Visible spectra of thin film catalysts after kept in 100ppm methylene blue solution for 24 hours | 88 |
| Figure 53: Normalized UV-Visible spectra of thin film samples kept in 100ppm methylene blue solution for 24 hours | 88 |
| Figure 54: Normalized UV-Visible spectra at different times during the methylene blue degradation test over T600 thin film catalyst | 89 |
| Figure 55: Normalized UV-Visible spectra at different times during the methylene blue degradation test over P600 thin film catalyst | 90 |
| Figure 56: Normalized UV-Visible spectra at different times during the methylene blue degradation test over T500 thin film catalyst | 90 |

| | |
|---|-----|
| Figure 57: Normalized UV-Visible spectra at different times during the methylene blue degradation test over P500 thin film catalyst | 91 |
| Figure 58: The initial UV-Vis spectrum of phenol and after 30 minutes reaction catalyzed by pure TiO ₂ catalyst calcined at 600°C under 300 W/m ² irradiation. | 92 |
| Figure 59: Absorbance at 270nm vs. reaction time for phenol mineralization reaction for 250 ml 20ppm phenol solution with 0.1g catalyst under 300 W/m ² irradiation. | 93 |
| Figure 60: Calculated amounts of species during phenol mineralization reaction for TiO ₂ catalyst calcined at 500°C | 93 |
| Figure 61: Calculated amounts of species during phenol mineralization reaction for 1%Pr-TiO ₂ catalyst calcined at 500°C | 94 |
| Figure 62: Calculated amounts of species during phenol mineralization reaction for TiO ₂ catalyst calcined at 600°C | 94 |
| Figure 63: Calculated amounts of species during phenol mineralization reaction for 1%Pr-TiO ₂ catalyst calcined at 600°C | 95 |
| Figure 64: Calculated amounts of species during phenol mineralization reaction for TiO ₂ catalyst calcined at 650°C | 95 |
| Figure 65: Calculated amounts of species during phenol mineralization reaction for 1%Pr-TiO ₂ catalyst calcined at 650°C | 96 |
| Figure 66: Reaction mechanism for the complete demineralization of phenol observed in the experiments | 98 |
| Figure 67: 10, 20ppm aqueous phenol solutions' UV-Vis spectrum..... | 126 |
| Figure 68: 10, 20ppm aqueous oxalic acid solutions' UV-Vis spectrum..... | 127 |
| Figure 69: 10, 20ppm aqueous maleic acid solutions' UV-Vis spectrum..... | 127 |

| | |
|--|-----|
| Figure 70: 10, 20ppm aqueous hydroquinone solutions' UV-Vis spectrum | 128 |
| Figure 71: 10, 20ppm aqueous fumaric acid solutions' UV-Vis spectrum .. | 128 |
| Figure 72: 10, 20ppm aqueous formic acid solutions' UV-Vis spectrum | 129 |
| Figure 73: 10, 20ppm aqueous catechol solutions' UV-Vis spectrum | 129 |
| Figure 74: 10, 20ppm aqueous benzoquinone solutions' UV-Vis spectrum | 130 |
| Figure 75: 10, 20ppm aqueous muconic acid solutions' UV-Vis spectrum. | 130 |
| Figure 76: $-\ln(C/C_0)$ vs. time graph for phenol of TiO_2 calcined at $500^\circ C$... | 138 |
| Figure 77: $-\ln(C/C_0)$ vs. time graph for phenol of 1%Pr- TiO_2 calcined at $500^\circ C$ | 138 |
| Figure 78: $-\ln(C/C_0)$ vs. time graph for phenol of TiO_2 calcined at $600^\circ C$... | 139 |
| Figure 79: $-\ln(C/C_0)$ vs. time graph for phenol of 1%Pr- TiO_2 calcined at $600^\circ C$ | 139 |
| Figure 80: $-\ln(C/C_0)$ vs. time graph for phenol of TiO_2 calcined at $650^\circ C$... | 140 |
| Figure 81: $-\ln(C/C_0)$ vs. time graph for phenol of 1%Pr- TiO_2 calcined at $650^\circ C$ | 140 |

CHAPTER 1

INTRODUCTION

Photocatalysts accelerates chemical reactions by utilization of photons and photocatalysis is an excellent way to perform many reduction and oxidation reactions at room temperature. Photocatalysis is found to be an economical and sustainable method for the removal of various pollutants from gas and liquid streams by oxidation such as aromatics, colorants, VOC's, CO etc. The reduction pathway can be used for NO_x abatement, artificial photosynthesis by CO₂ reduction into methane and direct water splitting into H₂ and O₂ by utilization of solar irradiation. On the other hand, the use of photocatalysis is not limited with chemical conversion. Many complex systems can be organized by structural design and photocatalysts can be used to obtain multifunctional products like self cleaning surfaces (windows, windshields, eye glasses, fabrics etc.), antimicrobial surfaces, dye sensitized photovoltaic cells, super hydrophilic or superhydrophobic surfaces sensors etc. [1]. The metal oxide semi conductors such as TiO₂, ZnO₂, and SnO₂ are the most widely studied photocatalytic materials. TiO₂ is the most available, non toxic, most stable and active material [2]. The irradiation of titania with photons having higher energy than its band gap results with the charge separation which is the promotion of valance band electrons to the conduction band energy [3]. The resulting electron-hole pairs (e⁻ - h⁺) have a potential to initiate many oxidation and reduction reactions by reacting with surface ad-species such as O₂, and H₂O to produce highly reactive free radicals. TiO₂ has three crystal phases that are rutile, anatase and brookite. Rutile and anatase are the mostly studied crystal phases of titania for photocatalysis.

Although rutile has a lower band gap than anatase (3.0 and 3.2 respectively), in general, anatase is considered to have higher photocatalytic activity than that of rutile [4]. The band gap of pure TiO₂ is between 3.0 – 3.2 eV which corresponds to 413 – 388 nm wavelength in UV radiation which exists in small fraction of solar radiation. The transport of electrons and holes into the surface is limited with transport properties of crystals such as mobility, charge carrier density, particle size etc. and only a small fraction of electrons and holes reach to outer surface. The electron-hole recombination reaction occurs in crystal defects, impurities, grain boundaries etc. Therefore, the photon efficiency of pure metal oxide semiconductors are usually low and only 1 to 10% of photons absorbed can produce free radicals. On the enhancement of photon efficiency, the simplest approach is the synthesis of nanostructured semiconductor metal oxides with shorter diffusion length. The use of sol-gel method offers good alternatives on the synthesis of nanostructured materials by bottom to up approach. Doping semiconductor with metals and metal oxides is another solution to enhance photon efficiency by the utilization of photons from visible light range of the solar spectrum. Metals can also act as electron or hole traps that would decrease the electron-hole recombination rate [5]. The use of organic sensitizers, sacrificial agents and photon up conversion methods are the recent advanced methods on the field. The use of metal dopants to absorb higher wavelength photons in visible light and emission of photons in UV region by photo-luminescence can be an efficient method to enhance efficiency.

In this study, titanium dioxide photocatalysts have been synthesized by sol-gel method. The effect of praseodymium doping and calcination temperature on the structure and the photocatalytic activity of titanium dioxide had been examined. Catalyst samples in the form of powder and thin films had been synthesized and tested. For characterization of the catalysts synthesized; XRD, BET, XPS, photoluminescence, photoresponse, SEM and EDS had been used. To test the photocatalytic activities of the samples three different activity tests had been conducted. Methylene blue degradation test had been

made over powder and thin film samples to examine the photocatalytic activity of the catalysts to degradation of methylene blue. Also photocatalytic activities of the catalysts synthesized had been tested by phenol demineralization test.

CHAPTER 2

LITERATURE REVIEW

2.1. Semiconductors

Materials are classified as conductors, semiconductors, and insulators according to their electrical conductivity. Conductors are materials that have high electrical conductivity on the order of $10^7 (\Omega\text{m})^{-1}$. Opposite to conductors, materials that have a very low electrical conductivity that are lower than $10^{-10} (\Omega\text{m})^{-1}$ are named as insulators. Semiconductors lie between insulators and conductors and their conductivities are generally between 10^{-6} to $10^4 (\Omega\text{m})^{-1}$ [6].

Any element or compound, electrons have specific energy bands. Valence band (E_{VB}) is the energy band that contains the highest energy electrons, last orbital occupied by an electron, and the next higher energy band is called conduction band (E_{CB}). The energy gap between these two energy states is named as band gap and its magnitude is called the band gap energy (E_g). Electrons are forbidden to exist between valence and conduction band energy levels. The Fermi energy level is defined as the energy level at which the probability of occupation by an electron is 0.5. Electrons above the Fermi level can be used in electrical conduction. Fermi level can be calculated by;

$$E_F = \frac{1}{2}(E_{VB} + E_{CB}) + \frac{1}{2} \left(kT \ln \frac{N_{VB}^*}{N_{CB}^*} \right) \quad (1)$$

Where k is the Boltzmann constant, T is the temperature, N_{VB}^* and N_{CB}^* are the effective density of energy states function in the valance and conduction bands [7]. Conduction is obtained by the movement of free electrons in conduction band that is above the Fermi level. In conductors highest occupied energy level is near the middle of an energy band and Fermi level is that level. By application of a potential a current can be obtained because there are plenty of vacant levels at higher energies into which electrons can be raised.

On the other hand, for insulators and semiconductors, adjacent empty states to the highest occupied energy level (valance band). There is a band gap between the valance band and the conduction band and the Fermi level for this kind of band structure lies in the band gap. Electrons should absorb energy higher than the band gap to be excited to the conduction band. Electrons in insulator are strongly bonded to the atom and high amount of energy is needed to excite the electron to the conduction band meaning the band gap is very wide. For semiconductors, the main difference from insulators is that the band gap is narrower, so that an electron can be excited to the conduction band by absorbing a photon with energy higher than the band gap energy (E_g) to achieve conductivity. Lower the band gap in the band structure for a semiconductor, higher the probability that a valance electron can be promoted into the conduction band meaning more conduction electrons and higher electrical conductivity. Excitation of an electron leaves an empty space in the valance band that is called hole (h^+). The conductivity is achieved by these electron and holes. Also these electron hole pairs can be used in photocatalytic reactions.

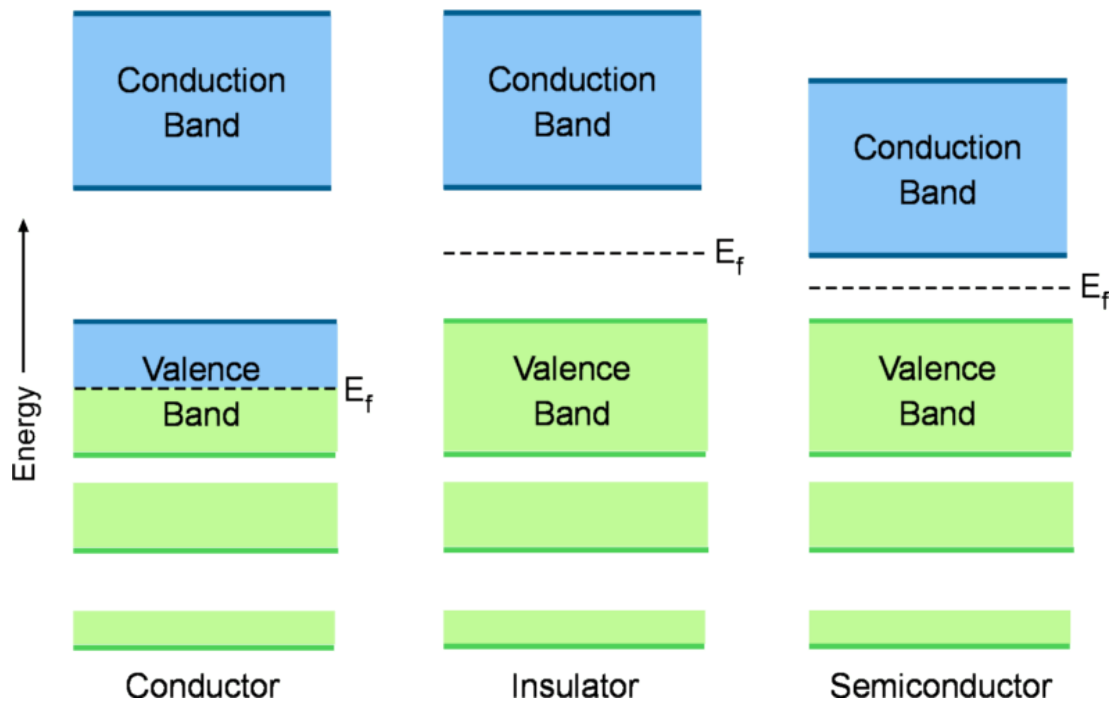


Figure 1: Band structures of conductors, insulators and semiconductors

There are two types of band gaps; direct band gap and indirect band gap. For direct band gap, the momentums of electrons and holes at valence and conduction bands are equal to each other, and electron can be excited to the conduction band by just absorbing a photon. If the momentums at valence and conduction bands are not equal to each other, it is called indirect band gap, and in this kind of band structure besides photon, a change in the momentum of the electron is also needed for the excitation from the valence band to the conduction band. This momentum change can be supplied by the crystal lattices. The vibration energy of atoms in the crystal is called phonons. The excitation of electrons to the conduction band, for an indirect band structure, includes absorption or emission of phonons that provide the momentum change needed by the electron for the excitation.

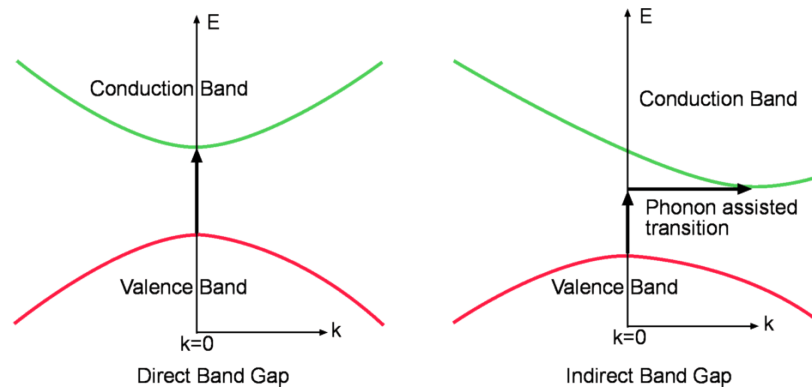


Figure 2: Direct and indirect band gap structures

Among semiconductors, titanium dioxide attracts significant interest especially on photocatalysis because of its excellent photo-chemical stability, low cost and non-toxicity. Titanium dioxide is the most active photocatalyst, and is used extensively in both laboratory and pilot plant studies [8].

2.2. Titanium Dioxide

Titanium dioxide is a non toxic semiconductor metal oxide, which is extensively used as pigment and filler to gain white color in paints, plastics, medicines, toothpastes, foods, etc. It is also used as UV absorber in cosmetic and skin care products. In recent years, nanostructured titania has attracted significant attention because of its photocatalytic property in applications involving removal of organic and inorganic pollutants from air and water, killing of cancer cells and bacteria, photovoltaic material for harvesting of solar energy, photoreduction of N_2 or CO_2 , and as a dielectric material for ultra thin capacitors [1]. Photocatalytic activity of anatase TiO_2 can be used in various processes such as odor elimination from drinking water, degradation of oil spills in surface water systems, degradation of harmful organic contaminants such as herbicides, pesticides, and refractive dyes [9].

TiO_2 also functions as an excellent model catalyst for oxide materials [10, 11]. Titanium cations are present in a variety of different coordination environments and oxidation states [12]. The numerous surface valance

states are capable of interacting with adsorbed species in unique ways facilitating many different chemical reactions. It is mentioned that surface oxygen plays an important role in the state of the titanium surface atoms [11]. Fully oxidized surfaces show traits similar to transition metal complexes. Moreover, the fully oxidized surface has insulator properties with very low electrical conductivity. The removal of surface oxygen causes electron transfer into the 3d orbital. Therefore at non-zero temperatures, electrons can be thermally excited to the conduction band creating a more conductive surface. Surface oxygen can be removed creating vacancies via several methods: annealing in hydrogen, annealing in vacuum [10, 12-14], and sputtering under ultrahigh vacuum conditions [10, 12, 15, and 16]. This creates a useful material for catalytic [10, 11, 17-32] and gas sensing applications [33-38]. For example the trimerization of acetylene to benzene and other C₂ through C₆ alkynes requires Ti⁺² cations [12, 27, and 28]. The Ti⁺² (and lower oxidation) sites are capable of undergoing a two electron oxidation in a manner completely described using organometallic homogeneous catalysis. The catalytic reactions on TiO₂ surfaces occur at oxygen vacancies create measurable changes in the surface conductivity of a TiO₂ film [34, 36-38].

Titania has been known to have three crystal phases; brookite, anatase, rutile [39]. Rutile is the thermodynamically most stable phase and brookite is the most rare phase of titanium dioxide. Rutile and anatase has a tetragonal unit cell with titanium cations surrounded by an octahedron of 6 oxygen atoms, whereas brookite has an orthorhombic structure. Among these phases Rutile and Anatase phases have been used in most photocatalytic investigations and the photocatalytic activity of amorphous titania is negligible [40]. Anatase phase is metastable and has the greater photocatalytic activity; rutile has a high chemical stability but is less active [4, 41]. Besides, some TiO₂ with a large quantity of anatase and a small quantity of rutile exhibits a higher photocatalytic activity than in the pure anatase or rutile phases [42, 43]. Although rutile has the lowest band gap of 3.0 eV, where anatase has a

band gap of 3.2 eV, anatase phase shows higher photocatalytic activity due to reduced recombination of photogenerated electron-hole pairs [8, 44]. Kyriaki et. al. [45] observed that, the photocatalytic reaction rate over anatase TiO₂ is approximately 7 times higher than that of rutile TiO₂. They have reported that the conduction bands for rutile and anatase are slightly different leading a smaller band gap for rutile than anatase (3.02 and 3.23 eV respectively). The flat band potential of rutile coincides almost exactly with the NHE potential (H⁺-H₂ level), whereas, that of anatase is shifted cathodically by approximately 200 mV [46]. Hence, in the case of anatase TiO₂, a driving force for water reduction is available, while in the case of rutile TiO₂, the driving force for water reduction is very small. They have also observed that light absorption capacity of the anatase form at the near UV-region is significantly higher than that of rutile, whose absorption capacity is shifted to higher wavelengths [45]. The majority of authors reported that pure anatase shows higher photocatalytic activity than pure rutile [44, 47-52], but many studies can be cited showing mixed structure of anatase and rutile is more active than pure anatase [42, 43, 53, 54]. Zhao et. al. [54] studied the on the mixed anatase rutile catalysts. They have prepared catalysts with having different amounts of rutile by annealing at 800°C for different time intervals. Annealing for a longer time leads to a more rutile content and their study showed that mixed phase catalysts has higher photocatalytic activity than pure anatase up to a composition of 33% rutile. Above 33% rutile they have observed that the photocatalytic activity starts to decrease. The higher activity and light absorption capability of anatase can be also explained by the band gap structure but there is not a good agreement on this in the literature. Some authors suggest that rutile has a direct band gap of 3.06 and an indirect one of 3.10 eV and the anatase has only an indirect band gap of 3.23 eV [55, 56]. However, Reddy et. al. [57] contrary to other authors found that anatase catalysts synthesized have a direct band gap of 3.32-3.36. There have been reported values in the literature from 2.86 to 3.34 eV for the anatase phase, the differences being attributed to variations in the

stoichiometric of the synthesis, the impurities content, the crystalline size and the type of electronic transition [49, 57, and 58].

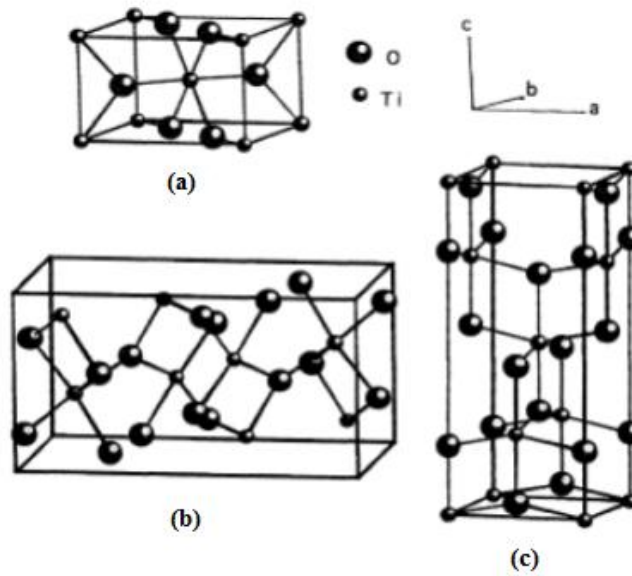


Figure 3: Crystal structures of a) rutile, b) anatase, c) brookite [59]

Table 1: Physical properties of different TiO_2 crystal phases [59]

| | Rutile | Anatase | Brookite |
|------------------------------------|---------------------------|---------------------------|-------------------------------------|
| Crystal structure | Tetragonal | Tetragonal | Orthorhombic |
| Lattice constants (\AA) | $a=4.5936$ $c=2.9587$ | $a=3.784$ $c=9.515$ | $a=9.184$ $b=5.447$ $c=5.145$ |
| Space group | $P4_2/mnm$ | $I4_1/amd$ | $Pbca$ |
| TiO_2 molecule/cell | 2 | 4 | 8 |
| Volume/molecule(\AA^3) | 31.216 | 34.061 | 32.172 |
| Density (g/cm^3) | 4.13 | 3.79 | 3.99 |
| Ti-O bond length (\AA) | 1.949 - 1.980 | 1.937 - 1.965 | 1.87 - 2.04 |
| O-Ti-O bond angle | $81.2^\circ - 90.0^\circ$ | $77.7^\circ - 92.6^\circ$ | $81.2^\circ - 90^\circ$ |

2.3. Photocatalysis

Photocatalysis is a process that modifies the rate of a chemical reaction in the presence of light. In semiconductors a photon can excite an electron in the conduction band to the valance band if it has a higher energy than the band gap energy of the material. The excited electron remains a hole in the valance band where it was before and electron itself behaves as a free electron. The electron and hole may migrate to the surface of the photocatalyst and react with adsorbed reactants [60]. Although there are several models in literature, the mechanism of photocatalysis on TiO_2 is not completely solved yet. In most of the processes, diffusion of electrons and holes to the surface is the rate determining process since electron hole recombination reaction takes place during this process. Photo-generated electron-hole pairs reported to combine in 1-25 μs depending on the reaction medium [61-62]. The excited electrons and holes can be used directly to drive a chemical reaction, which we call photocatalysis [63]. The surface atoms of TiO_2 are more active than the bulk atoms less adjacent coordinate atoms and unsaturated sites. Increased ratio of surface atoms to bulk atoms that can be achieved by increasing the surface area and the porosity of the catalyst, decreases the distance traveled to the surface by electrons and decreases the electron hole recombination [64]. The surface defects can act as hole traps in photocatalysis. With decreasing size, surface to volume ratio increases and the surface effect becomes more important [65].

In the presence of water or oxygen, redox reaction produces hydroxyl radicals that oxidize pollutants or can be used as anti-microbial agent [1].

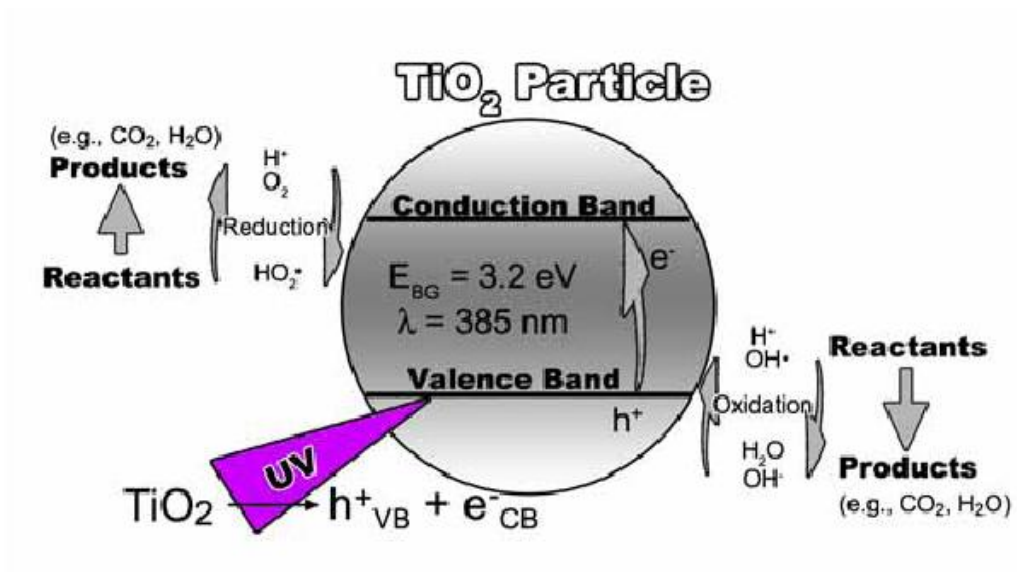


Figure 4: Photoinduction of a TiO₂ particle [66]

Rana et. al. [1, 3] gives a simple model for the TiO₂ photo catalyzed oxidation.

- (i) Charge carrier generation



- (ii) Surface trapping

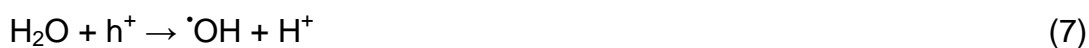


(iii) Recombination reaction



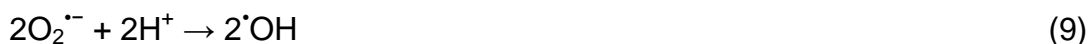
Over the surface of TiO_2 particles, the holes react with surface hydroxyl groups (OH^-) and adsorbed H_2O species to form $\cdot\text{OH}$ radicals;

(iv) Production of hydroxyl radicals



In the absence of electron or hole acceptors such as iron (III), manganese (IV), carbon dioxide the electron-hole recombination is possible according to eq. (3). The presence of oxygen prevents this recombination by trapping electrons through the formation of superoxide ions ($\text{O}_2^{\bullet-}$). The final product of the reduction may also be $\cdot\text{OH}$ radical and the hydroperoxy radical $\cdot\text{HO}_2$.





The performance of photocatalytic reactions is defined by the quantum efficiency or photon efficiency. Quantum efficiency is the ratio of photons used in the photocatalytic reactions to photons reaching to the photocatalyst surface. In photocatalysis formation of free radicals is followed by oxidizing the organic pollutants and these reactions are fast compared to the free radical formation and diffusion electron hole pairs on the surface [67]. So, quantum efficiency can be calculated by knowing the number of photons absorbed and the free radicals formed:

$$\text{Quantum Efficiency} = \frac{\text{Produced Radicals}}{\text{Absorbed Photons}} \quad (11)$$

Titanium dioxide can be excited by photons having higher wavelength than 388 nm which corresponds to the band gap 3.2 eV. Therefore UV light has the enough energy to excite electrons in the valance band to the conduction band. Only 4% of solar radiation energy is in UV light wavelength range (100 – 400 nm) which is very low compared with the visible light. This indicates a limitation in photon harvesting ability of titanium dioxide photocatalysts [68].

Another important process affecting the photocatalytic reactions rate is adsorption of the reactant to the surface of the catalyst. Adsorbed species on the surface can react with the electron and holes able to reach the catalyst surface without recombining and can decompose. A better adsorption of the species on the catalyst surface can be obtained by increasing the surface area and porosity, and modification of the catalyst surface. Also a meso porous structure is preferred.

Besides high surface area and porosity, crystallinity also affects the rate of photocatalysis. Although amorphous materials have a higher surface area, crystalline structures show much higher photocatalytic activities. To achieve high crystallinity, catalysts are heat treated at high temperatures. At high temperatures diffusion rate of the atoms in the catalyst increases and they can form an ordered crystal structure. However, during heat treatment sintering may occur in the catalyst and surface area may decrease. In addition to this heat treatment for a very long time at high temperature would lead anatase crystals in TiO_2 to transpose into rutile that may decrease the photocatalytic activity.

2.4. Methods to Improve the Photocatalytic Activity of TiO_2

There are several methods to improve the photocatalytic activity of titanium dioxide nanocrystals in the literature. Some of these methods are described in this section.

2.4.1. Electron Donors

Due to rapid recombination of photo-generated CB electrons and VB holes, it is difficult to achieve high photocatalytic using TiO_2 photocatalyst in distilled water. Adding electron donors (sacrificial reagents or hole scavengers) to react irreversibly with the photo-generated VB holes can enhance the photocatalytic electron/hole separation resulting in higher quantum efficiency. Since electron donors are consumed in photocatalytic reaction, continual addition of electron donors is required to sustain photocatalytic activity [5].

Hydrocarbons are widely used as electron donors, which can be oxidized by the holes at VB. EDTA, methanol, ethanol, CN₂, lactic acid and formaldehyde are some effective compounds to improve the photocatalytic activity [69-76]. On the other hand they may also yield pollutant CO₂ and CO gases which may not be favorable.

Inorganic ions such as S²⁻/SO₃²⁻ [77], Ce⁴⁺/Ce³⁺ [78] and IO₃⁻/I⁻ [79–81] are also used as electron donors in photocatalysis. Among these IO₃⁻/I⁻ is the most widely used one. I⁻ is the electron donor and IO₃⁻ is the electron acceptor and they work as a pair of redox mediators to scavenge holes and electrons respectively.

2.4.2. Carbonate Salts

Samaya et. al. [82-88] studied the addition of carbonate salts and showed that it improves the hydrogen production significantly. Addition of Na₂CO₃ was found to be effective for enhancement of hydrogen and oxygen production using Pt loaded TiO₂ (Pt-TiO₂) [82]. The IR spectra shows that the surface of the catalyst is covered by many carbonate species, as HCO₃⁻, CO₃⁻, HCO₃ and C₂O₆²⁻. They are formed by the following reactions:





Photo-generated holes react with carbonate species to form carbonate radicals and reduces the electron/hole recombination. Also proxycarbonates easily decompose into oxygen and carbon dioxide.



The evolution of CO₂ and O₂ promote desorption of O₂ from the surface which would reduce the chance of H₂ reacting with O₂ to form H₂O.

Addition of iodide was also found to be advantageous for hydrogen production [89]. I⁻ anion is preferentially absorbed on the Pt forming an iodine layer. This iodine layer is beneficial since it may suppress the formation of H₂O through the backward reaction of H₂ and O₂.

On the other hand, addition of carbonate salts and iodine should be made carefully. If they are added too much they may decrease the light absorption of the catalyst since they cover the surface. Also carbonate salts produce CO₂ which is a pollutant gas.

2.4.3. Noble Metal Loading

Noble metals, such as Pt, Au, Pd, Rh, Ni, Cu, and Ag are reported to improve the photocatalytic properties of titania. [74, 90-106]. The Fermi levels of these metals are lower than that of titania, and the excited electrons on titania can be transferred to the metal particles which decreases the electron/hole recombination rate. As electrons accumulate on the metal particles, their Fermi level shifts closer to the conduction band of titania [96, 98, 99], which is beneficial for photocatalysis. Also, if the metal particles are made smaller, Fermi level shifts more. Then electrons accumulated on the metals can react with the reactants increasing the photocatalytic activity.

2.4.4. Doping

When titania is doped with ions or oxides such as N, Fe, Ag, Na etc. Dopant can act as traps for holes and electrons. Doping may lead to an increase in the light-absorption capability by reducing the band gap. Dopants would also behave as electron or hole traps to decrease the electron-hole recombination rate. They may also improve photocatalytic activity by increasing the interfacial charge transfer rate.

Doping is introducing impurities in the structure of the semiconductor to modify its electrical properties. By doping, some energy states can be induced in the band gap of the semiconductor, making excitation of valance band electrons to the conduction band easier. For example a Group IV semiconductor such as silicon, germanium, and silicon carbide, can be doped with a Group III or Group V element to induce some defects in the crystal structure. Adding a Group V element such as phosphorus, arsenic, antimony in the structure of a Group IV semiconductor extra valance electrons are added that are not strongly bonded to the atoms. This type of

semiconductor is called n-type semiconductor and has a donor level in the band gap close to the valance band because of the extra valance electrons. On the other hand, doping Group IV semiconductors with Group III elements like boron, aluminium, gallium creates holes in the lattice structure and acceptor levels are formed in the band structure. This type of semiconductors is called p-type semiconductors.

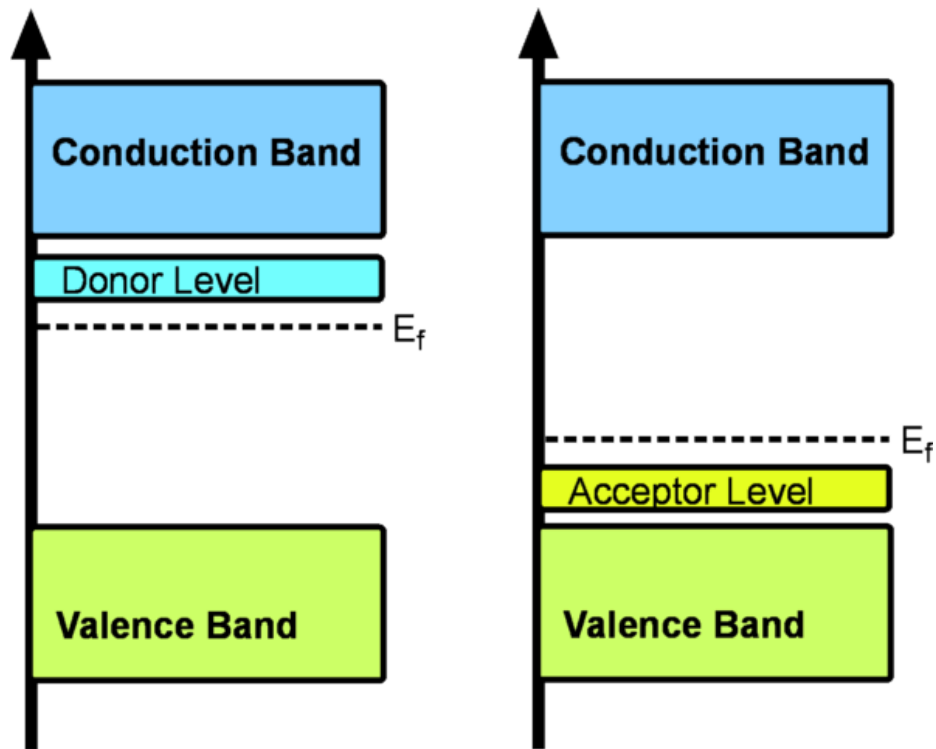


Figure 5: Band Gap structures of n-type and p-type semiconductors

There are some examples of doping of titania with metals such as Fe, Pd, Pt, Cr, rare-earth metals, etc. [107-111]. Araña et. al. [107] doped titania with Fe, Pd, Cu and observed enhancement on the photocatalytic activity for gas phase photocatalytic ethanol degradation. Wu et. al. [109] studied photo degradation of salicylic acid in water by using TiO_2 based catalysts, and showed that doping with Pd, Cr, and Ag would increase the photocatalytic activity of titania. Marinas et. al. [2] also studied on doping of titania with different metals and reported that Pd, Pt and Ag doping improves the

photocatalytic performance of TiO₂ for gas phase selective photo oxidation of 2-propanol.

Also, many researchers reported that Al₂O₃/TiO₂, ZrO₂/TiO₂, CdS/TiO₂, CdSe/TiO₂, ZnO/TiO₂, SnO₂/TiO₂, PbS/TiO₂, WO₃/TiO₂ and SiO₂/TiO₂ mixed oxides have higher photo-activity than pure TiO₂ [39]. Cheng et. al. [39] suggests that especially silica–titania nano-composites are more efficient photocatalysts than pure TiO₂. They tested the photocatalytic performances of titania doped with different amounts of silica by photo-degradation of methyl orange and concluded that 30wt. % silica shows the best performance.

Rane et. al. [112] claims that doping with N creates an induced mid-band level and titania can be made sensitive to visible light. N doping makes the white colored TiO₂ yellow, and this yellow TiO₂ has a band gap of 3.2 / 2.6 eV, where the band gap of white TiO₂ is 3.2 eV. This makes the UV absorption edge extending into the visible region while the white TiO₂ is transparent in this region. However, this reduced band gap would also increase the electron-hole recombination rate, and thus decrease the photocatalytic activity for photocatalytic oxidative degradation of 2-propanol reaction.

Scientists studied many metal ion and anion doping systems and their effects [113-146]. Doping is a very effective method in improving the photocatalytic activity of titania. Different ions can be used as dopants to improve the photocatalytic activity.

2.5. Photon Up-Conversion

Photocatalysts absorb light that has energy higher than its band gap. Doping may decrease the energy needed to excite an electron and cause a blue shift

in the U-Vis absorption spectrum of the catalyst sample. The photon up-conversion is the release of luminescence centre photons having higher energy than the energy of excitation photon [147]. So if a visible light can be transposed on a sample, photons emitted in the crystal can be used to excite conduction band electrons. In literature, there are limited publications on photon up-conversion [147-159] and none of them focused on photocatalysis.

There are several up-conversion mechanisms. The simplest and most widely applied UC mechanism involves ground state absorption (GSA) process followed by an excited state absorption (ESA) process as illustrated in Figure 6. GSA/ESA UC occurs when photons are absorbed sequentially within a single ion raising its energy to a higher energy state [148]. After the electron goes back to its ground state it emits a higher energy photon. Second mostly observed up-conversion mechanism is the energy transfer up-conversion. The energy transfer up-conversion (ETU) mechanism occurs when a nearby excited ion transfers its energy to a neighboring ion, also in an excited state raising it to a higher energy excited state. Co-operative process is another up-conversion mechanism which depends on the sensitization of the ion by two excited neighboring ions or combination of their luminescent energies (co-operative luminescence), as seen in Figure 7. The UC luminescence observed from these processes do not necessarily originate from the relaxation of an electron from a higher energy level [148].

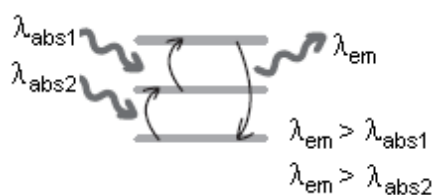


Figure 6: Photon up-conversion; ground state absorption (GSA) process followed by an excited state absorption (ESA)

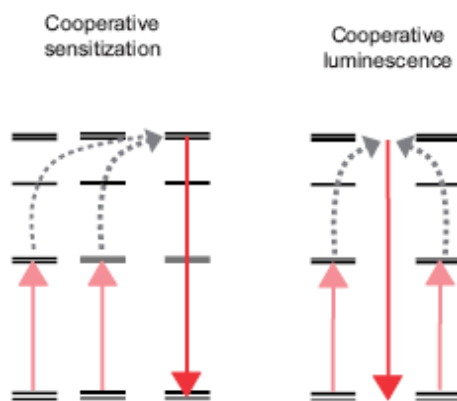


Figure 7: Photon up-conversion; co-operative sensitization, co-operative luminescence

Wenyue Su et. al. [160] synthesized TiO_2 incorporated with praseodymium (III) nitrate to make a visible light sensitive photocatalyst. They have seen that this photocatalyst has some photocatalytic activity under visible light whereas pure TiO_2 doesn't.

Amlouk et. al. [161] studied the luminescence of TiO_2 nanoparticles doped with Pr incorporated in silica aerogel. In the Photoluminescence spectra taken at different temperatures of the prepared sample with 2% Pr they have observed 2 peaks at 621 and 650 nm that may lead to photon up-conversion. Yang et. al. [162] showed Pr and N co-doped titania has higher photocatalytic activity than pure titania under visible light. Also Ranjit et. al. [163] observed that europium, praseodymium and ytterbium oxide doped TiO_2 shows significantly higher activity compared to the nonmodified TiO_2 catalyst.

Most promising photon up-conversion elements are praseodymium, erbium, europium, samarium and neodymium which are lanthanide group elements, and in this study they will be used to improve the photocatalytic properties of titania.

2.6. Photocatalytic Processes with TiO₂

In the studies of TiO₂ photocatalysis, many of them studied TiO₂ nanoparticles in suspension systems [164, 165]. But, as it is difficult to separate and recover TiO₂ particles in the suspension after the reaction, some groups began to work on immobilized TiO₂ films [166-168]. Also some studies have been focused on TiO₂ photocatalyst films [169]. Moreover, there are some studies focused on coating magnetic particles with TiO₂ that can be separated from the solution by applying a magnetic field [1, 9].

Photocatalysis by using TiO₂ is widely studied on decomposition of organic pollutants. A huge variety of organics, viruses, bacteria, fungi, algae, methylene blue, phenol, etc. can be successfully degraded to CO₂ and H₂O [17, 66, 67, 170-176].

Photocatalytic decomposition of phenol is one of the mostly studied photocatalytic processes on TiO₂ [67, 170-175]. Phenol (C₆H₅OH) is a common chemical that is used extensively in a variety of industrial applications [177]. Phenol concentration during the photocatalytic activity tests can be estimated using UV-Vis Spectrophotometer [178]. Decomposition of phenol takes place by complex reaction mechanism and according to the initial phenol concentration and catalyst properties, reaction follows various pathways. During phenol photodegradation, formation of intermediate species like hydroquinone and benzoquinone can be observed [178]. Arana et. al. [170] suggested two different mechanisms for phenol decomposition. At low phenol concentrations of 0.1g/L insertion of hydroxyl radicals increases the decomposition rate, whereas at higher concentrations (1g/L) insertion of hydroxyl radicals do not affect the decomposition rate as in low concentrations. UV-spectrums show that the reaction samples deviates significantly from that of pure aqueous phenol solution especially between the wavelength range of 310 to 400nm [67]. Possible intermediates that might be formed during the degradation of phenol are benzoquinone, hydroquinone, catechol, muconic acid, maleic acid, fumaric acid, oxalic acid

[179, 180]. B. Bayram [67] reported the specific peak of these compounds are at 246, 289, 271.5, 264, 211, 207, 222.5 nm respectively, and 270nm for phenol. He managed to develop a model for the calculation of amounts of species in a solution from UV-Vis spectrum by resolving UV-Vis characteristics of each species and using a computer program for the calculations. By this way, reaction mechanisms, rate limiting steps and the photocatalytic activity of the catalysts can be understood better for phenol mineralization.

There are many studies on photocatalytic decomposition of methyl orange [181] and dyes [182-183]. Neppolian et. al. [182] indicated that photocatalytic decomposition rates show significant difference for different dyes. Depending on the catalyst properties and the pH of the solutions there are three possible mechanisms for photocatalytic decomposition of dyes that are hydroxyl attack, direct oxidation by holes and direct reduction with electrons. Methylene blue is organic dye that is widely used in photocatalytic activity tests of TiO₂ [66, 176, 184] as probe molecule. It has been reported that methylene blue is degraded in aqueous dispersion of TiO₂ under UV illumination [185]. The advantageous special characteristics of methylene blue favor the monitoring of its decomposition upon illumination simple by measuring the concentration stages. The methylene blue concentration was determined by measuring the absorbance of the solutions at 666 nm by UV-Vis spectrometer [66]. Besides the characteristic peak of methylene blue at 666 nm, aggregation of methylene blue molecules at higher concentrations would lead extra peaks at 600 and 550 nm for dimers and for higher aggregates respectively [186]. Formation of these types of methylene blue aggregates highly decreases the photocatalytic degradation rate of methylene blue over TiO₂ crystals [187].

Surfactants are another important industrial pollutant. Studies on photocatalytic decomposition of some surfactants can also be sited in the

literature [188, 189]. Also it was reported that hydrogen sulfide that is highly toxic and pollutant can be decomposed by photocatalysis [190].

Another very promising reaction that can be achieved using TiO_2 photocatalyst is photocatalytic water splitting to produce hydrogen. Fujishima and Honda in 1972 [191] first showed that excited electrons on TiO_2 photocatalyst can react with water to produce hydrogen. Hydrogen is considered as an ideal fuel for the future [5]. It is thought as a clean energy source; however, 95% of hydrogen today is derived by fossil fuels, which means pollutant gases are formed during the production of hydrogen. This is because the alternative commercial process is water electrolysis that is too expensive. Photocatalytic water splitting is a promising solution to this problem since it is clean, cheap and environment friendly, renewable way of producing hydrogen gas. There are several studies found in the literature on photocatalytic water splitting to produce hydrogen [5, 59, 137, 192-198].

As for the inorganic contaminants, photocatalytic purification leads to deposition of environmentally harmful toxic metals on the surface of the semiconductor. Some photocatalytic purification studies about metal ions like Cu^{+2} , Hg^{+2} , Cr^{+6} and Pb^{+2} have been reported [199, 200]. Mechanism analysis of photocatalytic decomposition of nitrate on TiO_2 surface suggested that the major product of photo oxidation was nitrite [201].

For inactivation or removal of pathogenic organisms like bacteria, fungi or viruses photocatalytic disinfection is a promising alternative process [202]. It is reported that it is also possible to selectively kill organisms using TiO_2 [203].

2.7. Synthesis Methods

The functional properties of TiO_2 are strongly dependent on crystallinity, phase, particle size, surface area, pore size and distribution [66]. High surface area and porosity are important for any catalysts since the surface area directly affects the concentrations of active sites and surface adsorbed species. Titania synthesized by sol-gel method or chemical vapor deposition can have high surface area. Also titania can be synthesized physical vapor deposition, precipitation, hydrothermally, etc.

Low crystallinity (crystal to amorphous ratio) of titania coatings lead to a low photo-activity. To increase the crystallinity of titania, heat treatment under dry or hydrothermal conditions is considered essential. Rawat et. al. [68] compared the antibacterial properties of heat treated and not heat treated titania coated NiFe_2O_4 nanoparticles. The heat treatment was made at 400°C for 20 min and it was obviously seen that heat treatment increases the photo-activity of the material. However, extended heat treatment leads to the transformation of anatase to rutile phase [43, 45, 50, and 204]. Zhu et. al. [177] reported that with increasing temperature and heat treatment time rutile formation is observed. They have observed that increasing the calcination time from one hour to three hours at 600°C leads to starting of rutile formation. Also they have observed that after calcination in air at 700°C for 3 h, the sample displays a significant transformation of anatase into rutile phase, further calcination of the samples at temperatures above 800°C results in the total replacement of anatase by rutile phase for the TiO_2 materials. Su et. al. [204] observed that with increasing temperature and heating duration, the crystal size and simultaneously anatase to rutile transformation increases. Yu et. al [47] also studied on the effects heat treatment of TiO_2 on the photocatalytic activity. They have observed that by heat treatment phase transformation of titania powders from amorphous to anatase occurs. With increasing temperature and time, they have observed

that crystal size and pore size increased, whereas surface areas, pore volumes and porosity steadily decreased, and optimum heat treatment conditions have been found as 180°C for 10 hours for photocatalytic degradation of acetone. Jing et. al. [42] tested the effect of temperature on the crystal structure and photocatalytic activity by thermally treating the catalysts at 450, 550, 650°C for 2 hours. They have observed that increasing the temperature leads both increase in the crystallinity and anatase to rutile transition, and also reported that the highest activity for photocatalytic phenol degradation was achieved on the catalyst calcined at 550°C having 16.8% rutile in its composition. Another study on the heat treatment was made by Zhao et. al. [54]. They have annealed the catalysts at 800°C for 2, 5, and 10 hours. By annealing they have observed that rutile composition increases and the one annealed for 5 hours composed of 33% rutile shown the highest methylene orange degradation activity.

2.7.1. Sol-Gel Synthesis

Sol-gel method is widely used in the synthesis of metal oxides. By sol-gel method products with high homogeneity and purity can be obtained. Microstructural control of the nanoparticles and doping is easy by sol-gel synthesis. Moreover, the colloidal solution obtained by sol-gel enables several coating techniques like spin coating and dip coating. General process scheme of sol-gel synthesis is given in Figure 8.

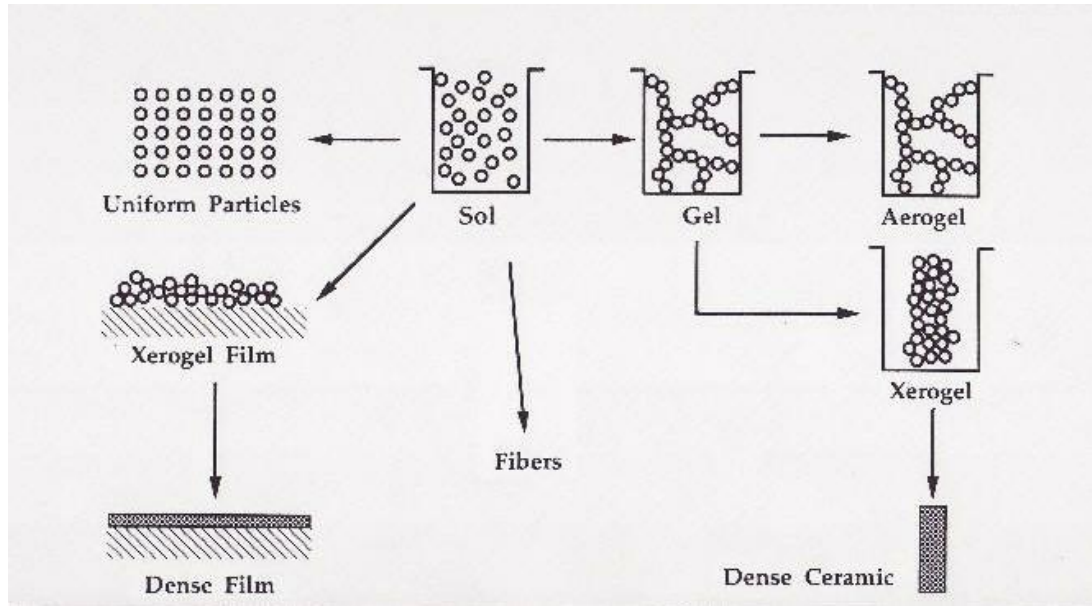
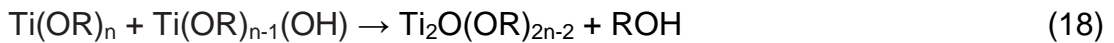


Figure 8: Process scheme of sol-gel synthesis [205]

Sol-gel methods are widely used in synthesis of TiO_2 . In the synthesis of TiO_2 by sol-gel method $\text{Ti}(\text{i-OP})_4$ and $\text{Ti}(\text{OBu})_4$ are the most commonly used precursors. Su et. al. [206] described the reaction mechanism in sol-gel synthesis of TiO_2 . The titanium precursor reacts with water (hydrolysis):



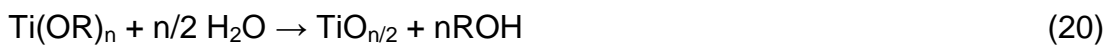
This reaction continues until the formation of $\text{Ti}(\text{OH})_n$. Then polymerizations reactions occur which are; condensation dehydration:



And dealcoholation:



The overall reaction is:



Condensation reactions pull the particles together into a compact form and build up the metal oxide crystal [207]. A network of gel is formed by the

gelation of the solute. Gelation is an important step since it controls the final product structure. After gel is formed, network loses water and alcohol, which causes gel to shrink and creates pores.

There are several factors affecting the morphology of TiO_2 . Type of precursor and chemical compounds in the sol-gel system are two of the important parameters. Aging is also a step that affects the final product. During aging further condensation of the partially condensed molecules occur and further cross links are formed. Aging time and conditions affects the final structure of the catalyst. Long aging times leads to an increase in the surface area and porosity of the catalyst and results in a stronger structure.

Drying time and conditions also affect the final structure of the catalyst. During drying water, alcohol and other volatile compounds are evaporated. If this is made too fast this may result in formation of high pressures in the pores and may lead to collapse of the cross-links formed.

After drying the material is amorphous and must be calcined to crystallize. Calcination is made under an oxidizing atmosphere. During calcinations hydrocarbons are burned out and the inorganic molecules diffuse to form ordered crystal structure. Calcination time and temperature is very important since it affects the crystal structure, phases and surface area of the catalyst. Low calcinations temperature and time leads to low crystallinity, whereas high calcinations temperature and time results in formation of rutile phase instead of the active anatase phase and also sintering and decrease in the surface area of the catalyst.

2.7.2. Other Synthesis Methods

Besides sol-gel synthesis there are several other methods for producing titanium dioxide. They will be explained briefly since their details are not in the focus of this study.

Hydrothermal synthesis is one of these methods. Hydrothermal synthesis can be a solution to high temperature heat treatment problem in sol-gel, because crystallization of nanoparticles can occur under autogenerated pressure during the hydrolysis process. Furthermore, the hydrothermal method is environmental friendly since the reactions are carried out in a closed system and the contents can be recovered and reused after cooling [208].

Another method is precipitation method, where hydroxides are precipitated by adding a solution to a raw material followed by calcination. The disadvantage of this method is the difficulty of controlling particle size and size distribution [66].

Also microemulsion method can be used in the synthesis of titanium dioxide nanoparticles. Some other methods that can be cited are chemical vapor deposition (CVD), physical vapor deposition (PVD), inert gas condensation, ion sputtering, spray pyrolysis, thermal plasma synthesis [209-214].

CHAPTER 3

EXPERIMENTAL

3.1. Preparation of Powder Samples

TiO₂ samples were prepared by sol-gel method. The hydrolysis was performed by drop wise addition of a solution containing 130 ml ethanol (J.T. Baker, CAS No: 64-17-5, Purity: 99.5%), 0.24 ml HCl (Acros Organics, CAS No: 7647-01-0, Purity: 37%) and 0.5 ml distilled water to the mixture of 8.4 ml titanium tetra-isopropoxide (TTIP) (Aldrich, CAS No: 546-68-9, Purity: 97%) and 20 ml of ethanol at 0°C under continuous stirring. The drop wise addition has special importance because of the fast reaction of titanium isopropoxide with water which leads to formation of large clumps and aggregates. After hydrolysis, solution was kept at 0°C for 30 minutes to ensure complete hydrolysis. Finally the solution was aged for 24 hours and colloidal solution was obtained. The aged solution was dried at 90°C in quartz cuvettes. The dried powder samples were calcined for 4 hours at 300, 400, 500, 600, 650°C under air flow. Praseodymium doped samples were prepared by the addition of appropriate amount of praseodymium(III) isopropoxide (Aldrich , CAS No: 19236-14-7) to obtain 1%, 5% and 20% Pr in the catalyst with respect to titanium. The samples, the Pr loading and calcination temperatures are given in Table 2.

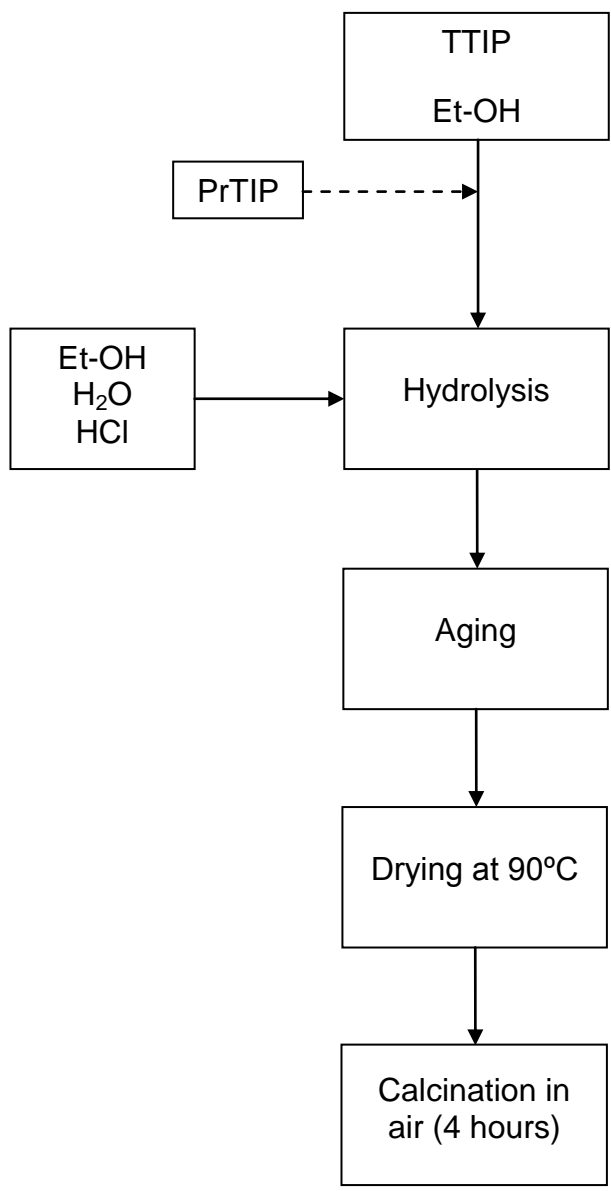


Figure 9: Synthesis procedure for powder catalyst samples

Table 2: The compositions and calcination temperatures of powder samples.

| Sample Code | Composition | Calcination Temp. (°C) |
|-------------|----------------------|------------------------|
| T300 | TiO ₂ | 300 |
| T400 | TiO ₂ | 400 |
| T500 | TiO ₂ | 500 |
| T600 | TiO ₂ | 600 |
| T650 | TiO ₂ | 650 |
| P300 | TiO ₂ -Pr | 300 |
| P400 | TiO ₂ -Pr | 400 |
| P500 | TiO ₂ -Pr | 500 |
| P600 | TiO ₂ -Pr | 600 |
| P650 | TiO ₂ -Pr | 650 |

3.2. Preparation of Thin Film Samples

The TiO₂ and Pr-TiO₂ thin films were obtained by coating pyrex microscope slide glasses. Microscope slides were cleaned before coating by washing with liquid detergent and rinsing with deionized water. After pre-cleaning, the slide glasses were etched by immersing in 1 molar NaOH (Merck, CAS No: 215-185-5, Purity: 97%) solution for 15 hours. The etching in alkali solution

enriches the glass surface with hydroxyl sites and improves hydrophilicity and wetting properties. The slides were rinsed with deionized water in ultrasonic bath 10 minutes dried at 120°C for 1 hour.

Aged colloidal solutions of TiO₂ and Pr-TiO₂ were prepared by following the same protocol for powder samples. The pre-cleaned and etched slide glasses were coated with colloidal solutions by dip coating (Figure 10). Coating was performed by immersing the slides into the solution at 2 cm/min speed, waiting for 1 minute and pulling it back by 1.2 cm/min. Coated glass plates were dried for 30 minutes at 110°C and the coating process was repeated 5 times to obtain desired thickness. After obtaining five consecutive layers of coating, the samples were calcined at 500 and 600°C for 15 minutes in air flow. Thin film samples of pure TiO₂, and 1%, 5% and 20% Pr-TiO₂ were prepared by the same protocol.



Figure 10: Dip coating apparatus

3.3. Characterization

3.3.1. X-Ray Diffraction (XRD)

X-Ray diffraction patterns of the samples were obtained by Rigaku D/MAX2200 diffractometer in METU Metallurgical and Materials Engineering Department. Diffractograms are taken between angles (2θ) of 20° to 80° by using Cu source ($\lambda=1.5405 \text{ \AA}$). The diffraction patterns obtained for TiO_2 anatase and rutile phases and praseodymium oxides are compared with Joint Committee on Powder Diffraction Standards (JCPDS) card file no 21-1272 (Anatase) and 21-1276 (Rutile).

3.3.2. Surface Area and Pore Size Distribution

Surface area, of the powder samples were obtained by Brunauer-Emmett-Teller (BET) N_2 sorption method. The pore size and pore size distribution of the samples were obtained by Barrett-Joyner-Halenda (BJH) method. These analyses were made at Gazi University Chemical Engineering Department using QuantoChrome–Autosorb–1C device.

3.3.3. X-Ray Photoelectron Spectroscopy (XPS)

X-ray photoelectron spectroscopy (XPS) analysis was used to determine surface composition, and electronic state of the elements in samples. The electronic states of Pr, Ti and O are determined by detailed spectra between 450 – 470 eV for $\text{Ti}2p$, 924 - 965 eV for $\text{Pr}3d$, 109 – 128 eV for $\text{Pr}4d$, and 525 - 540 eV for $\text{O}1s$. These analyses were made at METU Central Laboratory by using PHI 5000 VersaProbe device. During the tests neutralizer was used since the samples are semiconductors and surface charging leads deviations

such as shift of peaks to higher energies which make characterization harder, if neutralizer is not used. The obtained spectrums were corrected according to the carbon peak at 285 eV.

3.3.4. Photoluminescence

Photoluminescence tests are made by exciting the electrons in a semiconductor by a laser and detecting the photons emitted during electrons going back to its valance state. This analysis is made to see if photon up-conversion properties could successfully be achieved by praseodymium doping. These analyses are made at room temperature using HeCd laser at METU Physics Department.

3.3.5. Photoresponse Experiments

Photoresponse tests were performed to determine the conductivity of the samples in the presence of light. For this purpose, thin film samples were used. Two copper electrodes (about 30 gauges) are attached over the thin films 2mm apart by using conductive silver paste. A constant voltage of 5V DC was applied on the electrodes and the samples were exposed to monochromated beam between 300-800nm wavelength obtained by tungsten source and diffraction grating type monochromator. The photoresponse spectrum of the samples were obtained by measuring current passing from the thin films between 300-800 nm wavelength at 10nm intervals. The direct and indirect band gap energies of the samples were calculated by using photoresponse spectrum. These analyses are made at METU Physics Department.

3.3.6. TEM Analysis

High Resolution TEM imaging and EDX analysis were performed using JEOL JEM 2100F TEM microscope at METU Central Laboratory. Elemental mapping has been made in STEM mode using EDX to examine the dispersion of Pr in the structure. High resolution point analyses also have been made by using 2nm beam diameter. Moreover some High resolution TEM pictures have been taken to get deeper knowledge about the catalysts synthesized.

3.4. Photocatalytic Activity Tests

3.4.1. Methylene-Blue Degradation Test for Powder Samples

The photocatalytic activity of TiO_2 and Pr-TiO_2 samples were tested for methylene blue degradation as probe reaction. The effects of Pr doping and calcination temperature on the photocatalytic activity of the catalysts were studied. The reaction tests were performed at room temperature in batch type reactor. 250ml of 2 ppm methylene-blue solution in 250ml baker covered by quartz plate was mixed by magnetic stirrer and irradiated under artificial solar irradiation source with 300W/m^2 power between 280 – 780 nm wavelengths which is obtained by Suntest CPS+ solar simulator. The reaction was initiated by adding 0.1 g of catalyst sample. Solutions were continuously stirred during the tests using a magnetic stirrer. Samples are taken from the solution every half an hour and their UV-Visible absorbance spectra were obtained between 200-800nm by using Shimadzu 2550 UV-Visible spectrophotometer.

3.4.2. Methylene-Blue Degradation Test for Thin Film Samples

The photocatalytic activities of TiO₂ and Pr-TiO₂ thin films on glass samples were determined by methylene blue degradation reaction as probe reaction. At the start of the tests, UV-Visible spectra of the chosen and marked spot on the thin films were obtained by using Shimadzu 2550 UV-Visible spectrophotometer. The thin film samples were immersed in 100ppm methylene blue solution for 24 hours in dark and the UV-Visible spectrum of the same spot were determined again. The difference of the spectra was used for the determination of initial concentration of methylene blue arbitrarily. The degradation reaction was performed by exposing the samples to the artificial solar irradiation with 300 W/m² power measured between 280 - 780 nm by using SUNTEST CPS+ solar simulator. The UV-Vis spectrum of the same spot was measured at 15, 30, 60, 90, 120, 180, 240 min irradiation time. The reaction time course was followed with respect to the methylene blue concentration at the marked spot versus time.

3.4.3. Phenol Mineralization Test for Powder Samples

Phenol mineralization tests were also employed in order to determine photocatalytic activity of the powder samples. The batch reaction experiments were carried out by using 250 ml of 20 ppm phenol solutions in the presence of 0.1 g catalyst sample. Tests were performed under simulated sunlight with 300W/m² power measured between 280 – 780nm wavelength. Solutions were continuously stirred during the tests using a magnetic stirrer and air is bubbled from bottom of the solution with 1 L/min flowrate to ensure the presence of dissolved oxygen. Liquid samples are withdrawn at reaction time of 0th, 30th, 60th, 90th, 120th, 180th, 240th and 300th minutes. Samples were analyzed using Shimadzu UV-2550 UV-Visible spectrophotometer between 200-400nm. During phenol mineralization, the concentration of reaction intermediates such as benzoquinone, hydroquinone, catechol,

muconic acid, maleic acid, fumaric acid, oxalic acid were followed by UV-Vis spectroscopy with the attributed wavelengths given in Table 3 [67]. These components were selected by considering the results of previous work. The proposed mineralization pathway for phenol is given in Figure 11 by B.Bayram [67].

Table 3: Main absorption wavelengths of the species during the reaction

| Compound | Wavelength |
|-----------------|-------------------|
| Benzoquinone | 246 |
| Hydroquinone | 289 |
| Catechol | 271.5 |
| Muconic acid | 264 |
| Maleic acid | 211 |
| Fumaric acid | 207 |
| Oxalic acid | 222.5 |
| Phenol | 270 |

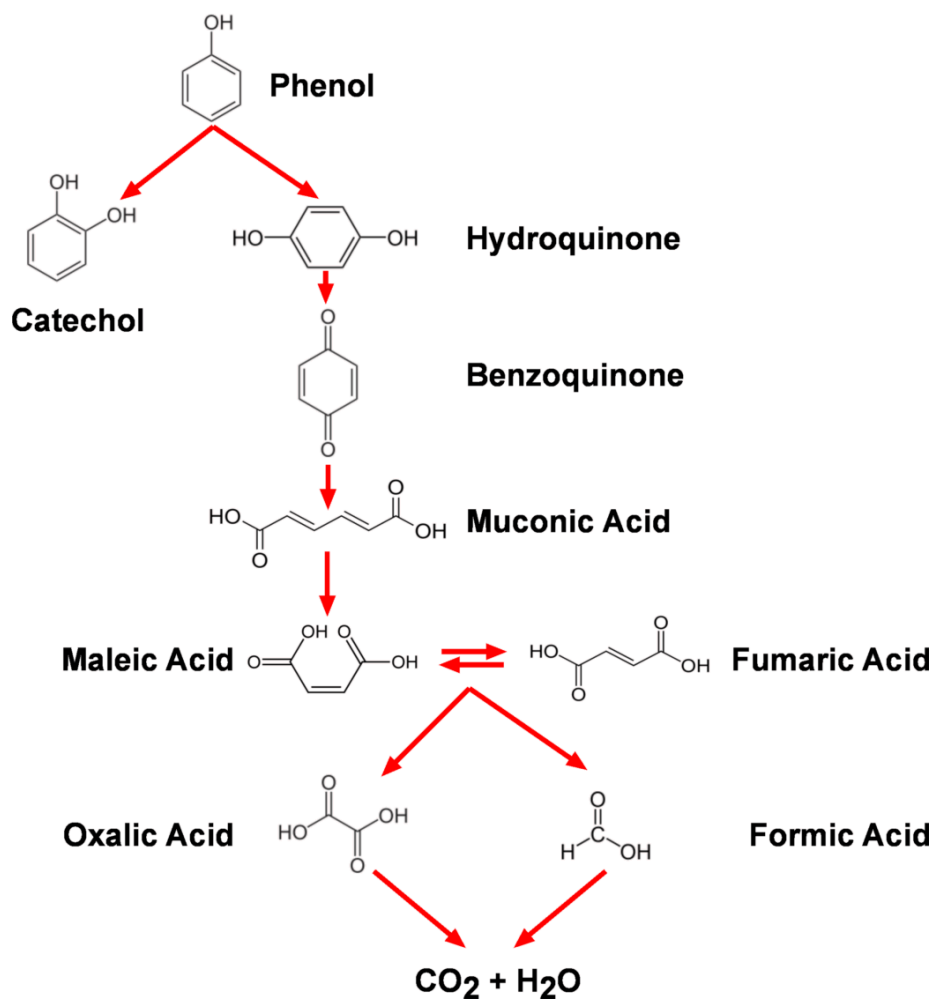


Figure 11: Reaction mechanism for the complete demineralization of phenol [67].

CHAPTER 4

RESULTS AND DISCUSSION

In this study, the effect of praseodymium doping on titania crystal structure and the photocatalytic activity have been investigated. The pure TiO_2 , and 1%Pr, 5%Pr and 20%Pr containing TiO_2 samples were successfully synthesized by the sol-gel method which has been described in experimental section. The effect of calcination temperature on the crystal structure, textural properties and photocatalytic activity was examined by calcination of samples at 400°C, 500°C and 600°C for 240 minutes in air flow.

4.1. Characterization

The catalyst characterization was performed by using XRD, XPS, BET, and TEM. XRD is used to characterize the crystal structures and phases present in the catalyst. For surface characterization of the catalysts prepared XPS analysis is used. Surface area and the pore structure of the samples have been examined by the use of BET and BJH analysis. On TEM the structure of the samples have been examined, by the use of high resolution TEM information about the size of the powder catalysts and the crystal planes in the structure showing the crystal structure have been gathered, and also EDAX analysis made by TEM showed the distribution of the elements in the structure. In this section detailed information on the characterizations made are given.

4.1.1. X-Ray Diffraction

XRD analyses were performed on prepared catalyst samples to examine the effect of praseodymium on crystal structure, oxide phases, bulk composition and crystallite size. The XRD spectra of pure TiO_2 and 1%Pr- TiO_2 samples calcined at 300°C and 400°C in air for 240 minutes (T300, T400, P300 and P400 respectively) are consistent with 100% anatase as shown in Figure 12. The peaks 25.5, 48.2, 54.1, 55.3, 68.9, 70.5, 75.2, 76.1 2θ show the presence of (1 0 1), (2 0 0), (1 0 5), (2 1 1), (1 1 6), (2 2 0), (2 1 5), (3 0 1) planes of the anatase structure. However pure TiO_2 calcined at 500°C, reveals the traces of rutile phase which is revealed by the peak at 27.6 2θ indicating (1 1 0) plane. In the spectrum of 1%Pr- TiO_2 , there are no peaks which can be associated with Pr, or its oxides such as PrO_2 , Pr_2O_3 etc. which can be explained as 1%Pr is below the detection limits or the lack of ordered crystalline structure. The amount of rutile in the T500 sample is not significant when the signal/noise ratio of the spectrum and sensitivity is considered. When the calcination temperature is increased to 600°C, 1%Pr- TiO_2 sample (P600) possesses 100% pure anatase structure although the pure TiO_2 sample (T600) has polycrystalline structure having significant amount of rutile. The XRD spectrum of pure TiO_2 is analyzed by attributing 25.5 2θ and 27.6 2θ for (1 0 1) and (1 1 0) planes of anatase and rutile respectively. The analysis revealed that the polycrystalline structure consists of 82% anatase and 18% rutile. This indicates that praseodymium suppresses the rutile formation and stabilizes the anatase phase. To validate phase stabilization, another sample set was calcined at 650°C (T650 and P650) The X-ray spectra of these two samples prove that doping titania with praseodymium suppresses the rutile formation. Pure TiO_2 sample calcined at 650°C (T650) is composed of 78% anatase and 22%rutile while 1%Pr- TiO_2 (P650) sample is composed of almost 100% anatase having traces of rutile formation. It can be clearly stated that the transformation of anatase to rutile phase is promoted by temperature as expected but the presence of 1%Pr suppresses the rutile formation.

Table 4: XRD peaks of anatase and rutile with copper source

| 2 θ | Intensity (%) | d-Spacing | Plane | 2 θ | Intensity (%) | d-Spacing | Plane |
|------------|---------------|-----------|---------|------------|---------------|-----------|---------|
| 25.33 | 100.00 | 35.163 | (1 0 1) | 27.50 | 100.00 | 32.435 | (1 1 0) |
| 36.98 | 6.29 | 24.307 | (1 0 3) | 36.17 | 46.72 | 24.836 | (1 0 1) |
| 37.82 | 20.24 | 23.786 | (0 0 4) | 39.28 | 7.11 | 22.935 | (2 0 0) |
| 38.60 | 7.13 | 23.322 | (1 1 2) | 41.34 | 18.28 | 21.840 | (1 1 1) |
| 48.09 | 28.07 | 18.921 | (2 0 0) | 44.15 | 6.45 | 20.514 | (2 1 0) |
| 53.93 | 17.92 | 17.001 | (1 0 5) | 54.46 | 57.99 | 16.849 | (2 1 1) |
| 55.12 | 17.56 | 16.662 | (2 1 1) | 56.77 | 17.32 | 16.217 | (2 2 0) |
| 62.17 | 2.96 | 14.931 | (2 1 3) | 62.93 | 8.18 | 14.770 | (0 0 2) |
| 62.75 | 13.68 | 14.808 | (2 0 4) | 64.21 | 8.66 | 14.505 | (3 1 0) |
| 68.82 | 6.03 | 13.642 | (1 1 6) | 69.18 | 20.83 | 13.579 | (3 0 1) |
| 70.37 | 6.65 | 13.379 | (2 2 0) | 69.99 | 10.44 | 13.442 | (1 1 2) |
| 75.12 | 10.24 | 12.646 | (2 1 5) | | | | |
| 76.12 | 2.75 | 12.505 | (3 0 1) | | | | |
| 82.77 | 5.18 | 11.661 | (2 2 4) | | | | |

These results show us that doping titania with praseodymium decreases the amount of rutile formation in the sample during calcination. It is shown that praseodymium doping suppresses the rutile formation in titanium dioxide. Since the photocatalytically active phase of titania is anatase and rutile is not active photocatalytically, doping titania with praseodymium would increase the photocatalytic activity by leading to formation of more anatase in the crystal structure.

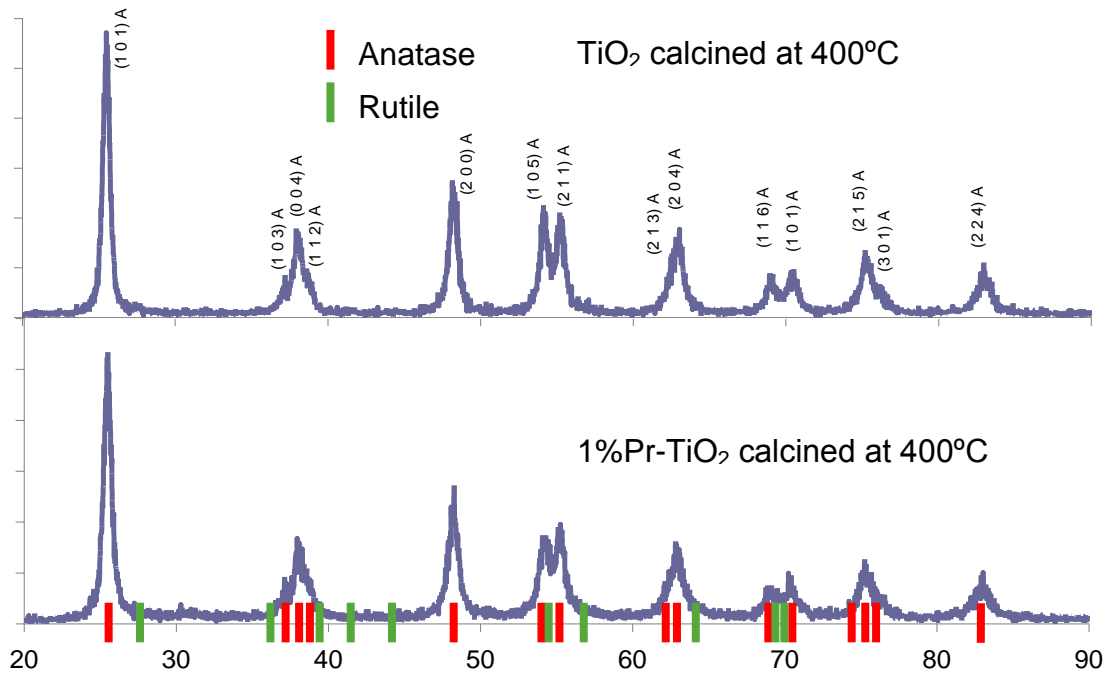


Figure 12: X-ray spectra for T400 and P400 samples

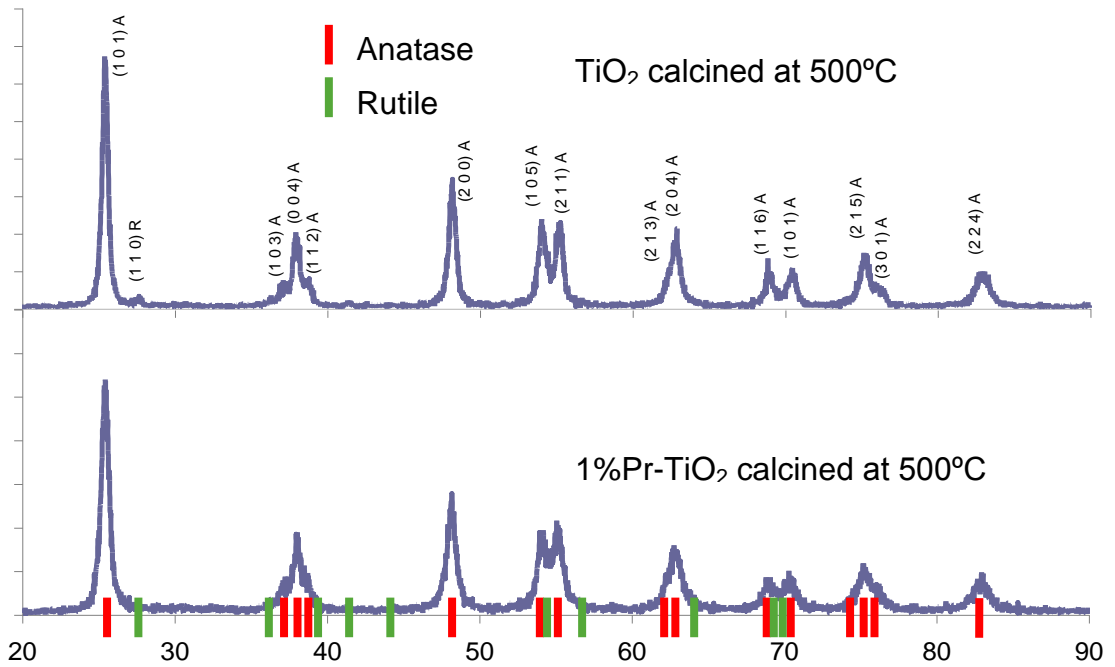


Figure 13: X-ray spectra for T500 and P500 samples

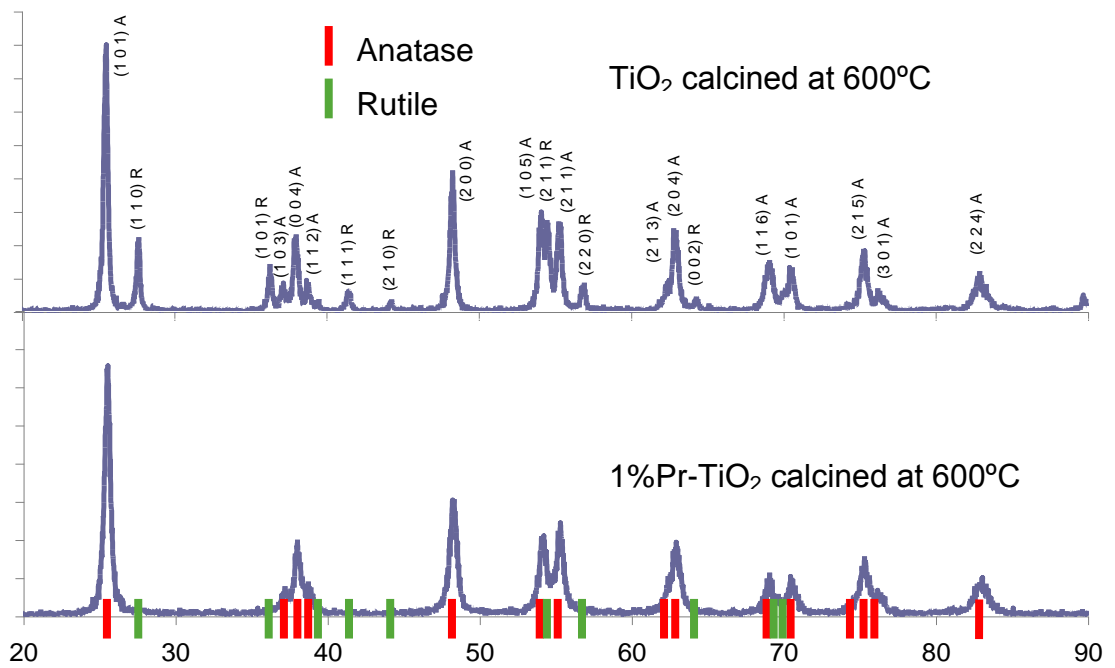


Figure 14: X-ray spectra for T600 and P600 samples

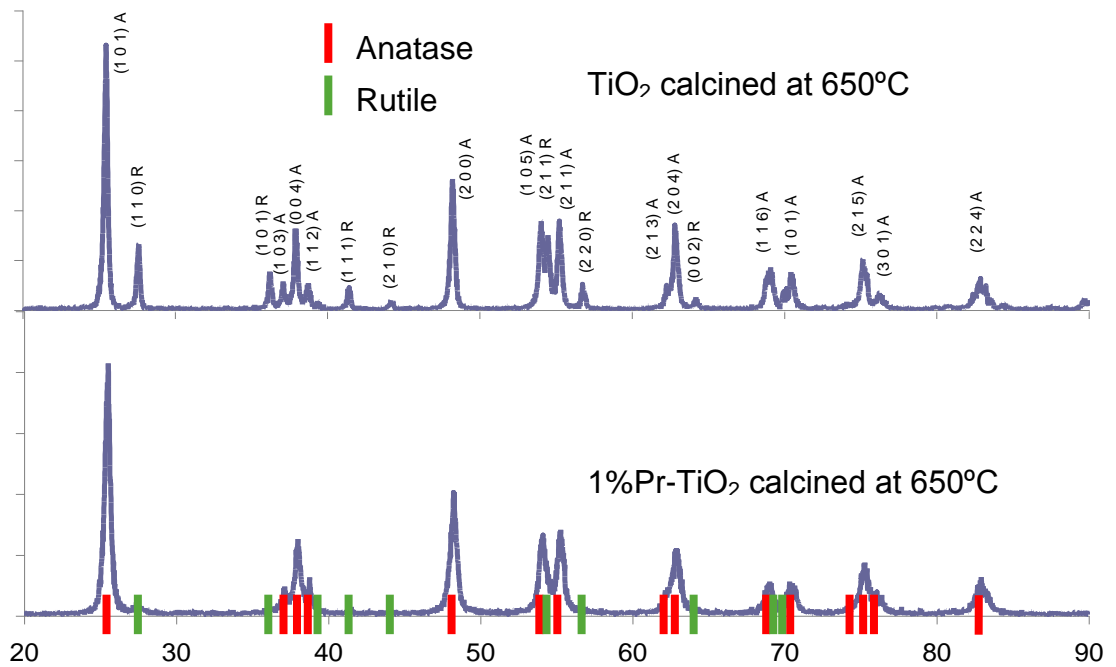


Figure 15: X-ray spectra for T650 and P650 samples

Table 5: The effect of calcination temperature on crystal structure; the XRD analysis of TiO₂ and 1%Pr-TiO₂ samples.

| Sample | Anatase | Rutile | Sample | Anatase | Rutile |
|--------|---------|--------|--------|---------|--------|
| T300 | 100 % | 0 % | P300 | 100 % | 0 % |
| T400 | 100 % | 0 % | P400 | 100 % | 0 % |
| T500 | 100 % | Trace | P500 | 100 % | 0 % |
| T600 | 82 % | 18 % | P600 | 100 % | 0 % |
| T650 | 78 % | 22 % | P650 | 100 % | Trace |

By using diffraction data, crystalline size of the anatase and rutile phases have been calculated using Scherrer equation [217]:

$$D = \frac{0.9\lambda}{B_{1/2} \cos \theta} \quad (21)$$

Where D is the crystal size, λ is the wavelength of the X-ray that is 1.5405 Å for copper X-ray source. $B_{1/2}$ is the full-width at half maximum and θ is the Bragg angle. The derivation of Scherrer equation assumes that only infinite crystals are perfect, and as the size decreases broadening of the XRD peaks increases. Also it is assumed that incident X-rays are parallel to each other, but nonparallel rays also exists in any real XRD experiment which also effects the broadening and also creates some background. Another assumption is that the X-ray beam used is monochromatic that is not possible to obtain in a real beam. The usual “monochromatic” contains strong $K\alpha$ component superimposed on the continuous spectrum, but the $K\alpha$ itself

has a width of about 0.001 Å and this divergence from monochromatic beam is another cause for line broadening since each value of λ corresponds to a value of θ [217]. Moreover there is always an instrument background caused by the detector, sample holder and the chamber itself. While finding the half width of the peak this background is subtracted from the peak obtained.

The full width at half maximum (FWHM) of the peaks at 2θ angles of 25.5° and 27.6° for (1 0 1) anatase and (1 1 0) rutile planes are utilized for the analysis. Calculated crystalline sizes for the both catalyst phases are tabulated in Table 6.

Table 6: Crystallite sizes for the TiO_2 and 1%Pr- TiO_2 samples; The effect of calcination temperature.

| | crystal size for Anatase (nm) | crystal size for Rutile (nm) |
|------|-------------------------------|------------------------------|
| T300 | 14.3 | - |
| T400 | 16.0 | - |
| T500 | 18.5 | - |
| T600 | 25.5 | 34.1 |
| T650 | 31.3 | 34.1 |
| P300 | 10.7 | - |
| P400 | 13.8 | - |
| P500 | 14.3 | - |
| P600 | 19.0 | - |
| P650 | 19.9 | - |

As it is seen from the table, crystalline sizes of Pr doped TiO₂ samples are consistently smaller than for pure TiO₂ samples. These results also confirm the inhibition of crystal growth by praseodymium. As anatase crystals grow they transform their crystal orientation to rutile form. In our experiments, anatase crystallites have grown by calcination and lose the stability over 20nm size. Samples except T600 and T650 have crystallite sizes of smaller than 20nm and are pure anatase. T600 catalyst has a crystal size of 25.5nm and T650 catalyst has a crystal size of 31.3nm for anatase crystallites and both samples have polycrystalline structure. Also increase in the crystal size for anatase leads to higher rutile composition in the catalyst. The crystallite size of rutile phase for both T600 and T650 samples yield similar results (34.1nm) which is larger than the anatase phase crystallite size.

Rutile is the more stable phase of titanium dioxide in bulk form. Anatase is more stable in small crystal sizes. Doping titanium dioxide with praseodymium inhibits crystal growth and sintering of anatase crystals leading smaller crystal sizes and phase stabilization of anatase.

Phase stabilization effect of praseodymium doping can be explained by crystallite size growth inhibition effect of Pr doping. This effect was proposed to be due to segregation of the praseodymium cations at the grain boundaries, which inhibited the grain growth by restricting direct contact of grains [162]. However, it was observed in the TEM analysis in our study that Pr atoms homogeneously distribute in the structure instead of occupying the grain boundaries, this is going to be explained in detail in Section 4.1.6. Wu et. al. [218] suggested the reasons of doped elements impacting on the grain growth may be the follows: (1) The growth process can be seen as order and energy transmission process through the interface. Some Pr ions can be efficient into the lattice of TiO₂, may form Pr₆O₁₁ layer and it can inhibit the order and energy transmission of TiO₂ crystallite, and restrain the growth. (2) It may attribute to the Pr effect on the sol-gel transformation during the

preparation process or the transformation from amorphous to crystalline structure. Specific explanation still needs to be further investigation.

From the XRD data obtained, interplanar spacing (d) between the corresponding planes for some peaks have been calculated by Bragg's Law;

$$n\lambda = 2d \sin \theta \quad (22)$$

Where n is the order of reflection, which is an integer and usually taken as 1. Interplanar spacing (d) for peaks corresponding to (1 0 1), (2 0 0), (1 0 5), (2 1 1), (1 1 6), (2 2 0), (2 1 5), (3 0 1) planes of the anatase and (1 1 0), (1 0 1), (2 0 0), (1 1 1), (2 1 0), (2 1 1), (2 2 0), (0 0 2), (3 1 0) planes of the rutile structure have been calculated and tabulated in

Table 7, Table 8 and they are in good agreement with the literature [1, 9, 42, 43, 54, 219].

4.1.2. Surface Area and Pore Size Distribution

The textural properties of catalyst samples are analyzed by N₂-BET analysis. Surface area and pore size distribution information gathered by BET and BJH methods are tabulated in Table 9 and Table 10. When the BET surface area of Pr doped and pure TiO₂ samples which are calcined at different temperatures are compared, it is observed that doping with praseodymium enhances both the surface area and the total pore volume significantly. Amlouk et. al. [161] also reported similar observation for Pr doping. From the results, it is also seen that increasing the calcination temperature decreases the surface area because of crystal growth, ripening and sintering of the samples but praseodymium doped samples show a lower decrease in the surface area and total pore volume by the increase in the calcination temperature. These results also confirm our observations for crystallite size analysis of XRD results. Also pore volume for pores smaller than 2.64nm decreases with calcination temperature. This is because of the crystal growth; these pores are in the amorphous phase, as the calcination temperature increases amorphous to crystal transition increases and the amount of these pores decreases since the crystallinity increases with calcination temperature. Another effect of Pr doping was also observed in the pore size distributions obtained by the analysis of desorption isotherms by BJH method. The pure TiO₂ samples have a sharp single peak showing a narrow pore size distribution varying between 3-6 nm while Pr doped TiO₂ samples have bi-modal pore size distribution. Such pore size can be attributed to the mesopores between the crystalline particles.

TiO₂ calcined at 400°C has an adsorption-desorption isotherm of Type IV according to IUPAC classification indicating mesoporous structure. Large hysteresis loop was observed. Desorption branch of hysteresis loop is quite sharp. However adsorption branch is not sharp and hysteresis loop closes at a high relative pressure of nitrogen (at about 0.85). This hysteresis loop is denoted as H2 by IUPAC classification and it indicates complex pore

structures with interconnected Networks of pores of different sizes. In fact the pore size distribution from adsorption branch of BJH isotherm indicated the presence of pores having diameters between 1.5-20 nm. Sharp pore size distribution obtained from the desorption branch indicated the presence of pore windows of about 3.7 nm in diameter.

Table 9: Surface area results of the samples

| SAMPLE | Surface Area m²/g (Single point BET) | Surface Area m²/g (BJH(ads)) | Surface Area m²/g (BJH(des)) |
|---------------|--|--|--|
| T400 | 38.0 | 46.4 | 61.1 |
| P400 | 59.2 | 73.4 | 82.5 |
| T500 | 23.5 | 28.1 | 46.3 |
| P500 | 53.8 | 65.4 | 80.9 |
| T600 | 2.6 | 3.2 | 8.3 |
| P600 | 30.5 | 36.0 | 57.8 |
| T650 | 2.4 | 4.3 | 12.3 |
| P650 | 15.6 | 23.5 | 40.5 |

Table 10: Pore volume and diameter results of the samples

| SAMPLE | Pore Volume (cm³/g) (for pores smaller than 2.64 nm) | Pore Volume (cm³/g) (for pores smaller than 500 nm) BJH(des) | Average Pore diameter (nm) (BJH(ads)) | Average Pore diameter (nm) (BJH(des)) |
|---------------|---|---|--|--|
| T400 | 0.020 | 0.065 | 5.4 | 3.7 |
| P400 | 0.030 | 0.077 | 4.2 | 3.5 |
| T500 | 0.012 | 0.050 | 6.2 | 3.7 |
| P500 | 0.027 | 0.084 | 5.0 | 3.7 |
| T600 | 0.001 | 0.010 | 2.9 | 3.9 |
| P600 | 0.015 | 0.069 | 8.9 | 3.7 |
| T650 | 0.001 | 0.020 | 3.6 | 4.1 |
| P650 | 0.008 | 0.049 | 10.0 | 3.7 |

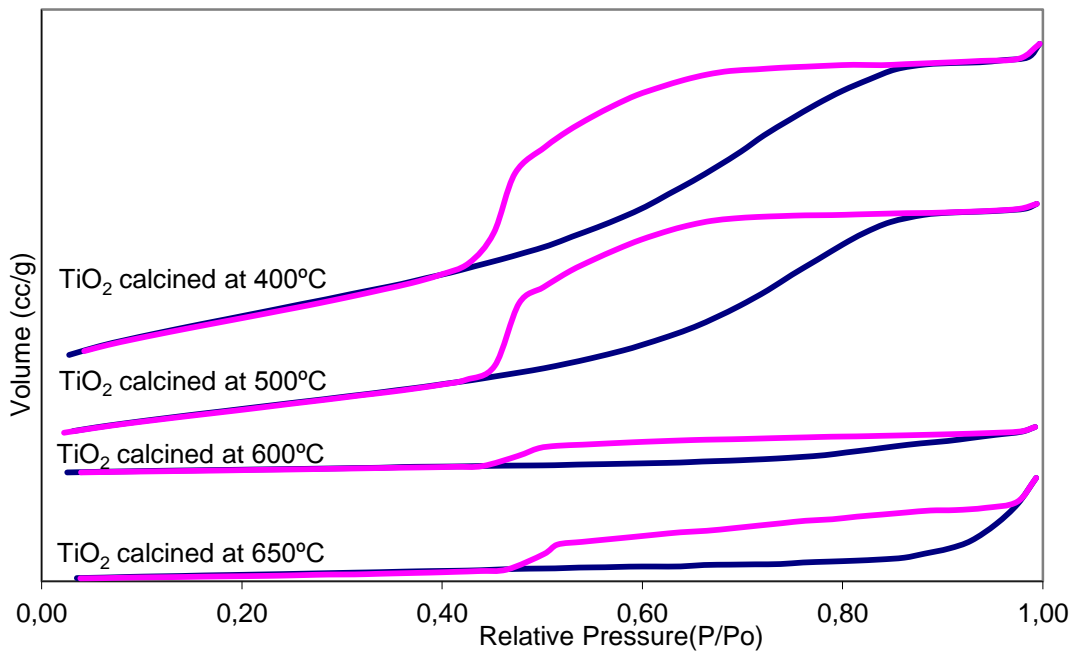


Figure 16: BET isotherm of TiO_2 calcined at 400, 500, 600, 650°C

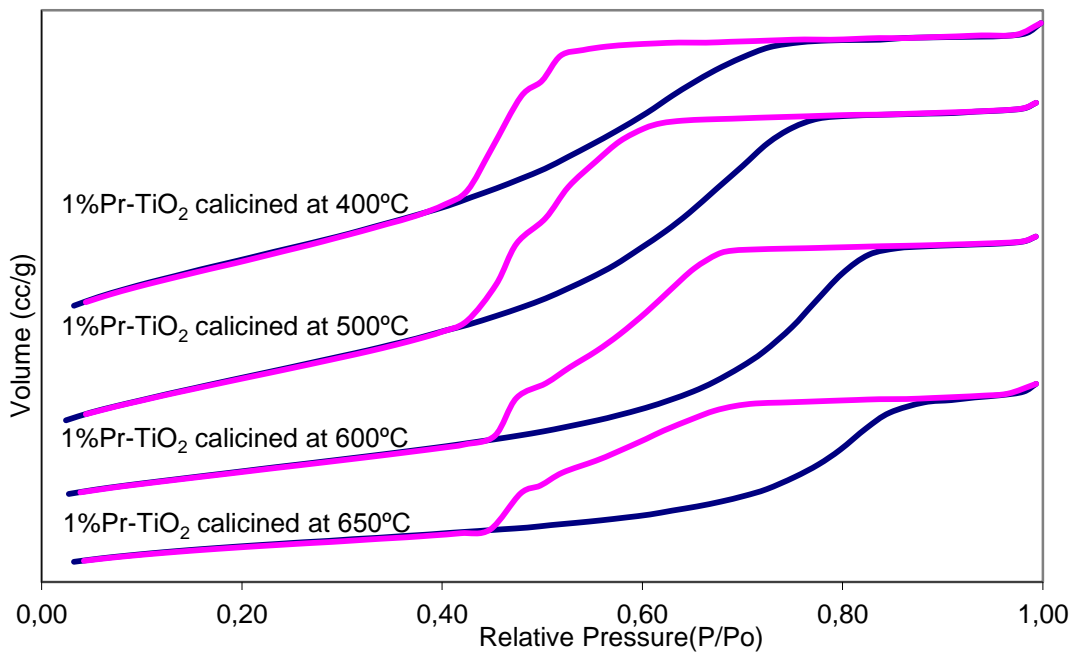


Figure 17: BET isotherm of TiO_2 doped with 1%Pr calcined at 400, 500, 600, 650°C

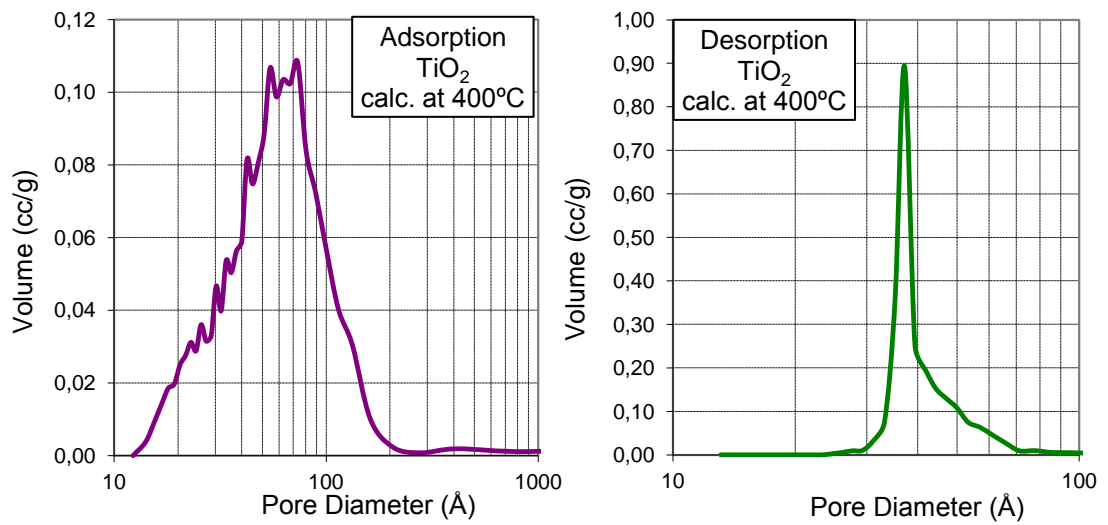


Figure 18: BJH adsorption and desorption pore size distribution of TiO₂ calcined at 400°C

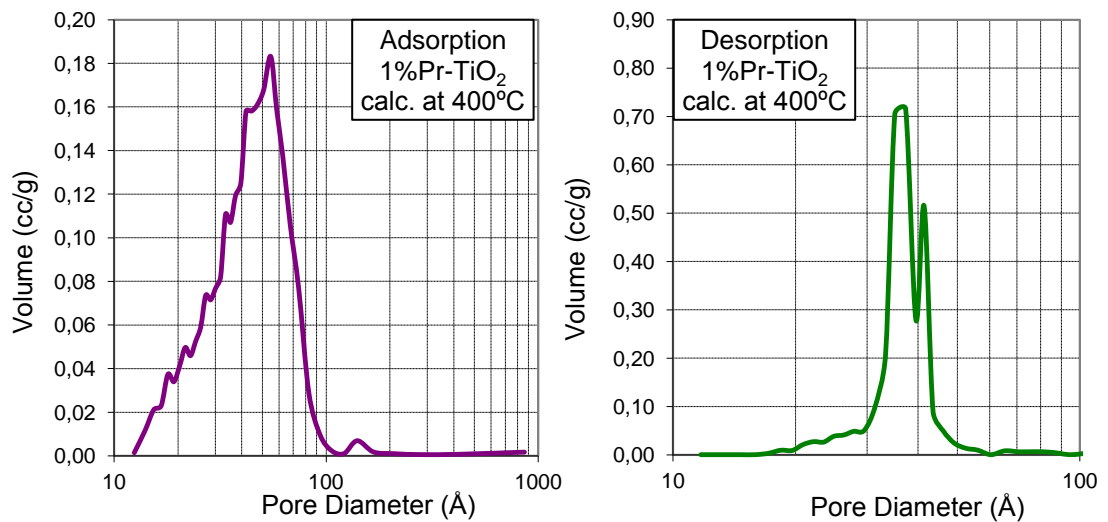


Figure 19: BJH adsorption and desorption pore size distribution of TiO₂ - Pr calcined at 400°C

TiO₂ doped with Pr and calcined at 400°C has quite similar adsorption-desorption isotherms with undoped counterpart. However, the closure of adsorption and desorption branches of the hysteresis loop is at a lower relative pressure (at about 0.75). As a result, the pore size distribution from the adsorption branch is narrower (in a range of 1.5-10 nm). Also this material has a higher surface area and pore volume. Moreover, from the desorption branch besides the pores of 3.7 nm some amount of pores with 4.2 nm size can be observed.

The adsorption desorption isotherms of samples calcined at 500°C are very similar to the samples which are calcined at 400°C. The samples calcined at 500°C demonstrate complex pore structure with interconnected networks of pores between 1.5-25 nm according to the BJH adsorption branch and a narrow distribution around 3.7 nm according to the desorption branch. However, the BET surface area of the samples reduced significantly with the increase of calcination temperature which can be explained by sintering.

1%Pr-TiO₂ samples calcined at 400°C and 500°C demonstrate similar adsorption desorption isotherms. The hysteresis loop closes at around 0.78 and the pore size distribution according to the adsorption branch pore sizes vary between 1.5 – 12 nm. The sintering cause a decrease in the surface area from 73 to 65m²/g but this decrease is not drastic as in the TiO₂ samples. When 1%Pr-TiO₂ samples calcined at 400°C and 500°C are compared, the PSD based on desorption isotherm of the sample calcined at 500°C has bimodal pore size distribution around 3.7 nm and 4.2 nm. The increase in calcination temperature causes pore size distribution widening towards higher pore size.

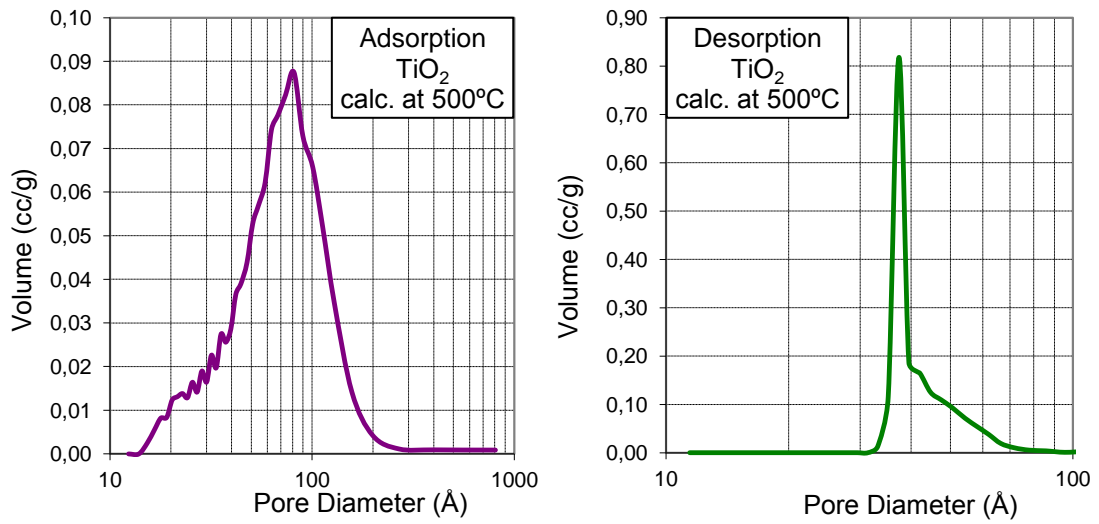


Figure 20: BJH adsorption and desorption pore size distribution of TiO₂ calcined at 500°C

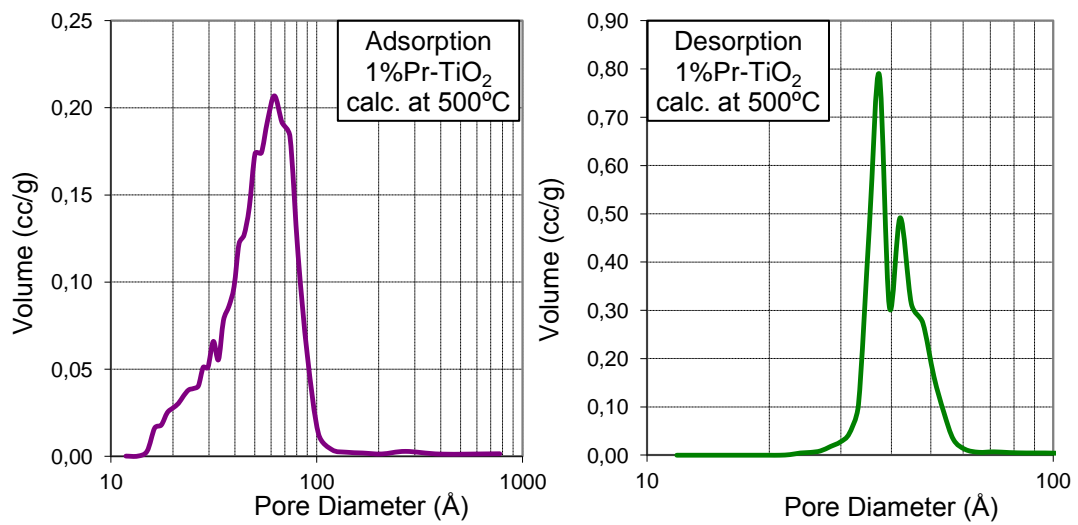


Figure 21: BJH adsorption and desorption pore size distribution of TiO₂ - Pr calcined at 500°C

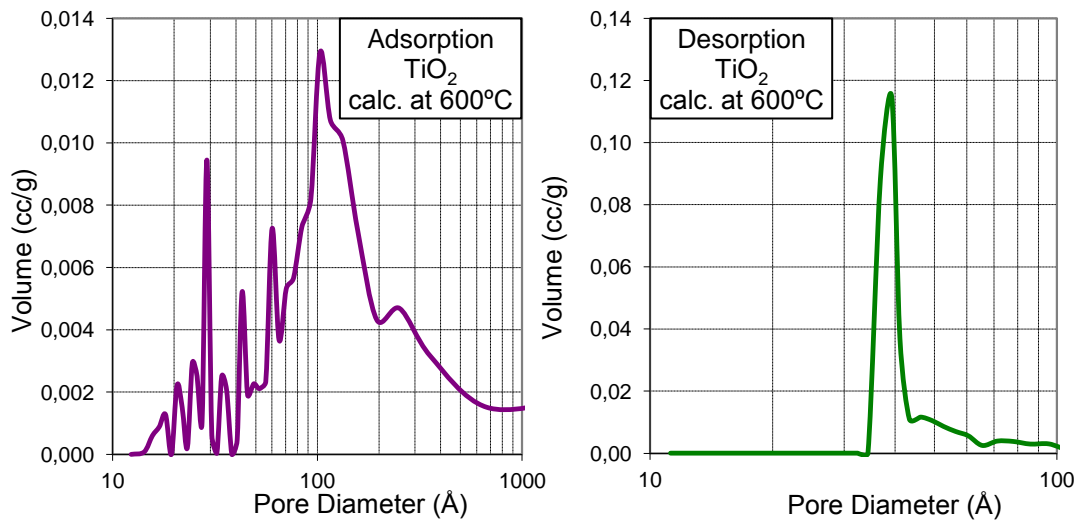


Figure 22: BJH adsorption and desorption pore size distribution of TiO₂ calcined at 600°C

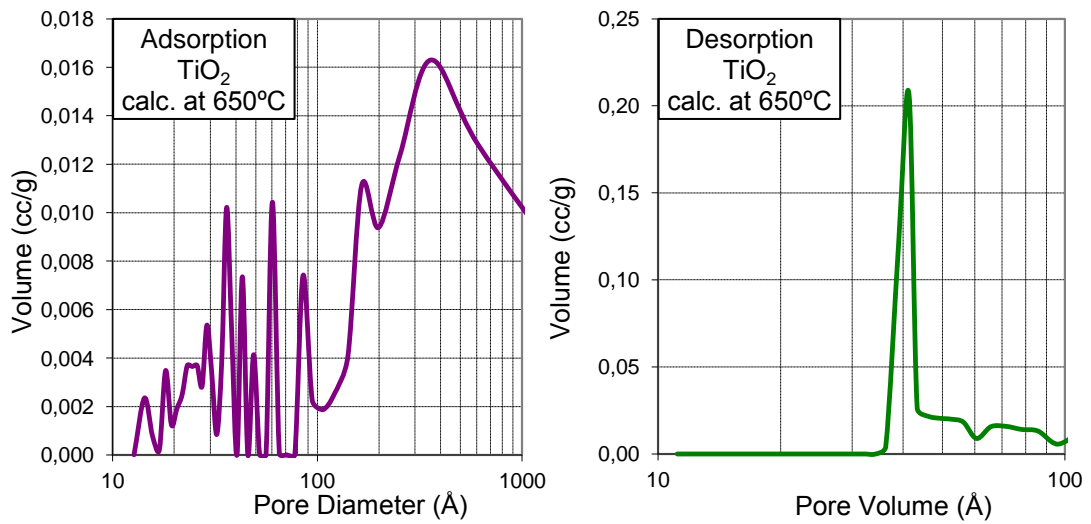


Figure 23: BJH adsorption and desorption pore size distribution of TiO₂ calcined at 650°C

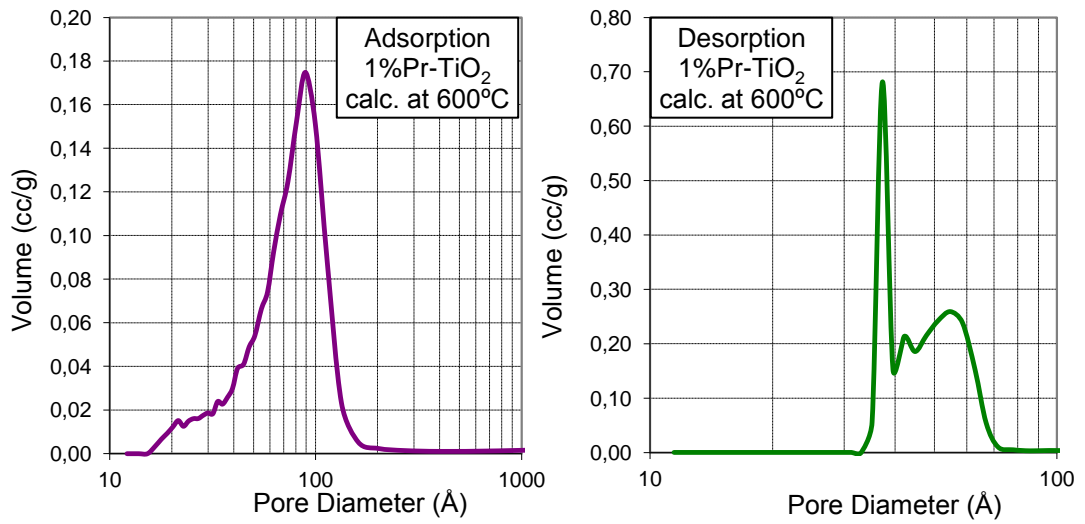


Figure 24: BJH adsorption and desorption pore size distribution of TiO₂ - Pr calcined at 600°C

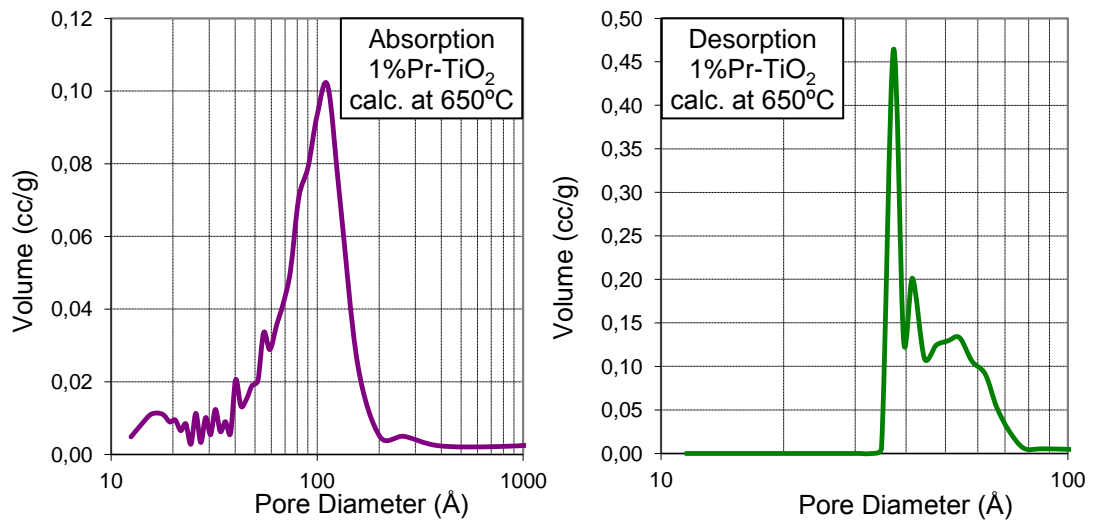


Figure 25: BJH adsorption and desorption pore size distribution of TiO₂ - Pr calcined at 650°C

For TiO_2 calcined at 600 and 650°C although the adsorption-desorption isotherm still indicate a mesoporous material, the pore size distribution based on adsorption isotherm indicate the macroporous structure which can be explained by inter-particle voids. Adsorption peak for T650 seems more like a macroporous material than T600. Closure of adsorption-desorption branches of the hysteresis loop takes place at a very high nitrogen relative pressure (of about 0.96). These materials have very low surface area and very low pore volume. Also when adsorption pores size distribution of TiO_2 calcined at 600 and 650°C are examined, it is observed that the adsorption pore size distribution graph characteristics change drastically. This is because of the formation of rutile in the structure. A more complex and wider adsorption pore size distribution can be observed because rutile particles are larger than anatase particles and the pores that are the voids between the particles changes according to the particle sizes.

Major improvement was achieved in the textural properties by Pr doping at 600°C. Both surface area and pore volume values are much higher than the corresponding values of T600. These samples demonstrate Type IV isotherm with a H2 hysteresis loop, indicating the presence of mesoporous structure with high interconnectivity between the pores. One very important result of N_2 adsorption analysis is related with the differences of average pore diameters obtained from the adsorption and desorption isotherms. The average pore diameter was estimated as 8.9 nm by using adsorption isotherm which is quite higher than 3.7nm which is estimated from desorption isotherm. The adsorption branch indicated the presence of pores with large distribution of pores having diameter between 1.5-20 nm, and desorption branch indicates very narrow distribution of pore size. Also wider pore size distribution is observed in desorption branch with respect to P500 catalyst by the increase in the crystal size.

The adsorption-desorption isotherm of P650 is similar to P600. Although the surface area has decreased to its half with increasing the calcination

temperature by 50°C, it still has much higher surface area than the pure TiO₂ sample. The average pore diameter values obtained as 10 nm and 3.7 nm from adsorption and desorption isotherms, respectively. The widening in the pore size distribution according to desorption isotherm was also observed with the increase of calcination temperature. These values and the shape of the adsorption-desorption isotherms indicate the presence of some cages of larger diameters in the range of 5-20 nm (with an average diameter of 10 nm), which are connected by narrower windows of about 3.7 nm in diameter. However it has mesoporous structure with sufficiently high surface area and good pore structure allowing easy penetration of the reacting molecules.

For all isotherms no micropores can be observed. This is because the pore structure is mostly because of the voids between the particles. This can also be seen in TEM images (Section 4.1.6). In TEM images solid particles around 15nm diameter are observed and no porosity can be seen on them. Porosity also decreases with the increasing temperature because of growth of the particles.

4.1.3. X-ray Photoelectron Spectroscopy (XPS)

In order to analyze the Ti, Pr and O species on the samples, the structure and incorporation of Pr species into the TiO₂ particles, the samples are also analyzed by XPS. The XPS spectrum of 1% Pr-TiO₂ and pure TiO₂ samples calcined at 600°C were analyzed in detail. The survey scan and Ti2p, O1s, and Pr3d spectra which are corrected according to the carbon peak at binding energy of 285 eV are shown in Figure 26 -Figure 29. As it is seen from the Pr3d spectra, Pr²⁺ has not been detected on the surface of 1%Pr-TiO₂ sample. The sensitivity of XPS depends on many parameters and any element heavier than lithium can be detected in ppm concentration range if the top 1-5nm of the surface has such concentration and sufficient collection time applied. The semiconductor samples such as TiO₂ tend to charging and

decompose under long exposures. The Pr3d spectra indicate that the concentration of Pr over the sample surface is very low and below the detection limits. These results can be interpreted as Pr is well dispersed and incorporated in TiO₂ matrix and the concentration of Pr in outer surface of TiO₂ particles is under the detection limits of the method.

Table 11: XPS detailed scan energy intervals

| | Ti2p | O1s | Pr3d | Pr4d |
|----------------------|---------|---------|---------|---------|
| Energy Interval (eV) | 452-468 | 525-237 | 925-962 | 109-127 |

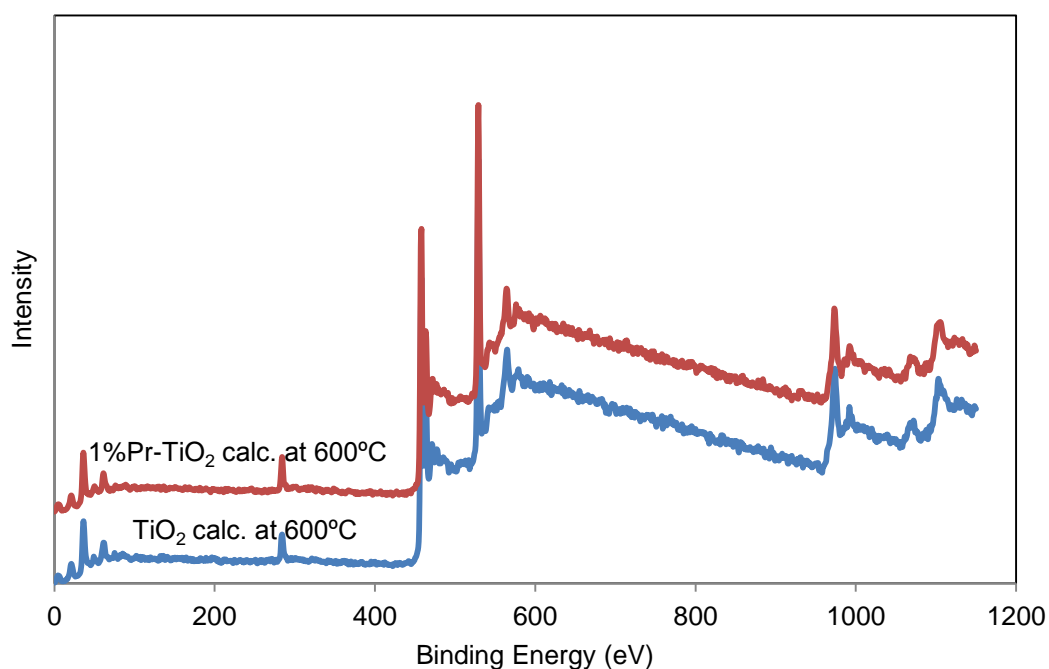


Figure 26: XPS survey scan of Pure TiO₂ and TiO₂-1%Pr calcined at 600°C

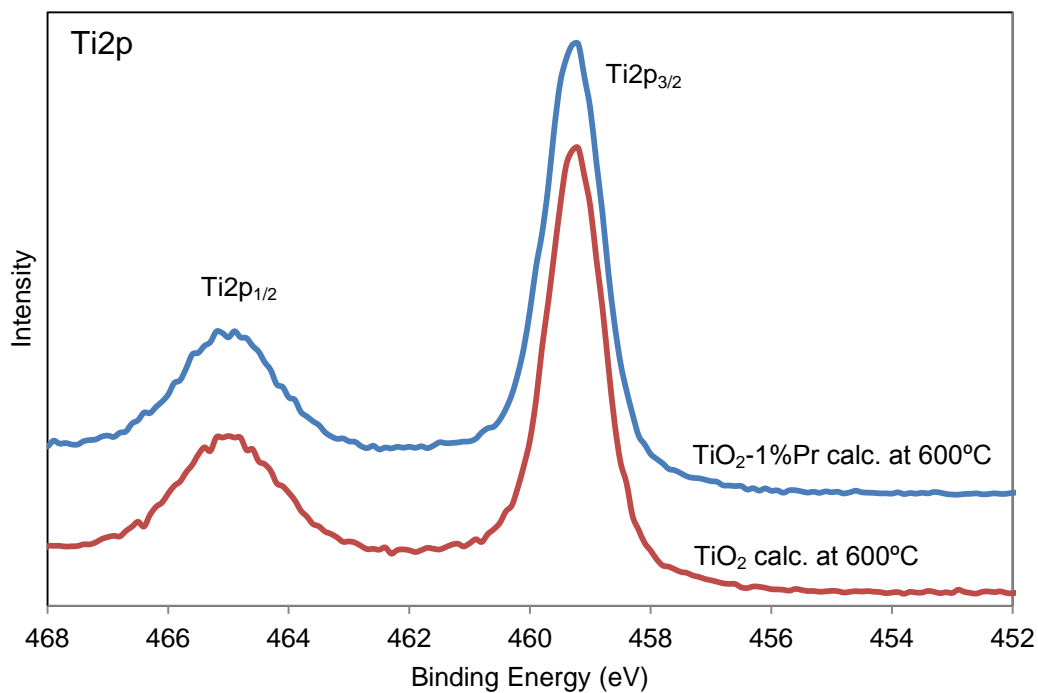


Figure 27: XPS Ti2p spectrum of Pure TiO_2 and TiO_2 -1%Pr calcined at 600°C

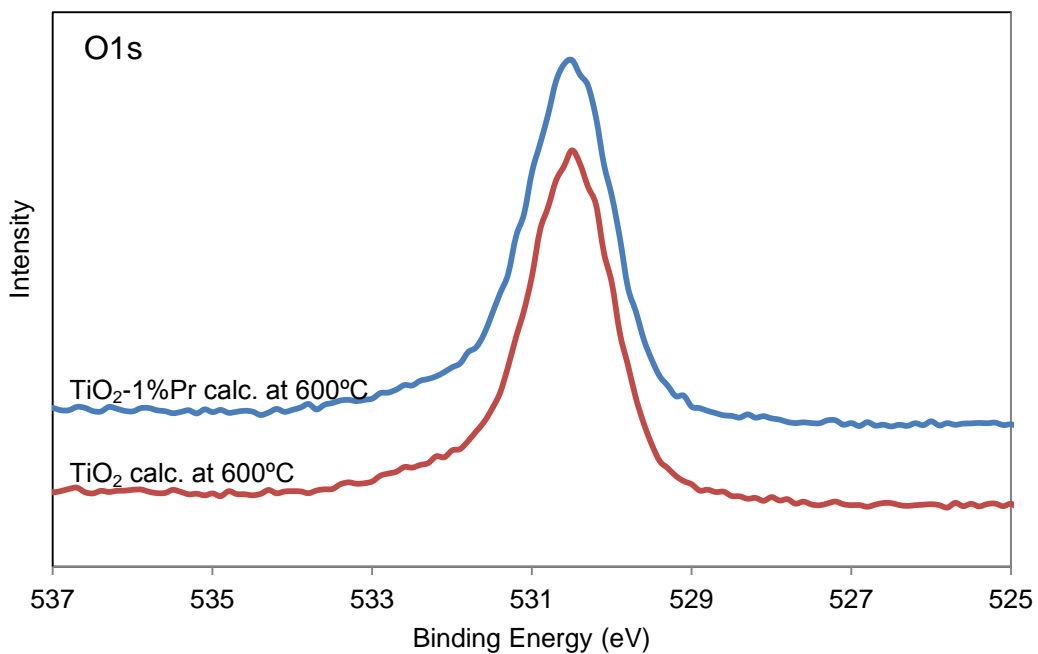


Figure 28: XPS O1s spectrum of Pure TiO_2 and TiO_2 -1%Pr calcined at 600°C

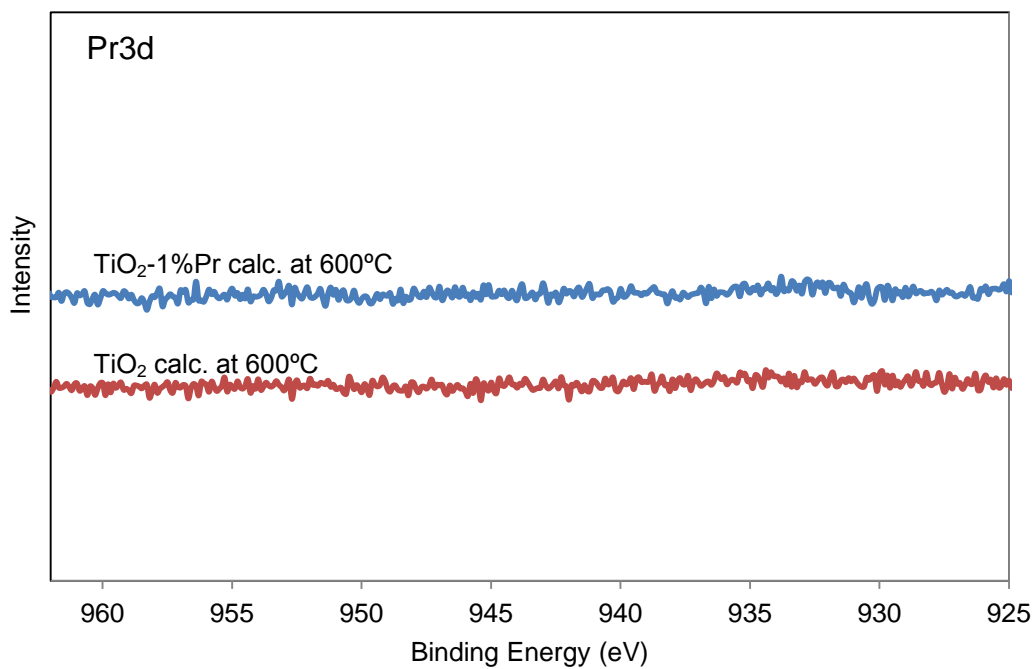


Figure 29: XPS Pr3d spectrum of Pure TiO₂ and TiO₂-1%Pr calcined at 600°C

In order to ensure these observations, 5% and 20% Pr containing samples are prepared and calcined at 500 and 600°C. Similarly no Pr was observed in Pr3d spectrum of the catalysts containing 5% Pr. However, 20%Pr-TiO₂ sample indicated the presence of Pr species over the surface. The XPS spectrum of Ti2p and Pr3d are shown in Figure 30 and Figure 31. Ti⁺⁴ peaks have been observed at 459.3 and 465.0 eV for Ti 2p_{3/2} and Ti 2p_{1/2} respectively. These peaks also have satellite peaks. These results are in correlation with the results in the literature [220, 221].

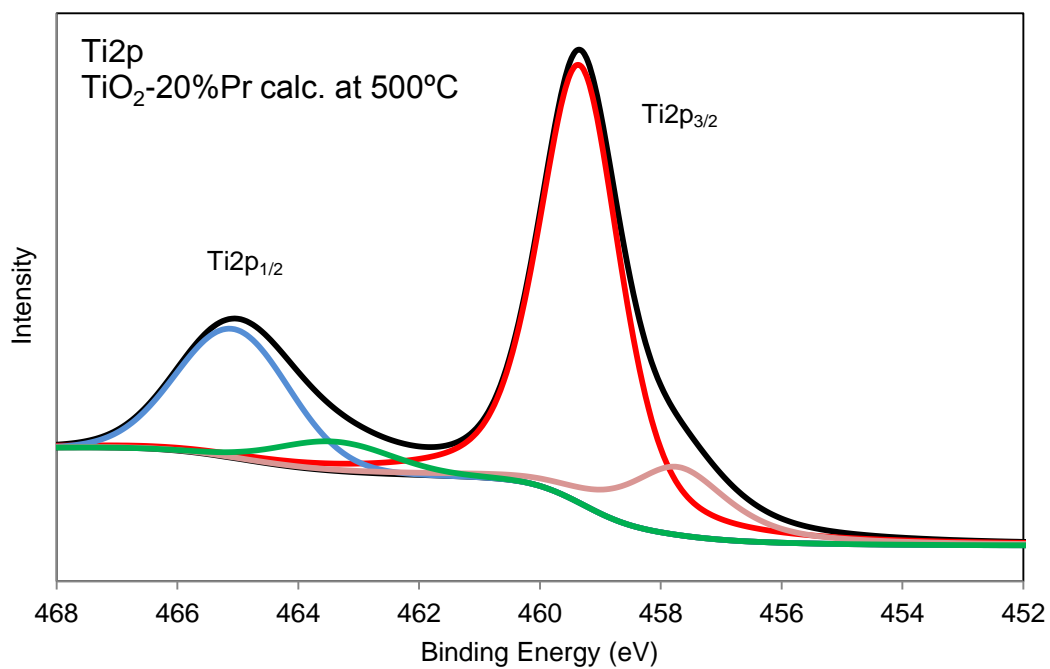


Figure 30: XPS Ti2p spectrum of TiO₂-20%Pr calcined at 500°C

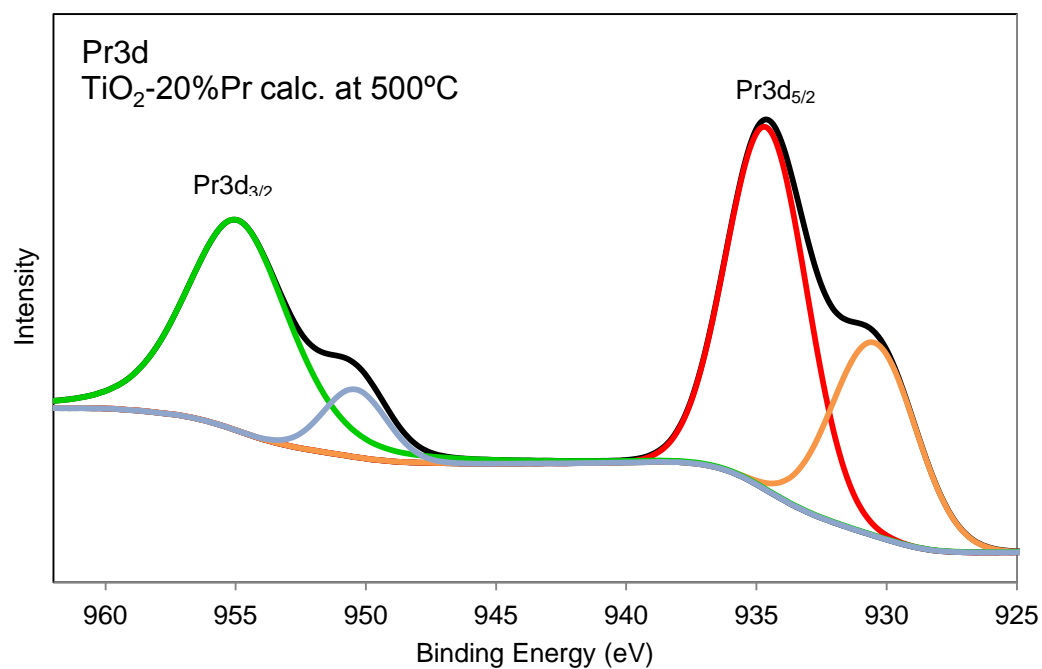


Figure 31: XPS Pr3d spectrum of TiO₂-20%Pr calcined at 500°C

The O1s spectrum of 20%Pr-TiO₂ calcined at 500°C is shown in Figure 32. It can be seen that the main component of the peak is at 530.8 eV. This peak is designated for both TiO₂ and PrO₂. There is also seen a shoulder of this peak at 532.3 eV which can be attributed to the OH⁻ groups on the surface [220, 222]. For the catalyst calcined at 600°C, it can be observed that besides those two peaks there is another peak at 534.2 eV (Figure 33). This peak is assigned to the Pr⁺³ species which can be explained as the formation of Pr₂O₃ as a result of calcination at 600°C [222]. The Pr3d region (925 – 962 eV) two characteristic peaks for Pr3d_{5/2} and Pr3d_{3/2} at 934.6 and 955.0 can be observed with satellite peaks in the lower energies. These results are in good agreement with the ones in the literature [223-225]. These satellite peaks are observed in PrO₂ whereas they disappear by the formation of Pr₂O₃ [226]. Although it can be observed in O1s spectra, Pr₂O₃ started to form at 600°C, since there is still PrO₂ in the structure those satellites are still observed in Pr3d spectra. There is a strong relation between the crystallite size and binding energy. The binding energy for Pr3d_{5/2} peak suggested increasing with decreasing crystallite size [223]. The maximum limit for this increase in the binding energy is 935 eV and for the bulk for it is reported as 933.2 eV [227]. In our study the binding energy is found to be 934.6 and this shows us that the crystals are very small. When Pr4d spectrum is investigated we examine the peak at around 116.5 eV (Figure 34) that is in agreement with Dalai et. al observed [228]. However, this peak cannot be characterized well since it is so small and affected by the background too much.

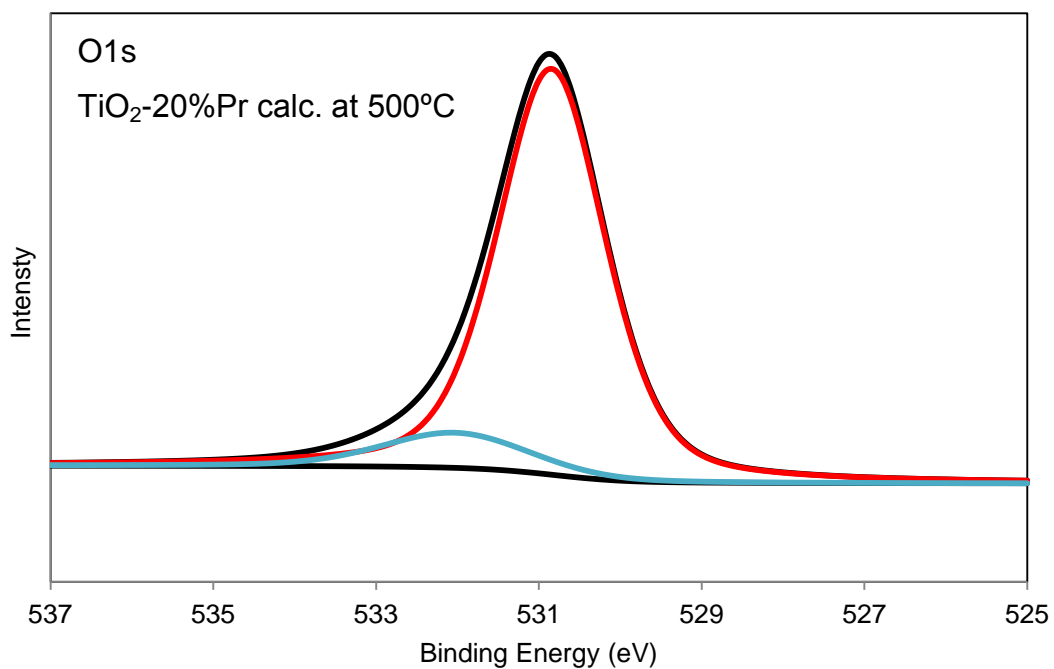


Figure 32: XPS O1s spectrum of TiO₂-20%Pr calcined at 500°C

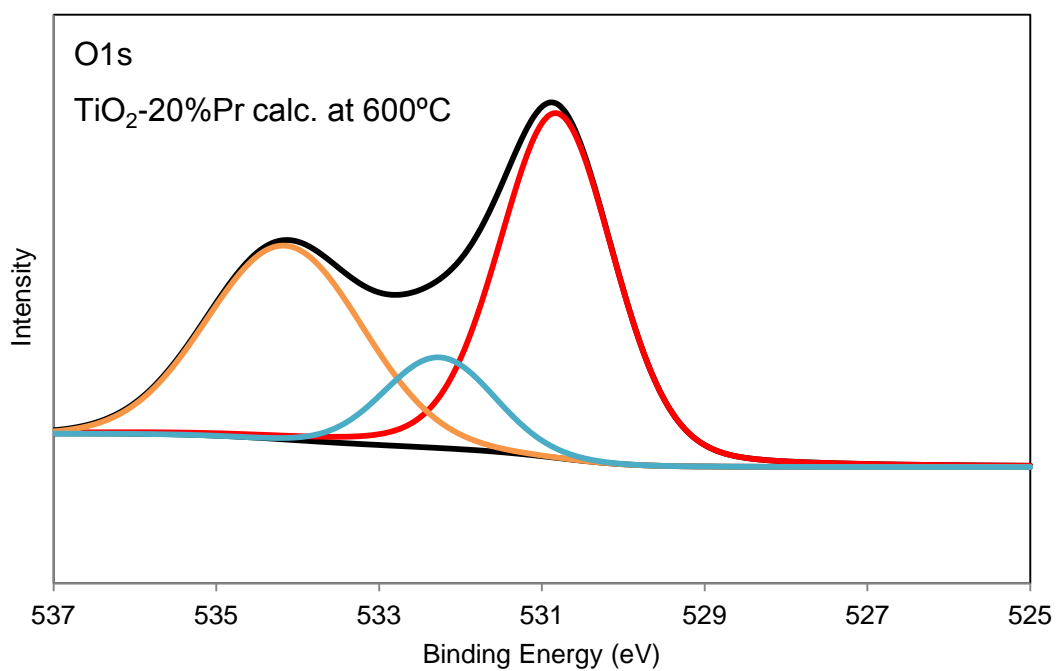


Figure 33: O1s spectrum of TiO₂-20%Pr calcined at 600°C

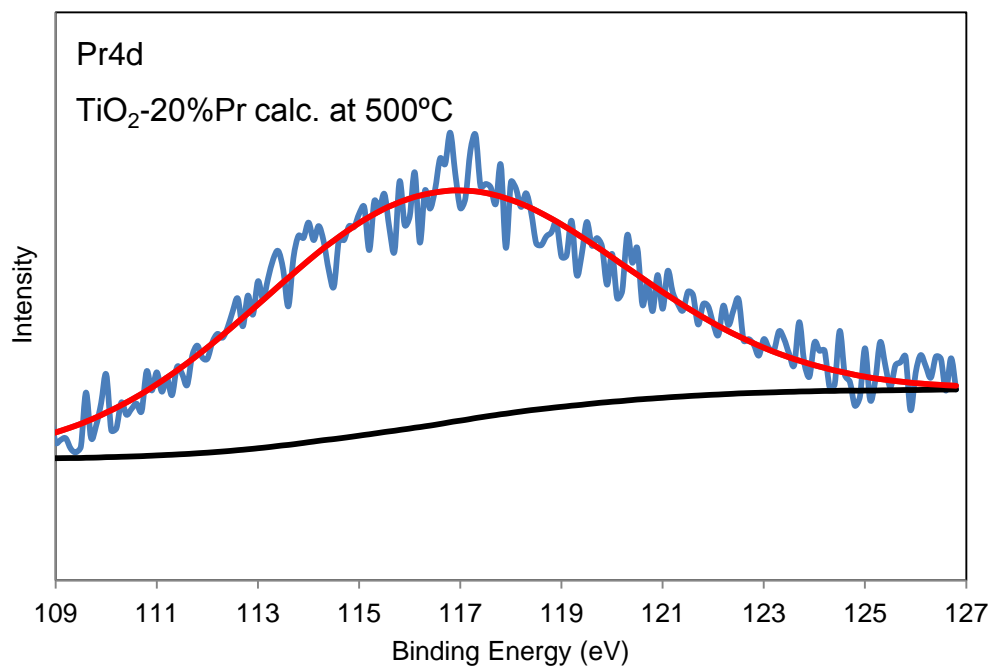


Figure 34: XPS Pr4d spectrum of TiO₂-20%Pr calcined at 500°C

These results were also confirmed by XRD analysis of the 20%Pr-TiO₂ sample. When the XRD data of the samples containing 20% Pr is analyzed, the presence of PrO₂ and Pr₂O₃ phases are evidenced. The peaks are small and making a good characterization is hard but according to the results it can be said that after calcination at 500°C most of the praseodymium is in PrO₂ form and the increase of calcination temperature to 600°C cause formation of Pr₂O₃. The sample calcined at 500°C, the composition is calculated as 0.7% Pr₂O₃, 7.1% PrO₂ and 92.2% TiO₂ (Anatase). For the sample calcined at 600°C, the composition is determined as; 1.9% Pr₂O₃, 5.0% PrO₂ and 93.1% TiO₂ (Anatase).

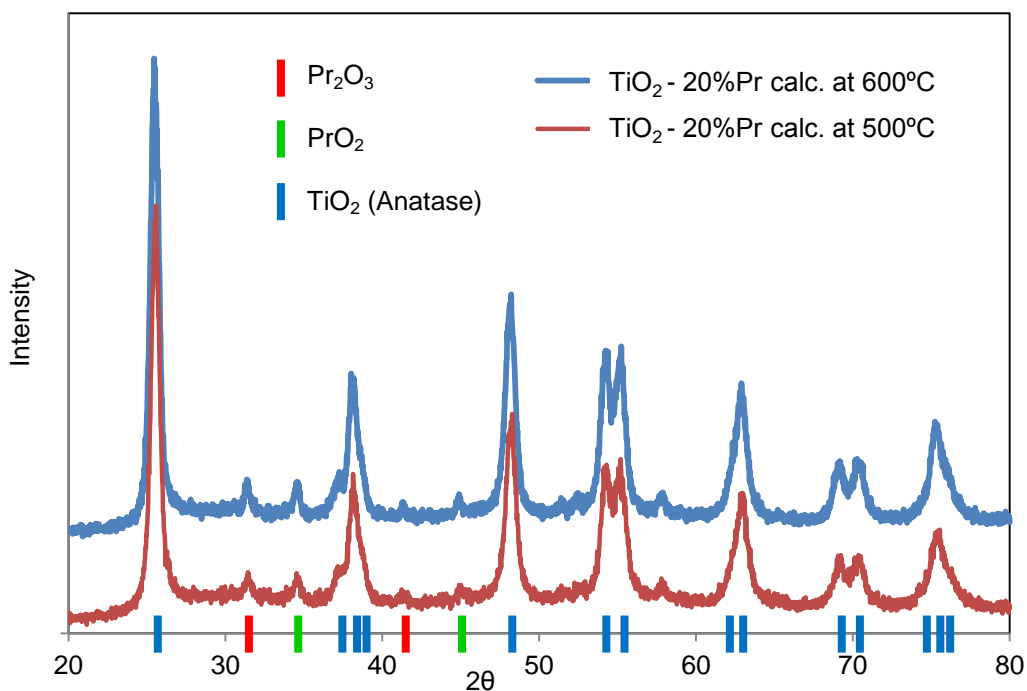


Figure 35: XRD spectrums of TiO₂-20%Pr catalysts calcined at 500, 600°C

4.1.4. Photoluminescence

Photoluminescence (PL) spectrums for pure TiO₂ and 1%Pr-TiO₂ powder and thin film samples which are calcined at 600°C were obtained to examine the excitation states of the samples (Figure 36, Figure 37). Powder samples were fixed over glass holders using adhesive tapes. When the samples are excited with 320nm HeCd laser, 1%Pr-TiO₂ powder sample demonstrated two emission peaks at 608 and 620 nm 2 peaks compared to pure TiO₂ (Figure 36). In order to ensure and eliminate the possibility of interference, the PL spectra of adhesive tape and the holder were also examined. As it is seen form Figure 53, the peaks at 608 and 620nm are specific emission peaks to the 1%Pr-TiO₂ powder sample. When the PL spectra of pure TiO₂ is compared with 1%Pr-TiO₂ sample, it can be clearly stated that two emission peaks are contributed by the presence of Pr. The PL spectrum of thin film samples were also obtained by using 320nm HeCd laser as excitation source

(Figure 37). The thin film samples also revealed the same peaks between 608-620 nm for 1%Pr-TiO₂ sample with better resolution and spectral quality. These peaks show that intermediate energy states are formed in the band gap of the structure that can lead photon conversion. In photoluminescence tests, samples are excited by HeCd laser with a wavelength of 320nm and any emission below the excitation wavelength cannot be observed by the long pass filter used to prevent the detection of excitation beam. Therefore, photons emitted by the samples that have a lower wavelength than 325nm could not be observed by the PL spectrometer that was configured for visible region. Electron excited to the conduction band emits photons during spontaneous de-excitation process. The de-excitation process may occur stepwise through intermediate levels in the band gap emitting lower energy luminescent photons. The 2 peaks at 608 and 620 nm observed in the PL spectrum might be accounted as the proof of intermediate energy states formed in the band gap structure of the catalyst by Pr doping.

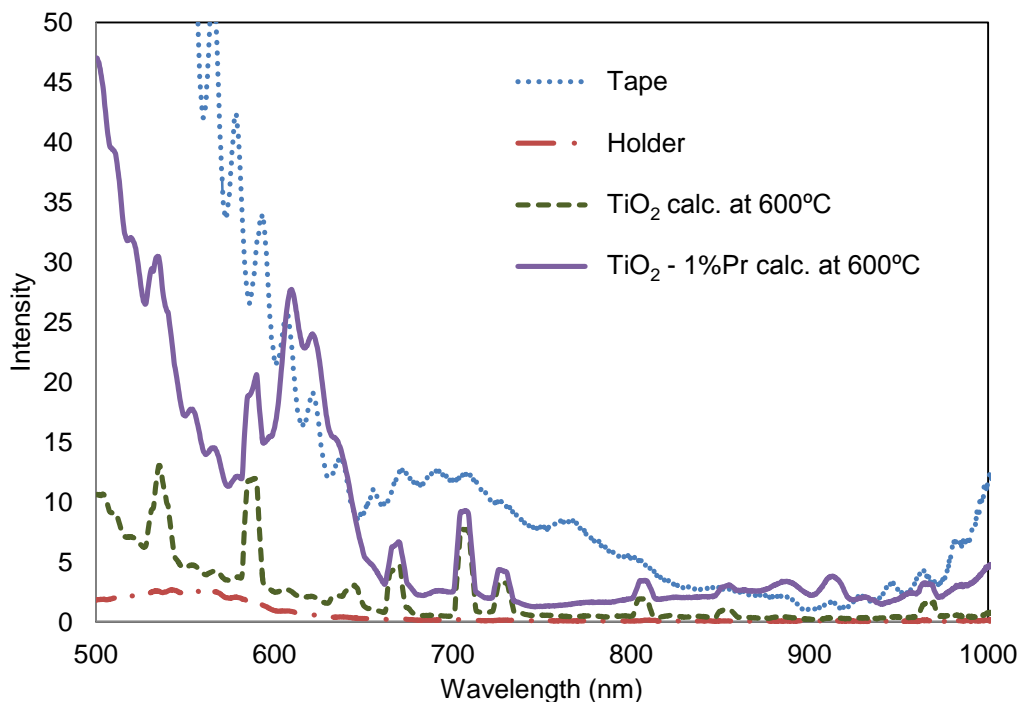


Figure 36: Photoluminescence spectrums for T600 and P600 powder samples.

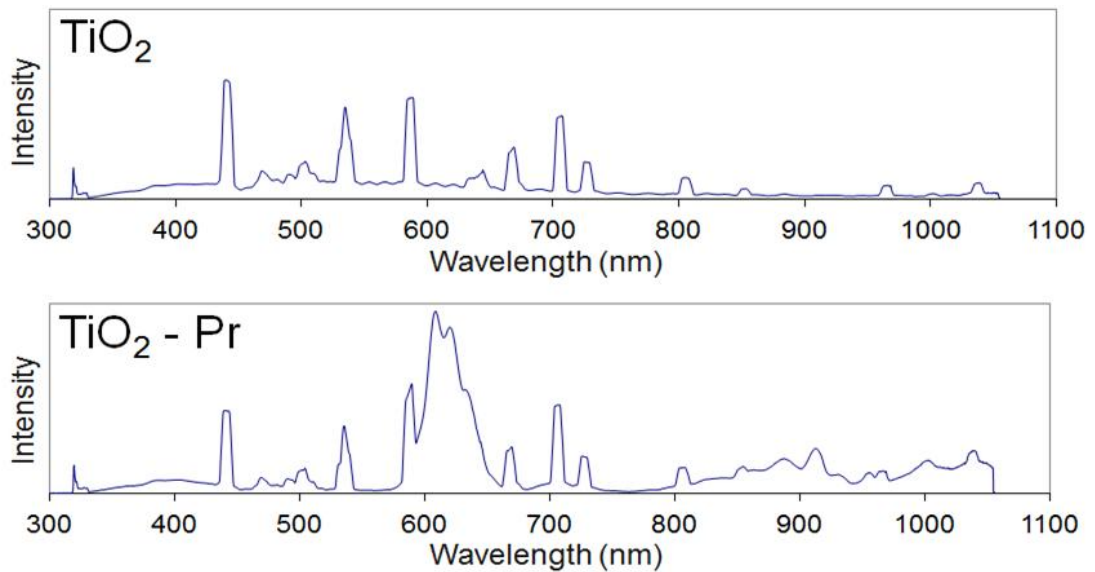


Figure 37: Photoluminescence spectrums for T600 and P600 thin film samples.

4.1.5. Photoresponse

Photoresponses of the samples were also studied in order to observe any possible shift on the band gap as a result of praseodymium addition. The photoresponse curves of the thin film samples were obtained with respect to the wavelength of the excitations source. The tungsten lamp and monochromator was used as excitation source. The conductivity measurements of the thin films were carried under constant DC voltage 5V by measuring current across the two electrodes attached to the sample by using silver glue. Conductivity versus wavelength of the incident light is shown in Figure 38. As it is seen from figure, all TiO_2 and 1%Pr- TiO_2 samples absorb light between 300 – 400nm and their conductivity increases as a result of excitation of the valence electrons. Highest conductivity was obtained for sample containing 5% praseodymium which is calcined at 600°C. It is observed that the conductivity consistently increases with the addition of Pr in the titanium dioxide photocatalysts. The calcination

temperature also affects the conductivity. The conductivity of praseodymium containing samples increases with calcination temperature. However the conductivity of pure TiO₂ samples decreases with calcination temperature which can be attributed to the rutile formation. Rutile although it can absorb a wider range of the solar spectrum because of its lower band gap, has a lower light absorption capacity than anatase [45], leading fewer electrons excited to the conduction band and a lower electrical conduction.

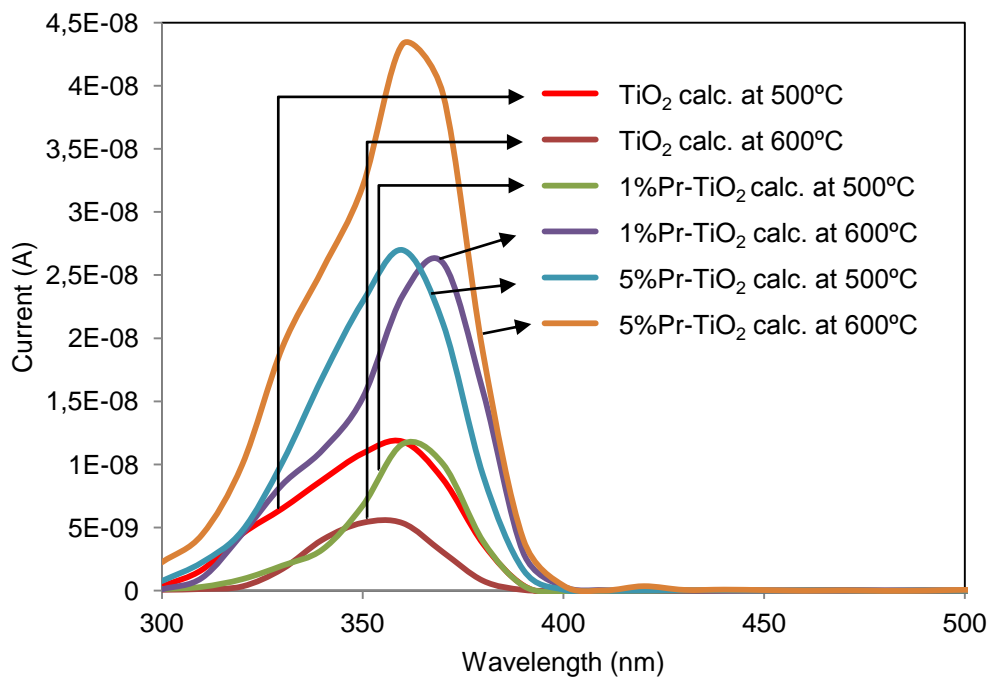


Figure 38: Photoresponse curves for different catalysts

The band gap energy of the samples can be calculated by using photoresponse data. The data can be analyzed to observe direct and indirect band gap energy by using appropriate methods. The wavelength can be converted to energy (eV) by using the following relationship;

$$E = \frac{1239}{\lambda(nm)} \quad (23)$$

For semiconductor samples having a direct band gap structure, the intercept of $(E \times I)^n$ versus E graph yields the band gap energy. The value for n can be chosen as 2 and $\frac{1}{2}$ for direct band gap and indirect band gap, respectively. The photocurrent data is converted to band gap plots and direct band gap plot (n=2) is shown in Figure 39 and indirect band gap plot (n=1/2) is shown in Figure 40.

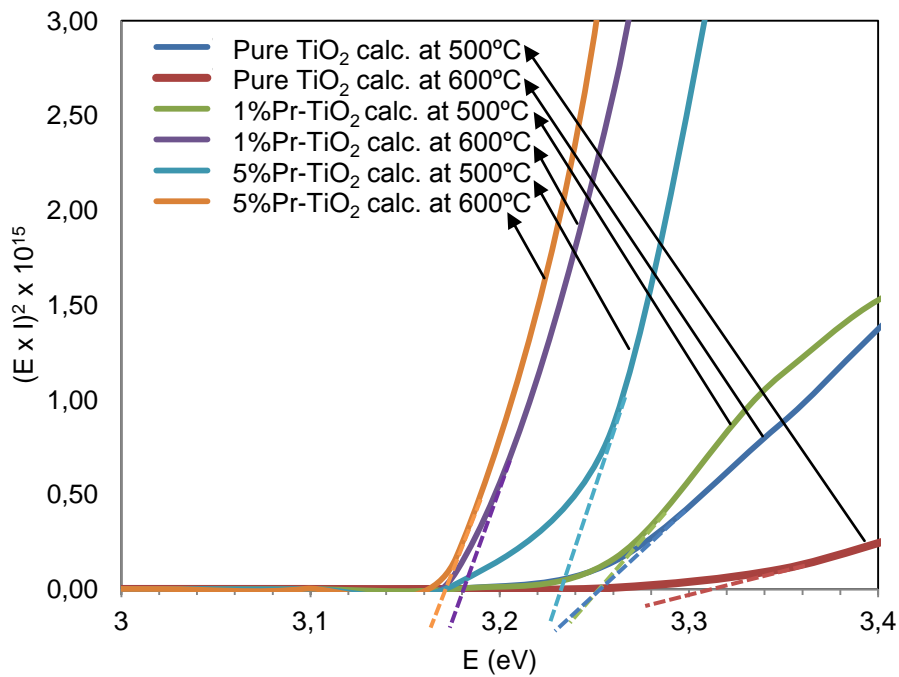


Figure 39: Band gap calculation graph for direct band gap model

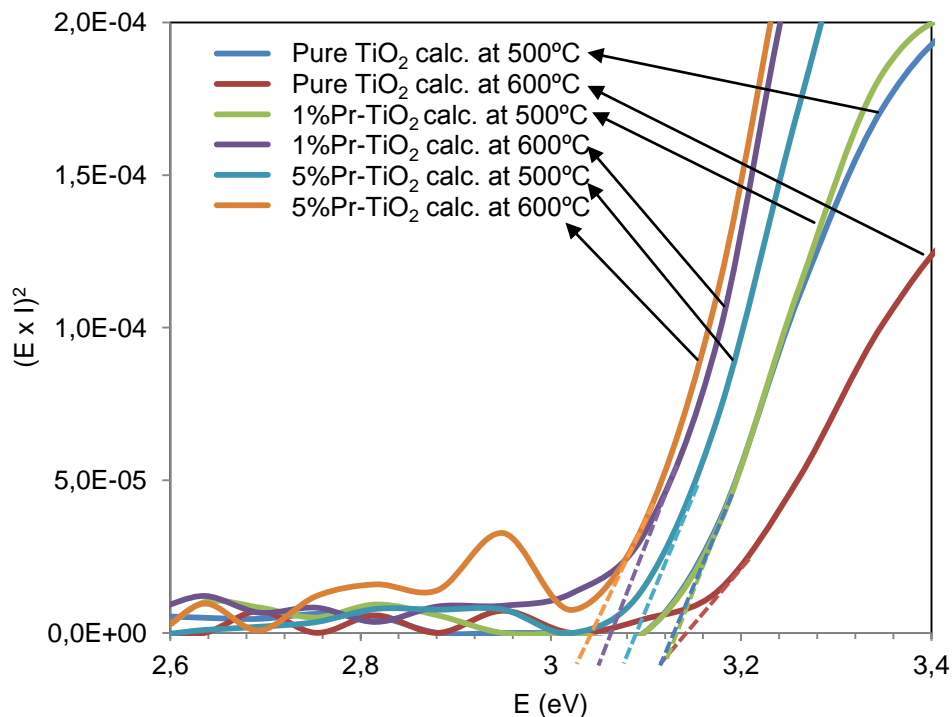


Figure 40: Band gap calculation graph for indirect band gap model

Many publications report that TiO_2 rutile structure has a direct band gap of 3.06 eV and an indirect one of 3.10 eV and the anatase has only an indirect band gap of 3.23 eV [55, 56]. However, there are also contrary results showing that anatase has a direct band gap [57]. For anatase, different values of the band gap have been reported by many publications from 2.86 to 3.34 eV for the anatase phase, and the differences explained with the variations in the stoichiometry of the synthesis, the impurities, crystalline size and the type of electronic transition [49, 229]. The band gap values obtained for the samples are tabulated in Table 12. It can be seen that praseodymium doping cause a decrease in the band gap energy for both direct and indirect band gap models. Decreasing band gap energy is favorable and increases the photocatalytic activity since light absorption capability of the catalyst increases towards visible region. It is also observed that the Pr doped samples calcined at 600°C has lower band gaps than the ones calcined at

500°C, whereas for the pure TiO₂ catalyst, increasing the band gap energy significantly for the direct band gap, and slightly for the indirect band gap. This can be because of the rutile formation. The band gap values obtained 3.17-3.31 eV for the direct band gap and 3.04-3.14 eV for the indirect band gap is comparable with the band gaps of anatase and rutile respectively.

Table 12: Band Gap Energies for the catalysts

| Catalyst | Direct Band Gap (eV) | Indirect Band Gap (eV) |
|--------------------------------------|-----------------------------|-------------------------------|
| Titania calcined at 500°C | 3.25 | 3.13 |
| Titania calcined at 600°C | 3.31 | 3,14 |
| Titania with 1% Pr calcined at 500°C | 3.25 | 3.13 |
| Titania with 1% Pr calcined at 600°C | 3.18 | 3.06 |
| Titania with 5% Pr calcined at 500°C | 3.23 | 3.09 |
| Titania with 5% Pr calcined at 600°C | 3.17 | 3.04 |

4.1.6. TEM Analysis

TEM analyses of the samples were performed by using HRESTEM and STEM modes. STEM mode was employed to obtain energy dispersive X-Ray spectroscopy (EDX) for mapping and point analysis for Pr and Ti in the structure. Particles around 10 - 15 nm diameter were observed in STEM that is in agreement with XRD crystal size calculation and EDX analyses are performed on these particles. The samples are prepared by dispersing powder sample in ethanol and dipping copper grids.

In the high resolution TEM imaging, for the catalyst containing 1%Pr and calcined at 600°C, it was observed that particles are smaller than 20nm and size distribution seems to be homogeneous (Figure 41). Also it was observed that the particles resemble octahedral shape which is well known crystal geometry of anatase. Some crystal planes can be observed in the HRTEM pictures. The interplanar spacings of these planes observed are measured. Some of these interplanar spacings are measured as; 3.5, 4.7 and 1.9 which correspond to (1 0 1), (0 0 2) and (2 0 0) planes of anatase structure respectively. Also (1 0 1) and (0 0 2) planes can be observed in the same crystal with an angle of 68.3° between them. This angle is in agreement with the calculated angle between these planes and also in agreement with the values in the literature [230, 231]. In the HRTEM imaging, for the catalyst containing 20%Pr and calcined at 600°C, interplanar spacings of 3.5 and 1.9 corresponding to (1 0 1) and (2 0 0) planes of anatase can still be observed (Figure 42). These results show us that anatase structure is present in both catalysts that is consistent with the XRD results.

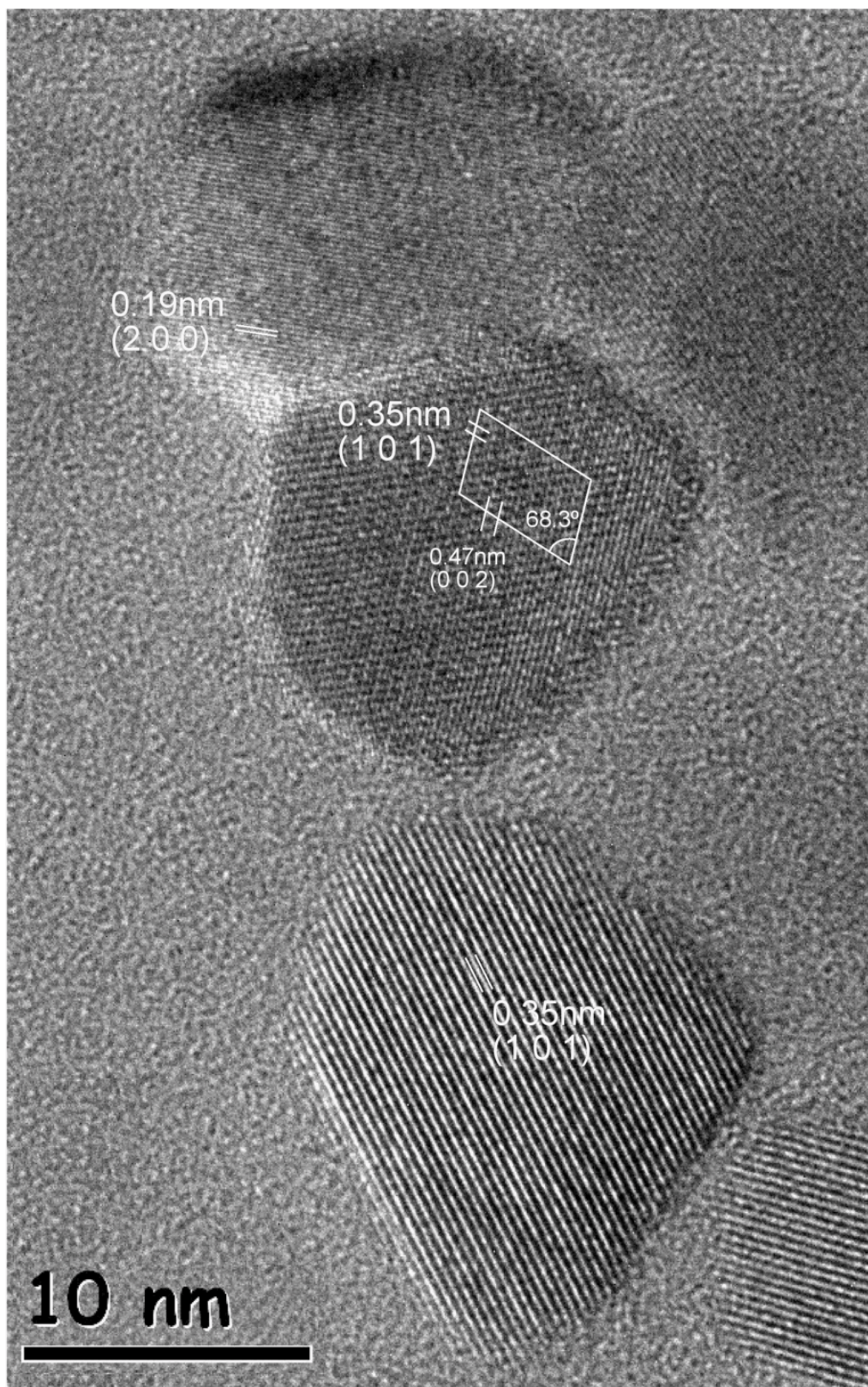


Figure 41: HRTEM photo of the catalyst containing 1%Pr and calcined at 600°C



Figure 42: HRTEM photo of the catalyst containing 20%Pr and calcined at 600°C

The principal X-Ray emission lines for Ti, O, and Pr are shown in Table 13. Cu, C and O are also included in the table to clarify possible interference by the presence of Cu grid, organic film on the copper grids and instrument background. EDAX analysis in the STEM mode showed homogeneous distribution of Pr and Ti atoms in the structure of the 20%Pr-TiO₂ catalyst calcined at 600°C (Figure 43). This shows that catalyst preparation was successfully made and the catalysts synthesized are highly homogeneous. Also from these results it cannot be claimed that growth of the crystals are inhibited by the praseodymium atoms occupying the grain boundaries since it seems to be homogeneous over the complete crystal structure. Another approach is needed to explain the phase stabilization effect of praseodymium, but the experimental data obtained in this study is not enough to fully explain how this phase stability occurs. EDAX analysis of the complete area had shown 77.4%Ti and 22.6%Pr atoms in the structure that is close to the prepared catalysts desired composition of 20%Pr.

Table 13: The principal X-Ray emission energies.

| | Ti | Pr | O | Cu |
|---------------|-------|-------|-------|-------|
| Energies (eV) | 4.510 | 5.033 | 0.523 | 8.040 |
| | 4.931 | 5.488 | 0.532 | 8.904 |
| | 4.964 | 5.849 | | 8.979 |
| | 0.452 | 5.962 | | 0.930 |
| | 0.454 | 6.438 | | 0.933 |
| | 0.460 | 6.833 | | 0.953 |
| | 0.530 | 0.929 | | 1.100 |

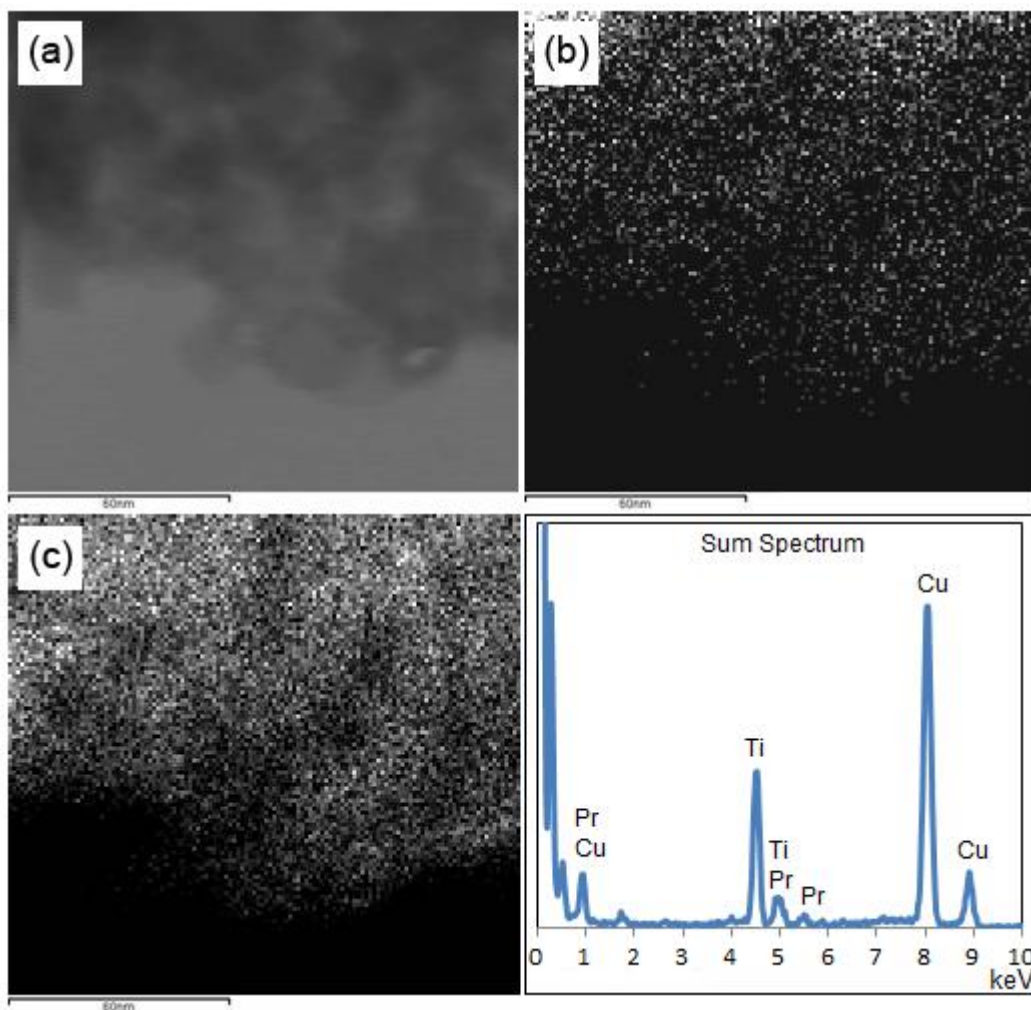


Figure 43: a) STEM image, Elemental mapping of 20%Pr-TiO₂ b) Pr, c) Ti, d) Sum EDX spectrum

Detailed point EDAX analysis of the samples has been carried out using electron beam diameter of 2nm which is very narrow area compared with the particle 10-15nm particle size. The point EDAX analysis revealed that particles have homogeneous distribution of Pr and Ti atoms in the structure for 20%Pr-TiO₂ sample.

Some particles in the catalyst containing 20%Pr were observed to be containing no Ti atoms in it but only Pr. These are isolated particles that are

composed of PrO_2 or Pr_2O_3 . This might be because at this high Pr concentration some Pr atoms cannot get into the structure and create PrO_2 crystals. These crystals might be the reason of the Pr_2O_3 observed in the XRD analysis after calcination at 600°C .

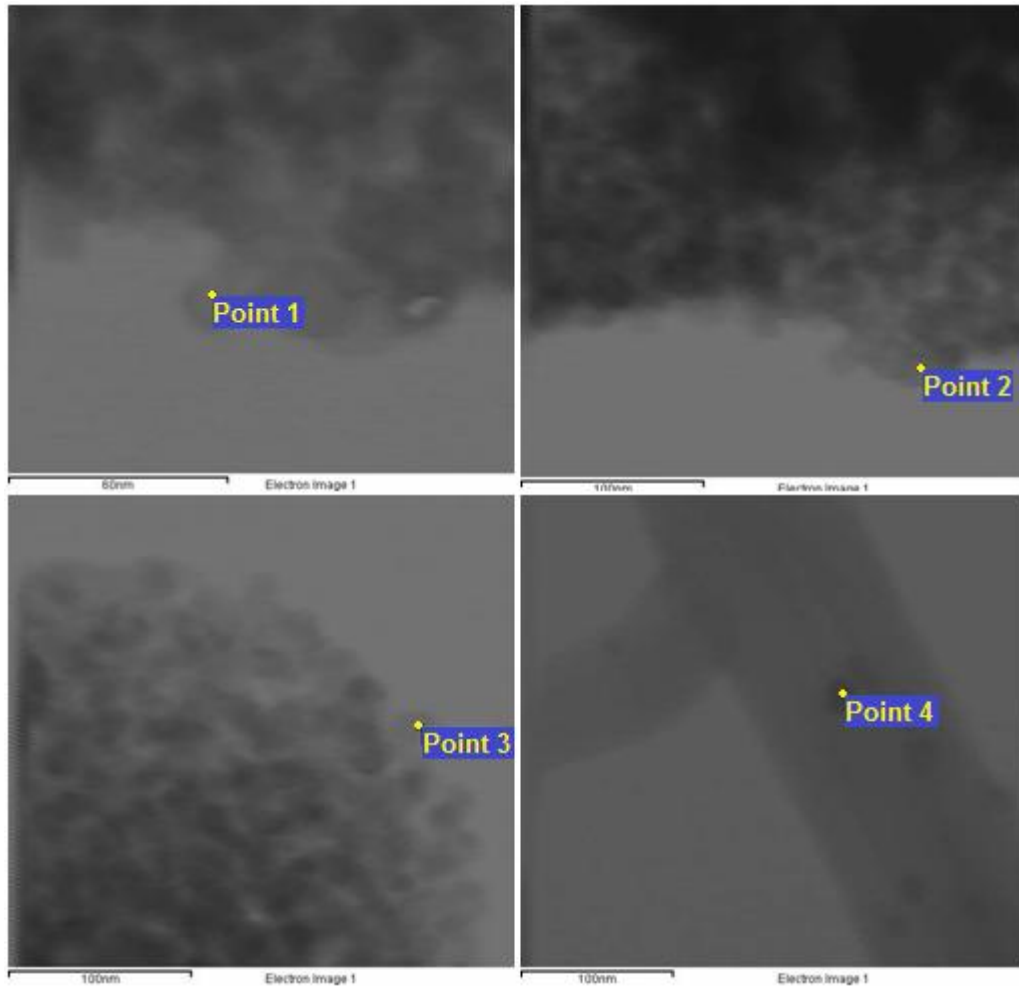


Figure 44: Point EDX analysis with 2nm beam for Pr and Ti with weight percentages; point 1: 77.5%Ti, 22.5%Pr, point 2: 87.8%Ti, 12.2%Pr, point 3: 76.1%Ti, 23.9%Pr, point 4: 3.3%Ti, 96.7%Pr.

4.2. Photocatalytic Activity Tests

4.2.1. Methylene-Blue Degradation Test for Powder Samples

The photocatalytic activities of the samples were determined by using Methylene Blue degradation method. The methylene blue degradation tests were performed by adding 0.1 grams of catalyst samples into 250 ml of 2ppm methylene blue solution in 250 ml bakera. The reaction is performed batchwise under 300 W/m^2 artificial solar irradiation between 280-780nm wavelengths. The samples are collected periodically every 30 minutes and analyzed in UV-Vis spectrometer after the removal of catalyst particles by precipitation and filtering.

The major absorption peaks of methylene blue are at 600nm and 666nm (Figure 45). Jockusch et al. studied the aggregation of methylene blue and the peak maximum at 666 nm is designated for monomer, 600 nm for dimers and at 550 nm for higher order aggregates [186]. Dimerization of methylene blue increases with its concentration. Murugan et. al. also observed the dimerization of methylene blue in their studies on methylene blue degradation over TiO_2 and found that dimerization highly decreases the degradation rate [187]. Also Methylene blue has a peak maximum at around 293 but this peak is not used in calculations since there can be more experimental error in that region because of the absorption of quartz cuvettes used and for the thin film samples the absorption of glass substrates that the thin film is coated on.

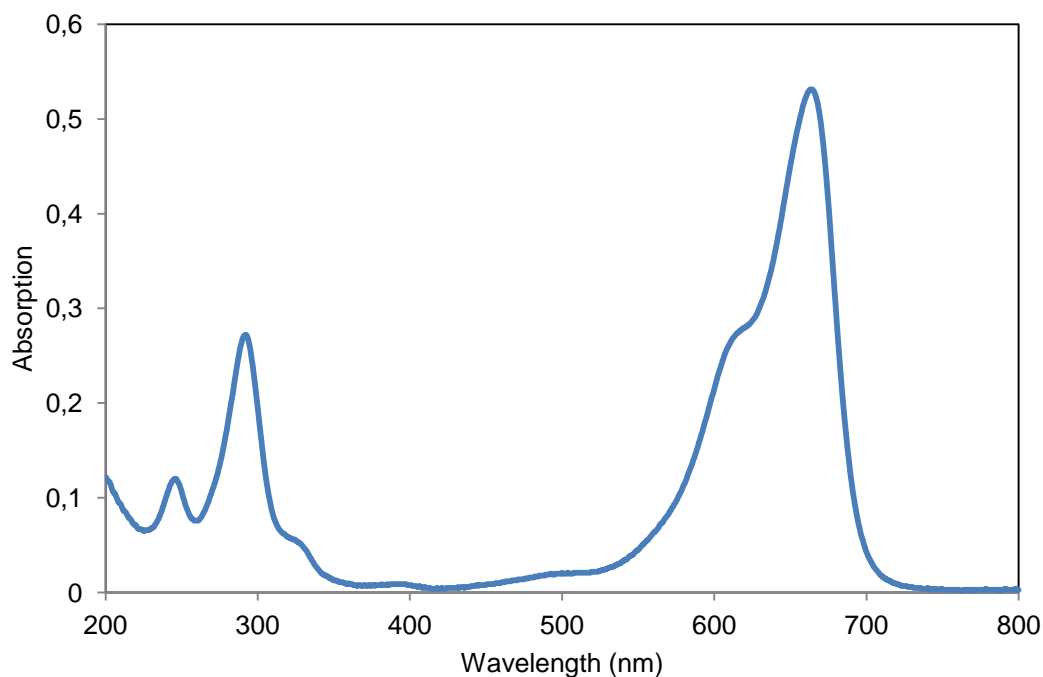


Figure 45: UV-Visible Spectra of 2 ppm methylene blue solution

During the reaction time, the concentration of methylene blue was determined by the absorbance of reaction solution at 666nm and comparing with the calibration curve. The photocatalytic degradation of methylene blue by using pure TiO_2 and Pr-doped TiO_2 samples are shown in Figure 46. It can be clearly stated that pure TiO_2 samples have higher initial activities than the Pr doped counterparts. However, the activity of pure TiO_2 samples decreases with time and reaction is not completed resembling catalyst deactivation. On the other hand, reaction on Pr doped samples having lower initial photocatalytic activity at the beginning and complete degradation of methylene blue was achieved at 150 and 240 min for samples calcined at 600°C and 500°C respectively.

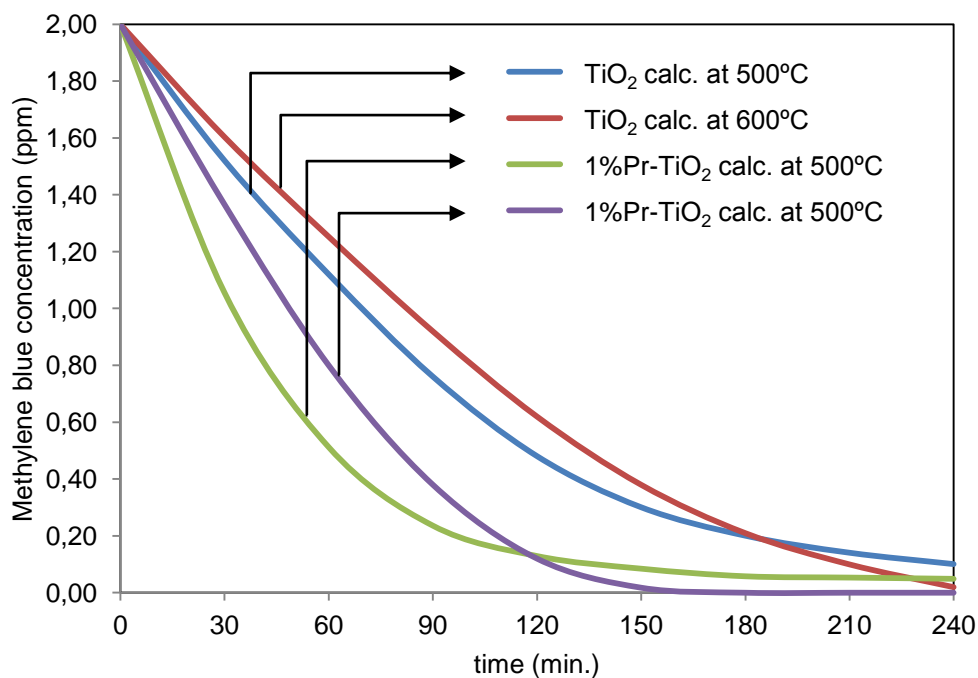


Figure 46: Methylene blue degradation on powder catalyst with time

The relative change of methylene blue dimer and monomer concentrations can be analyzed by detailed UV-Visible spectra of the reaction mixtures. As it is shown in Figure 47 -Figure 50, there is a strong relation between the dimer and monomer concentrations. Methylene blue in monomer form degrades faster than dimer form and dimer form decomposes to monomer with the reaction progress. Since dimers are larger molecules than monomers, their adsorption is slower over the catalyst and cannot penetrate to the smaller pores. The liquid phase analysis is not sufficient to elaborate any conclusion for surface reactions. Another set of degradation reactions were performed by using thin films and surface concentration of methylene blue species were analyzed.

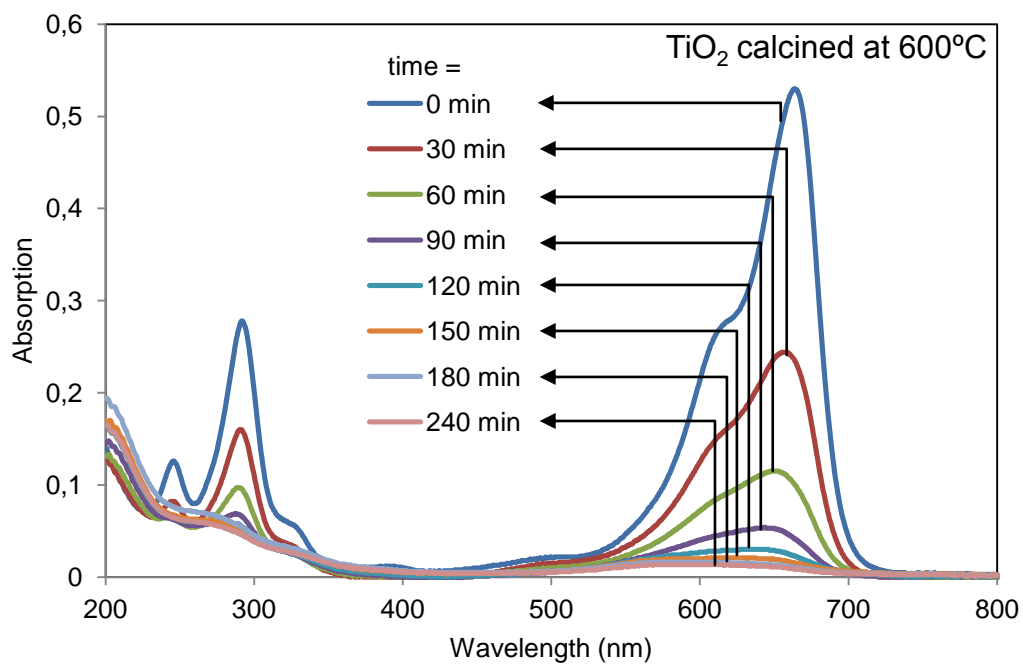


Figure 47: UV-Visible Spectra at different times during the methylene blue degradation test over pure TiO_2 catalyst calcined at 600°C

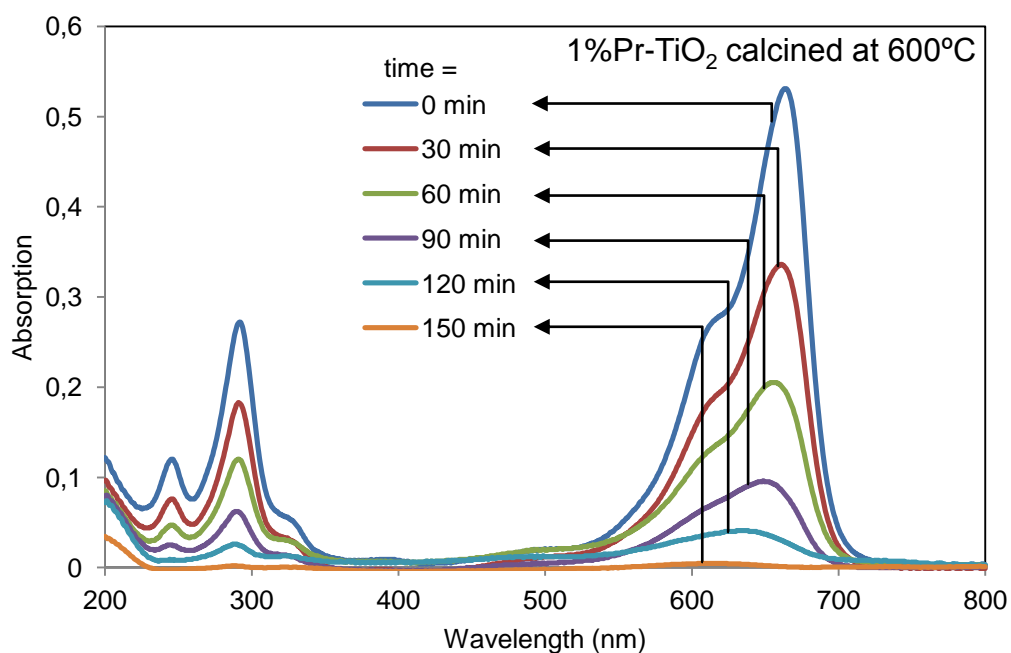


Figure 48: UV-Visible Spectra at different times during the methylene blue degradation test over $1\%\text{Pr-TiO}_2$ catalyst calcined at 600°C .

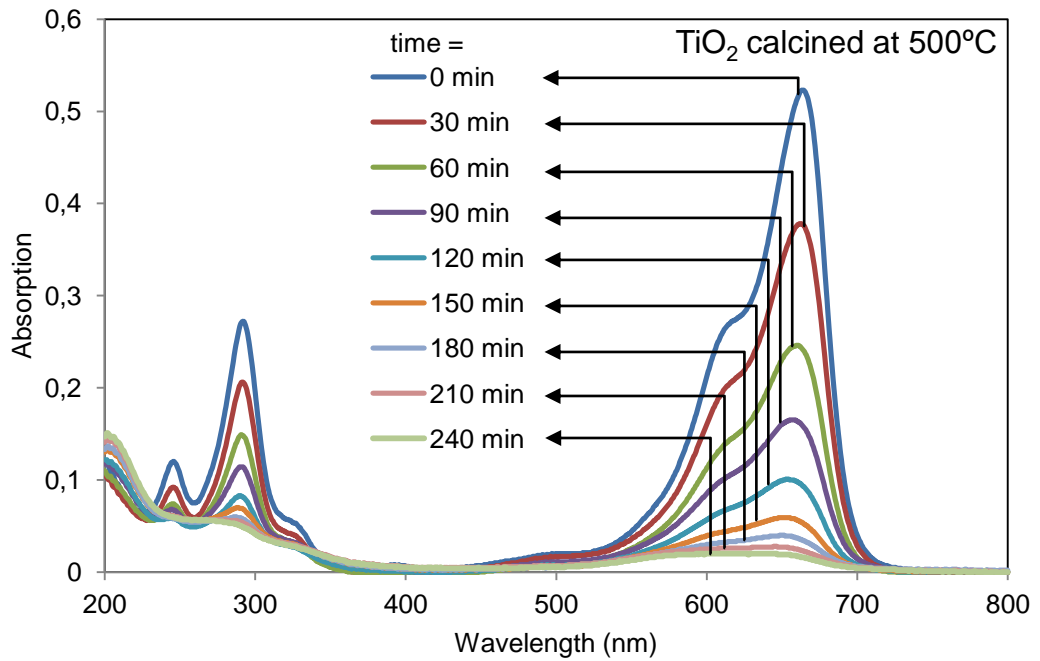


Figure 49: UV-Visible Spectra at different times during the methylene blue degradation test over pure TiO_2 calcined at 500°C .

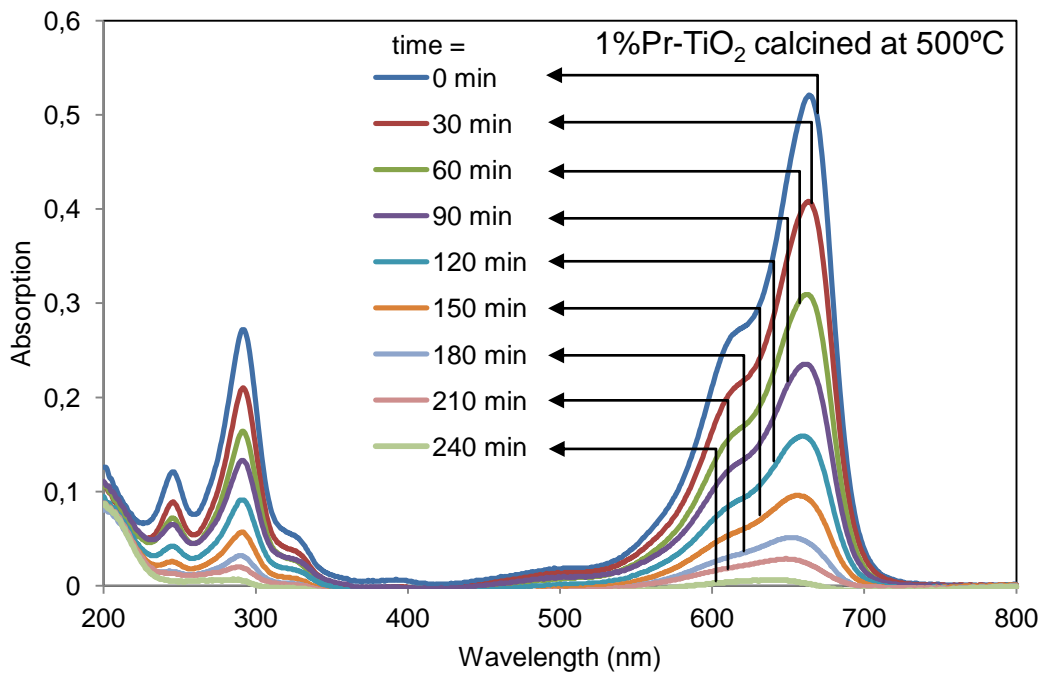


Figure 50: UV-Visible Spectra at different times during the methylene blue degradation test over $1\%\text{Pr-TiO}_2$ calcined at 500°C .

4.2.2. Methylene-Blue Degradation Test for Thin Film Samples

The thin films samples are immersed in 100ppm methylene blue solution in dark for 24 hours and the equilibrium were achieved. The adsorbed methylene blue on thin films was tested under simulated sunlight $300\text{W}/\text{m}^2$ of 280 - 780nm. The methylene blue degradation was followed by analyzing the UV-Vis spectra of the thin film samples. Each spectrum was compared with spectra obtained from the same spot before reaction and the change in the concentration of surface species with reaction time course was obtained. The UV-Vis spectra of the samples are shown in Figure 51. After 24 hours immersion in 100ppm methylene blue solution, the UV-Visible spectra of thin films were also obtained (Figure 52). The difference spectra were obtained and presented in Figure 53 indicating the presence of methylene blue adsorbed dimer and monomer surface species.

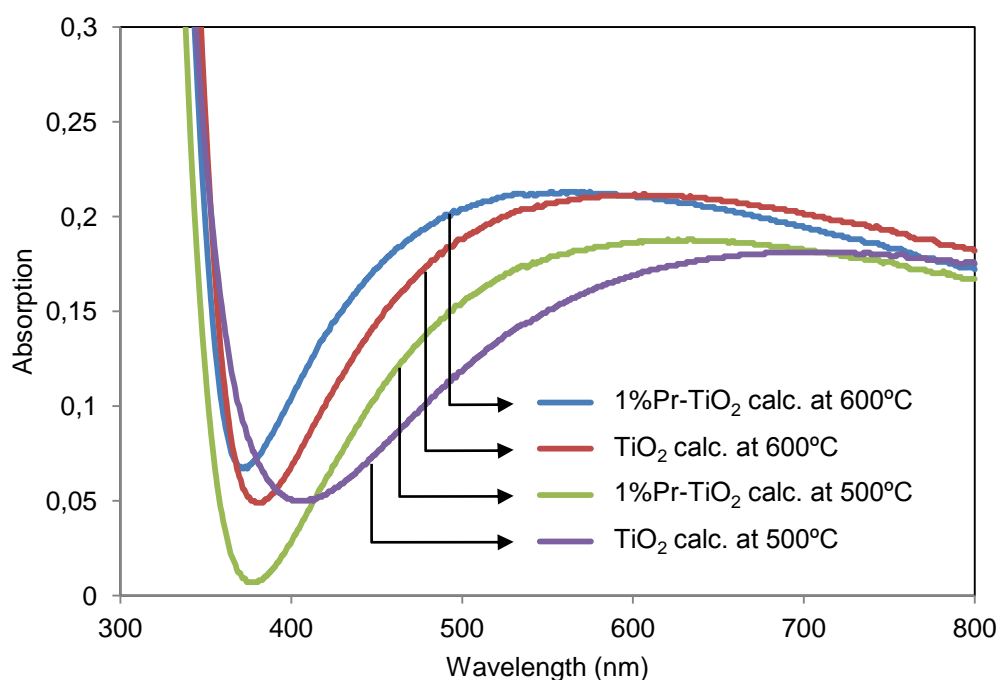


Figure 51: UV-Visible spectra of thin film catalysts

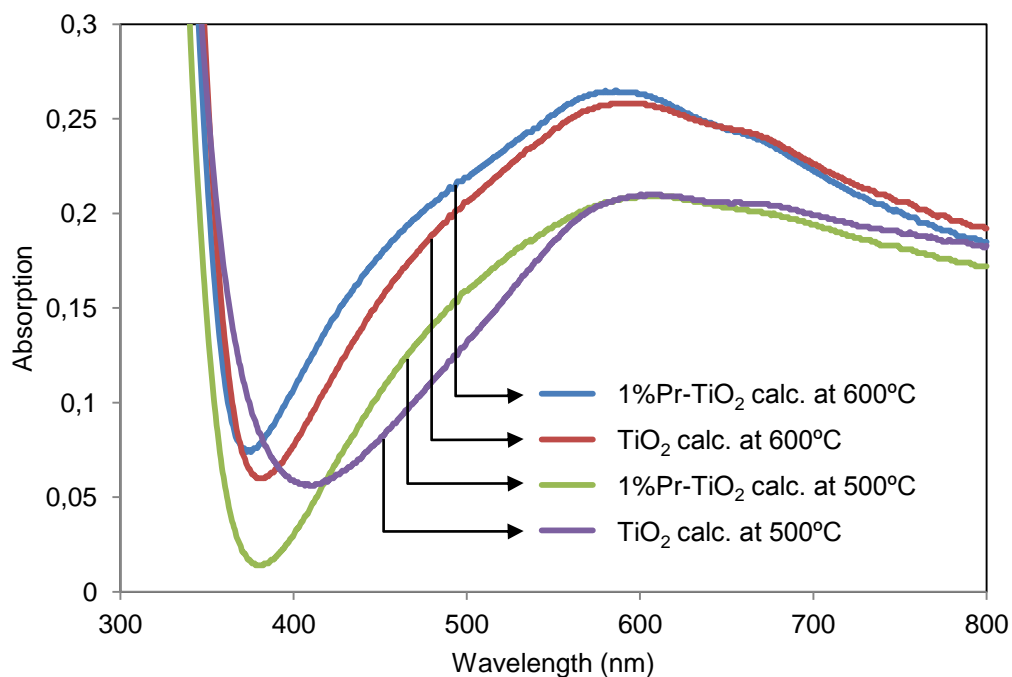


Figure 52: UV-Visible spectra of thin film catalysts after kept in 100ppm methylene blue solution for 24 hours

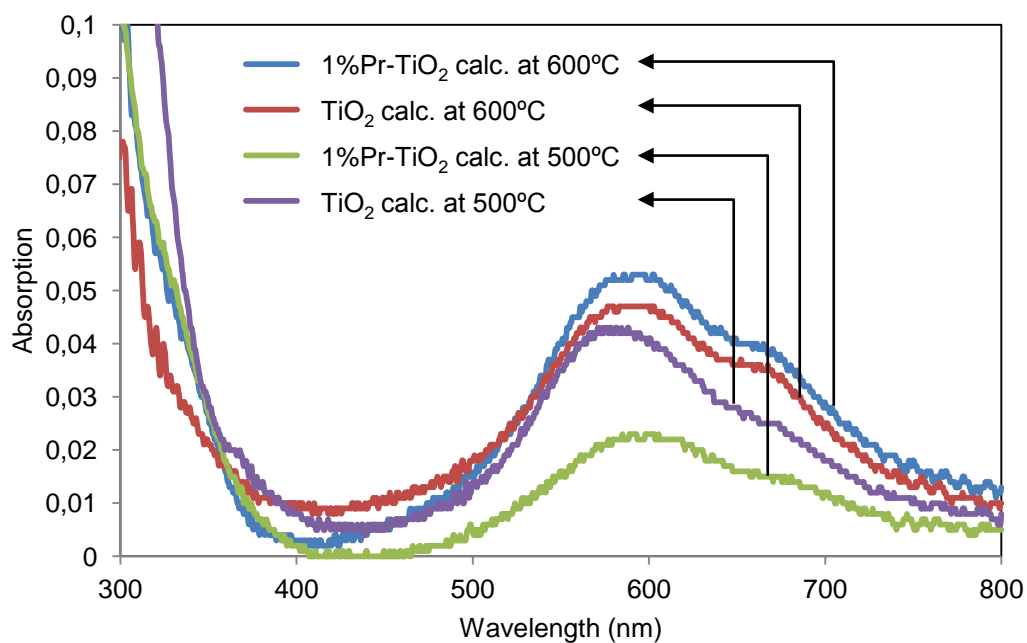


Figure 53: Normalized UV-Visible spectra of thin film samples kept in 100ppm methylene blue solution for 24 hours

Both dimer and monomer species were detected over all catalyst samples. As it is seen from the degradation time courses, the monomer degradation is much faster than the dimer degradation and the dimer degradation is the slower step which limits the reaction rate. (Figure 54 - Figure 57).

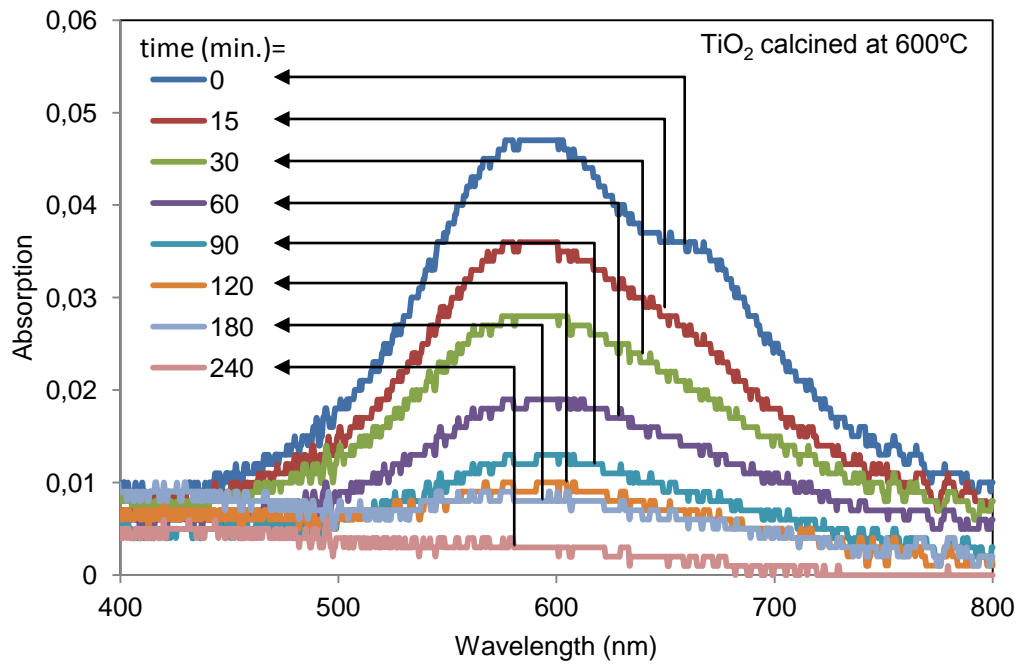


Figure 54: Normalized UV-Visible spectra at different times during the methylene blue degradation test over T600 thin film catalyst

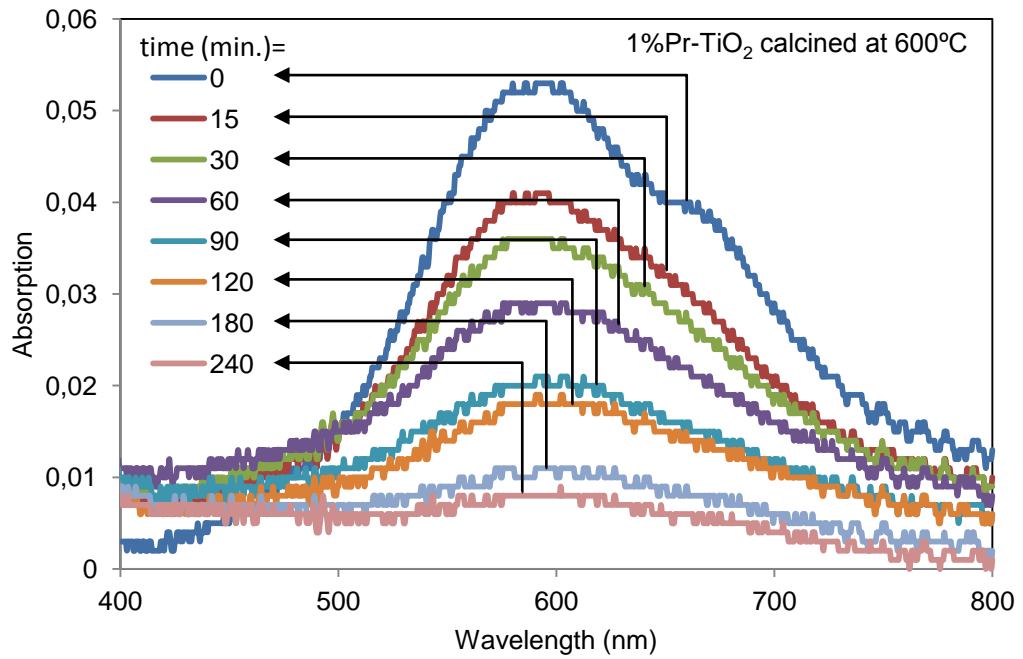


Figure 55: Normalized UV-Visible spectra at different times during the methylene blue degradation test over P600 thin film catalyst

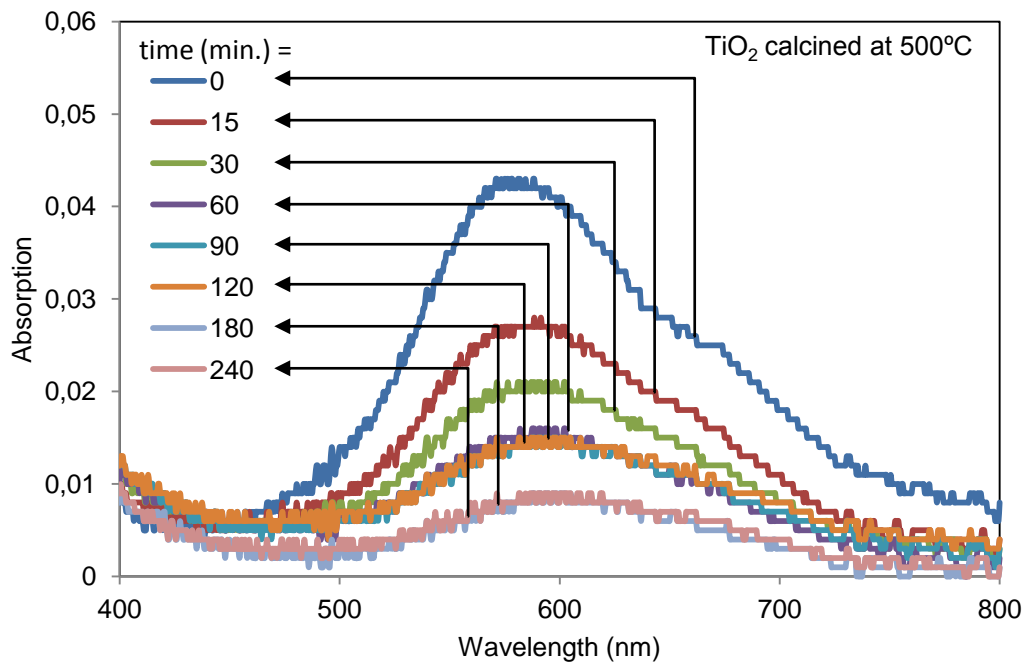


Figure 56: Normalized UV-Visible spectra at different times during the methylene blue degradation test over T500 thin film catalyst

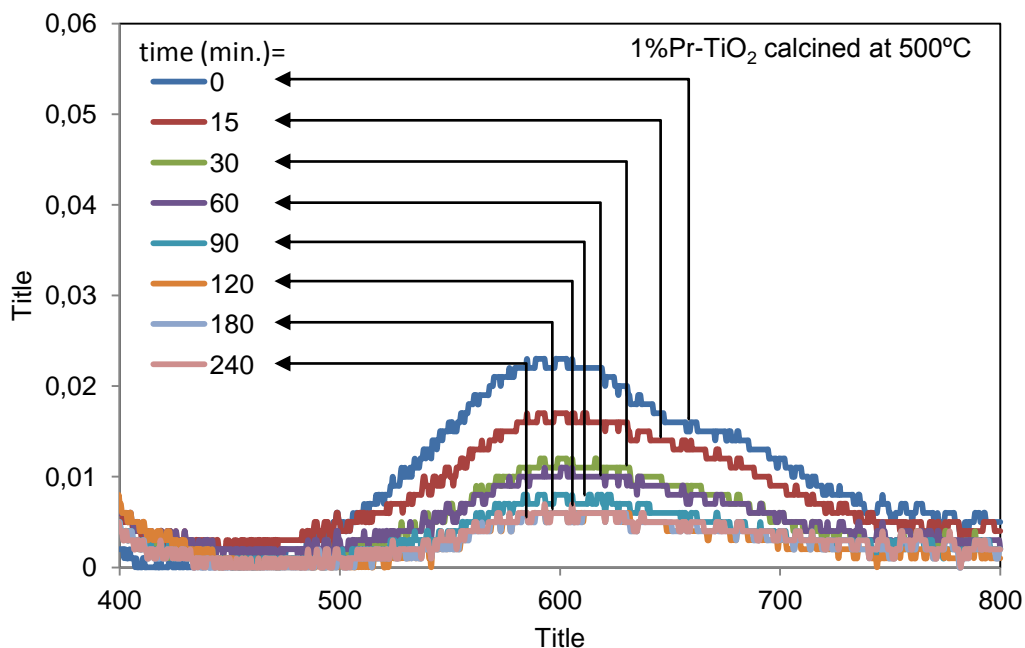


Figure 57: Normalized UV-Visible spectra at different times during the methylene blue degradation test over P500 thin film catalyst

4.2.3. Phenol Mineralization Test for Powder Samples

Another photocatalytic activity test study was performed for phenol mineralization. Phenol mineralization was studied by our research group and methodology was developed [67]. Bayram stated that the complex reaction mechanism and reaction intermediate species cause interference on UV-Vis absorbance spectrums and phenol concentration cannot be measured directly by analyzing the absorbance of phenol at 270nm as many studies in literature performed that way. As it is seen in Figure 58, the UV-Vis spectrum of reaction products interfere and cause an increase in UV-Vis absorbance at 270nm indicating the formation of reaction intermediate having the same electronic transitions with phenol. As seen in the Figure 59, the absorbance at 270nm first increases because of the formation of other species and later tends to decrease. In order to take into account for the reaction

intermediates and their interference at 270nm, the UV-Vis spectrometer was calibrated for possible species such as catechol, hydroquinone, benzoquinone, maleic acid, muconic acid, fumaric acid, oxalic acid according to their specific absorbance values at various wavelengths. The detailed calibration procedure was published by Bayram [67]. The complete analysis of reaction samples with UV-Vis absorbance results with calibration is presented in Figure 60 -Figure 65.

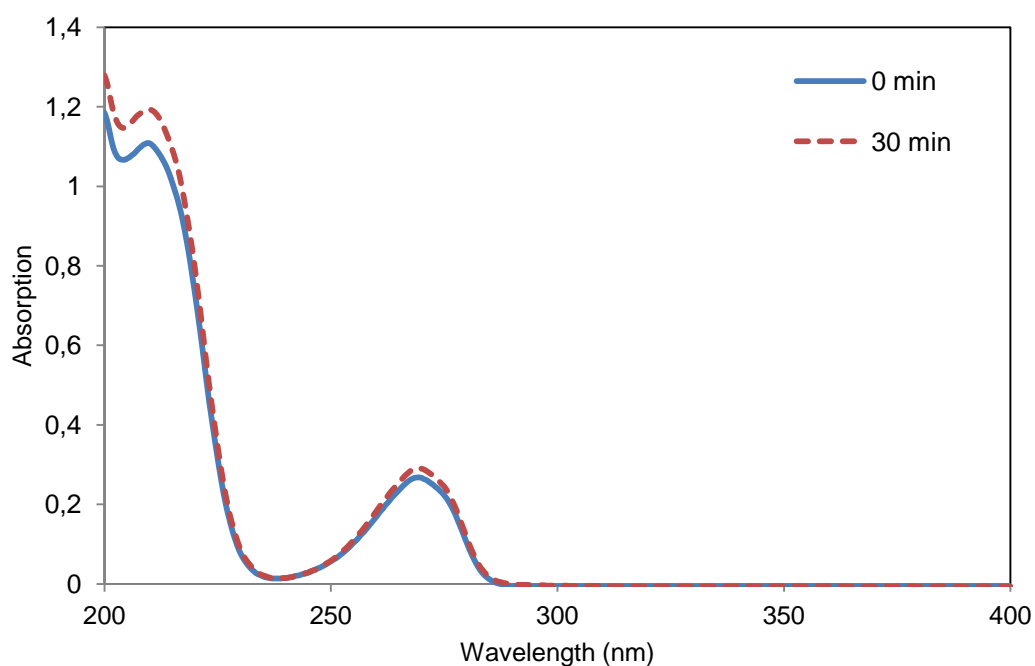


Figure 58: The initial UV-Vis spectrum of phenol and after 30 minutes reaction catalyzed by pure TiO_2 catalyst calcined at 600°C under 300 W/m^2 irradiation.

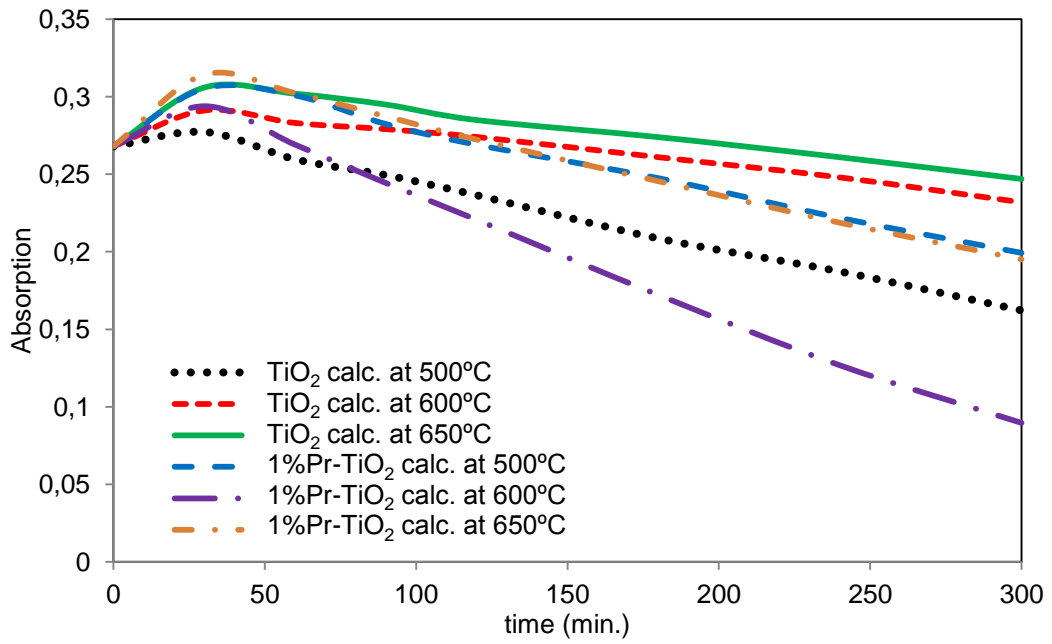


Figure 59: Absorbance at 270nm vs. reaction time for phenol mineralization reaction for 250 ml 20ppm phenol solution with 0.1g catalyst under 300 W/m² irradiation.

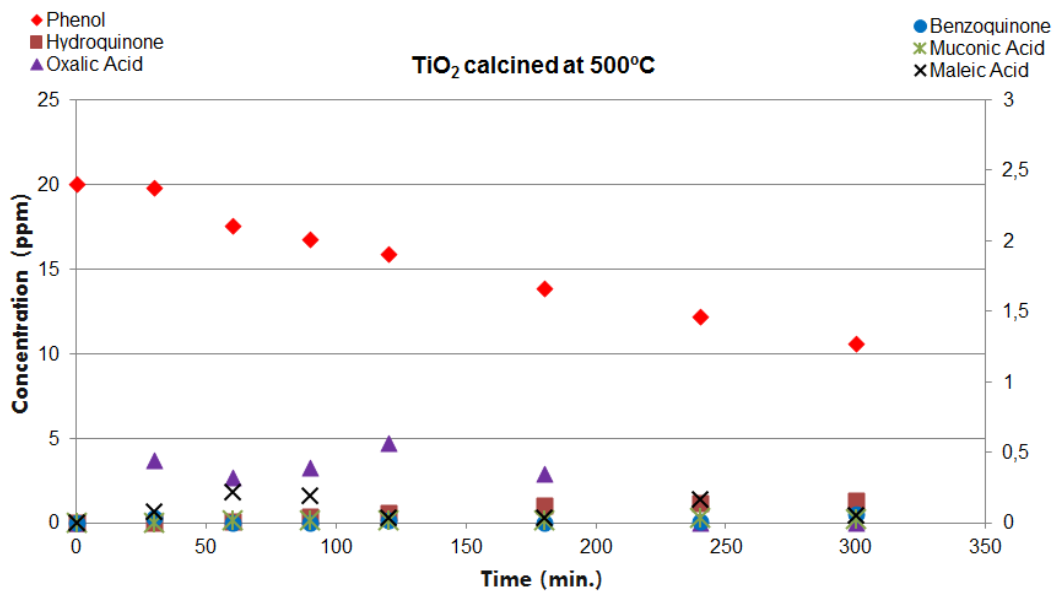


Figure 60: Calculated amounts of species during phenol mineralization reaction for TiO₂ catalyst calcined at 500°C

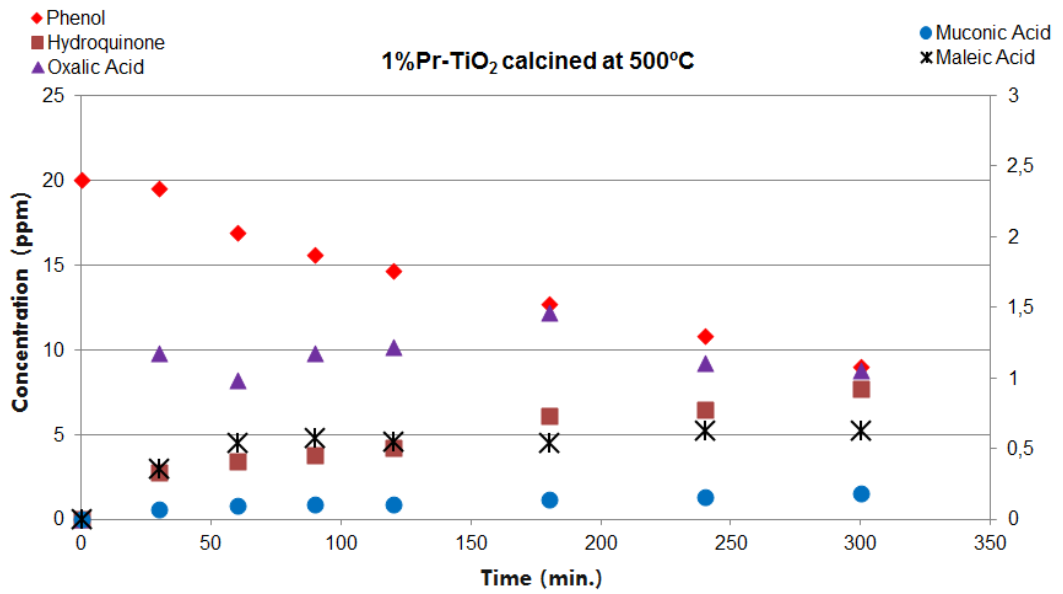


Figure 61: Calculated amounts of species during phenol mineralization reaction for 1%Pr-TiO₂ catalyst calcined at 500°C

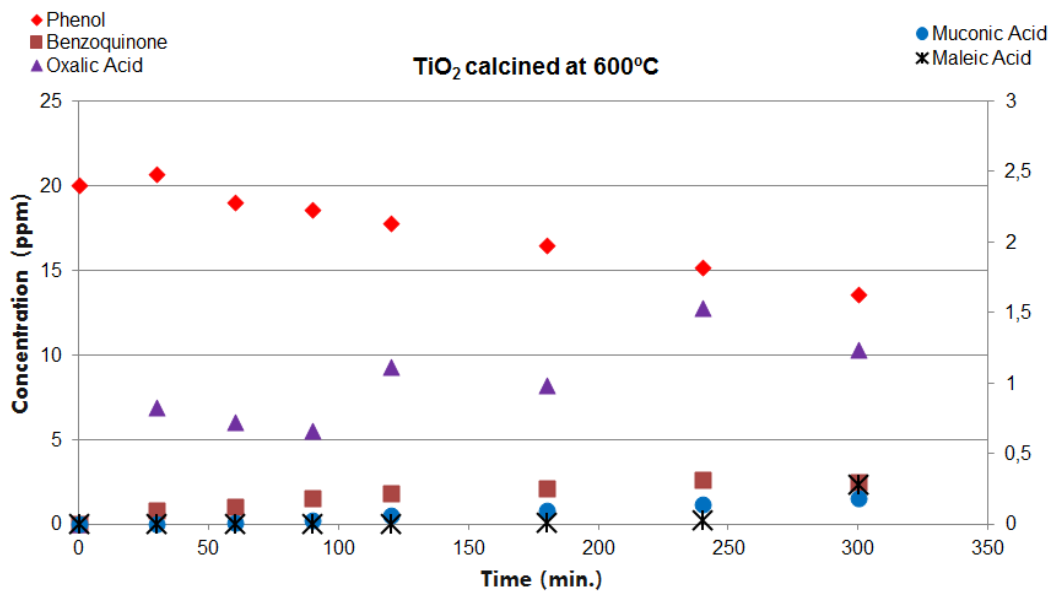


Figure 62: Calculated amounts of species during phenol mineralization reaction for TiO₂ catalyst calcined at 600°C

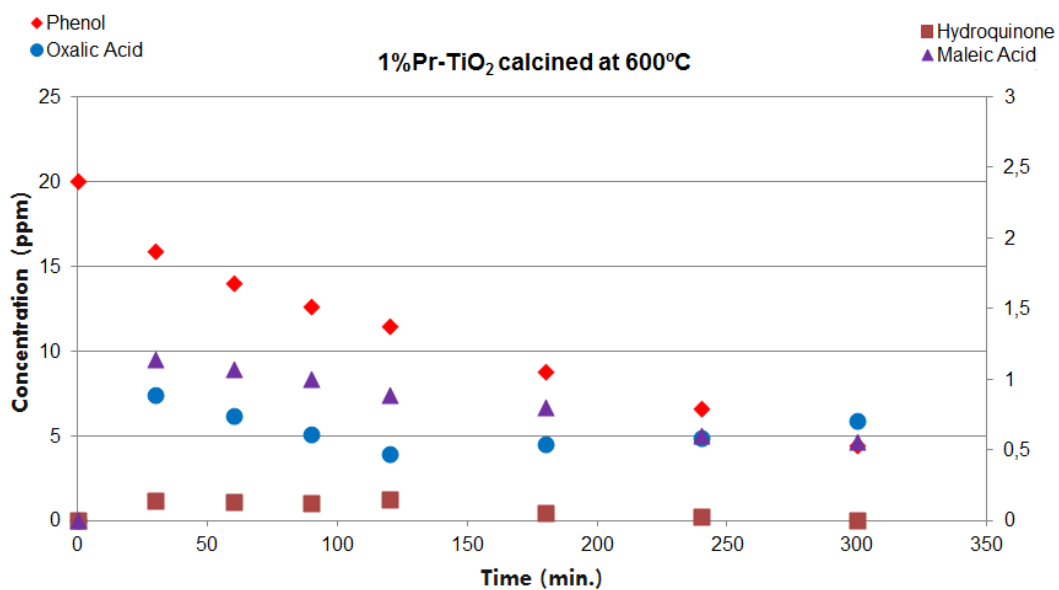


Figure 63: Calculated amounts of species during phenol mineralization reaction for 1%Pr-TiO₂ catalyst calcined at 600°C

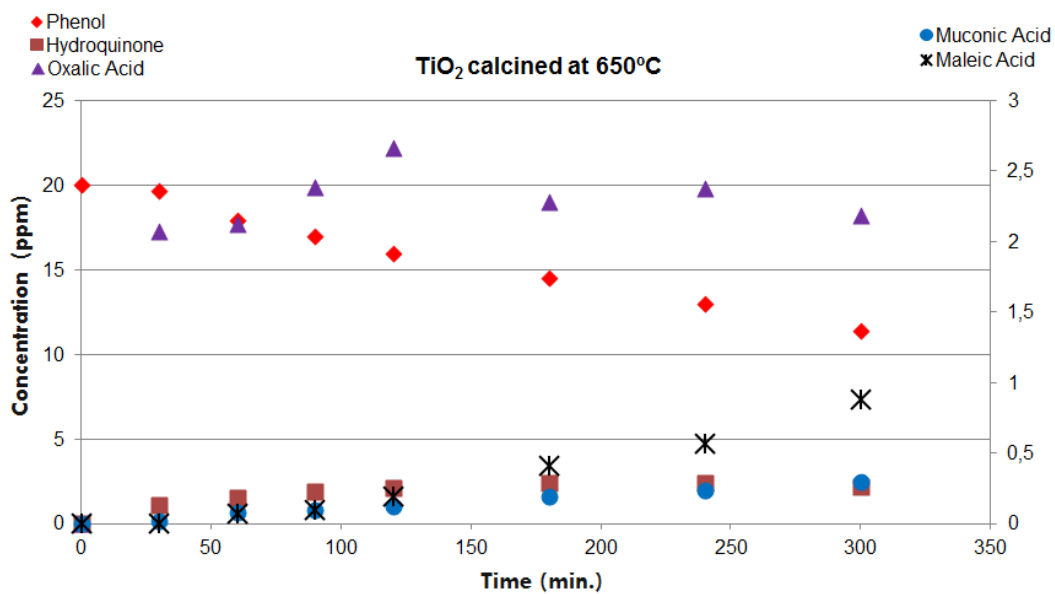


Figure 64: Calculated amounts of species during phenol mineralization reaction for TiO₂ catalyst calcined at 650°C

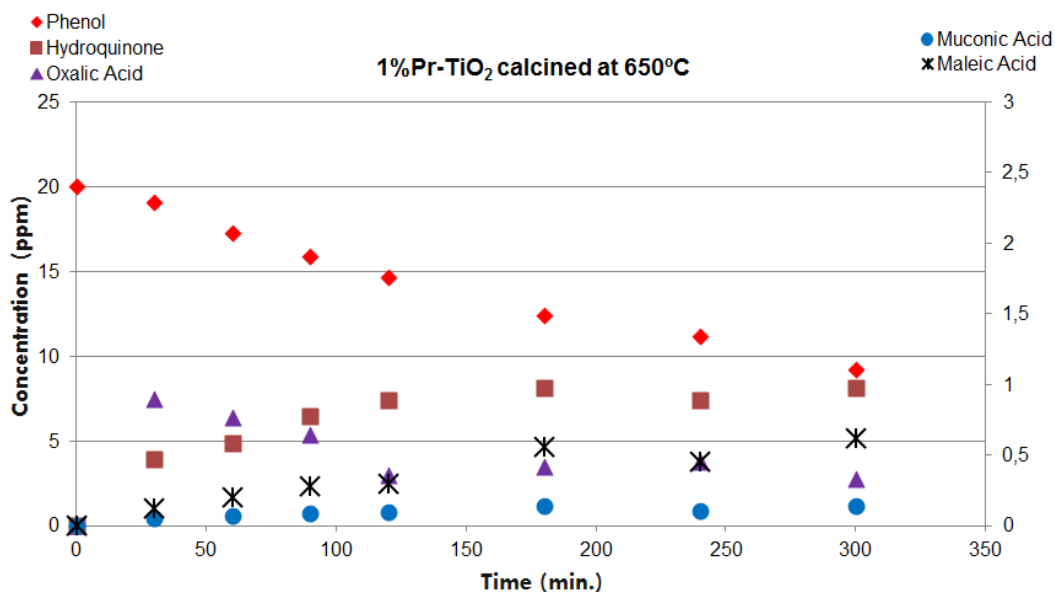


Figure 65: Calculated amounts of species during phenol mineralization reaction for 1%Pr-TiO₂ catalyst calcined at 650°C

From Figure 59, it can be seen that 1%Pr-TiO₂ catalyst calcined at 600°C has the highest photocatalytic activity and among the undoped samples the one calcined at 500°C is the most active one. To be sure about these activity results, the reaction intermediate species are also analyzed. Results obtained according to this model are tabulated in Table 15 - Table 20. The initial concentration of 20 ppm phenol can be lowered down to 10.55 ppm at the end of 300 minutes by using pure TiO₂ catalyst calcined at 500°C which is the most active undoped catalyst. On the other hand, 1%Pr-TiO₂ catalyst calcined at 600°C is the most active one and phenol concentration was lowered to 4.4 ppm at the end of 300 minutes. According to the results obtained, no catechol formation was observed by using the catalysts synthesized. From this result, we can understand that the reaction mechanism follows the hydroquinone route in the mechanism suggested by Bayram as illustrated in Figure 11. As it is seen from Figure 60 -Figure 65, some traces of oxalic acid was detected in reaction solutions which indicate the slowest step on the reaction mechanism is the decomposition of oxalic acid and phenol reacts to form hydroquinone. Also in the reactions with Pr

doped catalysts calcined at 500°C and 650°C some amount of hydroquinone can be observed that hydroquinone to benzoquinone reactions are also slow steps which limits the overall mineralization. On the other hand, in the case of 1%Pr doped TiO₂ calcined at 600°C the reaction rate is very fast and no hydroquinone formation was observed. The reaction mechanism for the complete demineralization of phenol observed in the experiments is given in Figure 66.

For undoped samples, pure TiO₂ calcined at 500°C has a high surface area and composed of 100% pure anatase phase. When the calcination temperature is increased to 600°C, the surface area drops drastically and also rutile starts to form in the crystal structure. Because of this, on photocatalytic demineralization of phenol T500 has higher activity than the other undoped catalysts calcined at higher temperatures. For Pr doped samples 1%Pr-TiO₂ calcined at 500°C has the highest surface area but 1%Pr-TiO₂ calcined at 600°C is the more active one. This result is consistent with the results obtained in the methylene blue degradation test. The surface area of 1%Pr-TiO₂ calcined at 600°C is higher than that of undoped samples and also no rutile formation is observed resulting in a much higher photocatalytic activity. When calcinations temperature is increased to 650°C although still no rutile formation is observed, since the surface area decreases to its half, photocatalytic activity also decreases very much. The effect of Pr doping, suppression of rutile formation and increase in the surface area makes 1%Pr-TiO₂ calcined at 600°C catalyst much more active than the other catalysts.

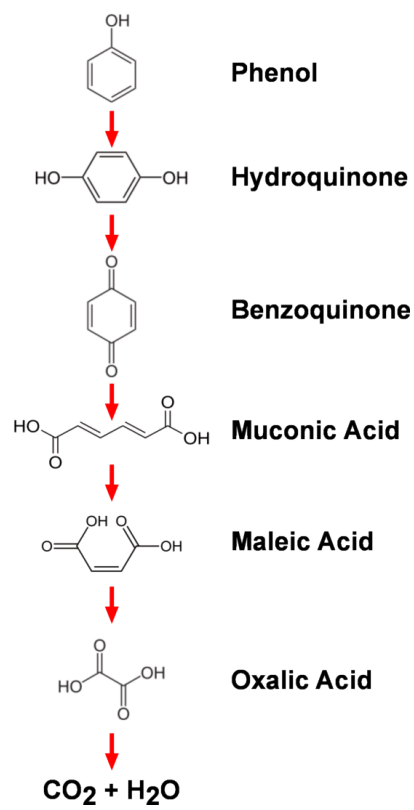


Figure 66: Reaction mechanism for the complete demineralization of phenol observed in the experiments

The rate constants for the first step of the reaction mechanism which is the phenol to hydroquinone reaction have been calculated assuming this is a first order reaction. Assuming depletion of phenol is a first order reaction, concentration of phenol at any time is given as;

$$C_{phenol} = C_{phenol_0} e^{-kt} \quad (24)$$

Where C_{phenol_0} is the initial phenol concentration which is 20ppm, k is the rate constant, and t is the time. The natural logarithm of this equation gives out;

$$-\ln\left(\frac{C_{phenol}}{C_{phenol_0}}\right) = kt \quad (25)$$

According to this equation the graph of $-\ln(C/C_0)$ vs. time for phenol was drawn. The linear trend confirmed the first order reaction rate assumption. The rate constant (k) for the disappearance of phenol is the slope of the line. According to the results obtained it can be seen that the Pr doped catalyst that is calcined at 600°C has the highest rate constant of 0.0049 min^{-1} , that means it is the most active catalyst.

Table 14: Rate constants for the disappearance of phenol

| Catalyst | k (min^{-1}) |
|--------------------------------------|-------------------------|
| TiO ₂ calc. at 500°C | 0.0021 |
| TiO ₂ calc. at 600°C | 0.0012 |
| TiO ₂ calc. at 650°C | 0.0018 |
| 1%Pr-TiO ₂ calc. at 500°C | 0.0026 |
| 1%Pr-TiO ₂ calc. at 600°C | 0.0049 |
| 1%Pr-TiO ₂ calc. at 650°C | 0.0025 |

CHAPTER 5

CONCLUSIONS

The effect of praseodymium doping on the structural properties and photocatalytic activity was studied. The catalyst samples were synthesized by using sol-gel technique in both powder and thin film forms. Thin film samples were prepared by dip coating of glass substrates through the same colloidal solution which the powder form of samples was obtained. Characterization of the catalysts samples were performed by X-ray diffraction, BET, X-ray photoelectron spectroscopy, photoluminescence, photoresponse, scanning electron microscopy and energy dispersive X-ray spectroscopy analysis. Photocatalytic activities of the samples were tested by methylene blue degradation and phenol mineralization tests.

Photocatalytic activity of titania catalysts highly depends on the crystal structure and the surface area of the catalyst. Increase in crystallinity improves the photocatalytic activity. The photocatalytically active crystal phase is anatase which is prone to transform into rutile phase by heat treatment. It was observed that calcination at higher temperatures favors the rutile formation. Catalyst samples prepared by calcination at 600°C and 650°C that are not doped with praseodymium resulted with rutile phase in their structure, whereas 100% anatase crystal structure were observed for Pr doped catalyst samples. Thus, doping TiO₂ with Pr suppresses the rutile formation. Crystallite sizes for Pr doped catalysts which were determined by Scherrer approximation by using XRD data are smaller than the crystal sizes for undoped catalysts. These results show that praseodymium doping inhibits

the crystal growth by sintering and the phase stabilization could be achieved by praseodymium doping. According to the BET results it was seen that doping with praseodymium enhances both the surface area and the total pore volume. It was also observed that higher calcination temperature cause sintering, crystal growth and small surface area while Pr doping suppresses the sintering, crystal growth and higher surface area could be achieved.

Photoluminescence analysis showed that Pr doping can also be used to induce intermediate stable band levels in the band gap of the catalyst. These intermediate levels may be used for photon up-conversion.

From the photoresponse tests it was observed that doping titania nanocrystals with Pr increases the conductivity under the same irradiation power and wavelength. Thus, Pr doping decreases the electron hole recombination reaction rate which is beneficial for photocatalysis. Also band gap energies for the catalysts were calculated and it was observed that Pr doping decreases the band gap of the catalyst giving the catalyst the ability of absorbing a larger range of photons in the solar spectrum.

TEM analysis and elemental mapping by EDX analysis in STEM mode revealed that Pr atoms are homogeneously distributed in the structure. Point analysis made by 2nm beam on several sites over the crystallite particles supported this observation. It was observed that, the catalyst samples are comprised of particles smaller than 20nm. Moreover, some dimensions between the crystal planes were analyzed and compared with the interplanar spacings which fits to anatase structure.

The methylene blue degradation tests showed that Pr doped samples have lower photocatalytic activities than pure TiO_2 counterparts at the first stages of the reaction. This situation is reversed with the time course of the reaction and the complete methylene blue degradation was only achieved on Pr doped samples. The slower initial rate of Pr doped samples than undoped samples were investigated by UV-Vis spectroscopy and it was observed that

the methylene blue surface species are in dimer form, which is converted into monomers by reaction progress. Unlike Pr doped catalysts, complete conversion could not be achieved by TiO₂ catalyst samples.

Phenol mineralization tests by using Pr doped catalyst samples showed higher photocatalytic activities than pure titania samples. The photocatalytic phenol degradation follows a complex kinetics involving many intermediates. The rate limiting steps on phenol degradation were identified as the decomposition of oxalic acid to carbon dioxide and water, and the formation of hydroquinone from phenol. Pr doped TiO₂ samples calcined at 600°C were identified as the most active catalyst sample for phenol degradation which has moderately high surface area, and anatase structure.

As a result, Pr doping improves the photocatalytic activity of titania catalysts. The most important outcome of this study is that Pr doping stabilizes the anatase phase on titanium dioxide catalysts. Pr doping decreases the crystallite size and suppresses the rutile formation.

REFERENCES

- [1] S. Rana, R.S. Srivastava, M.M. Sorensson, R.D.K. Misra, *Mater. Sci. Eng B* 119 (2005) 144.
- [2] J.C. Colmenares, M.A. Aramenis, A. Marinas, J.M. Marinas, F.J. Urbano, *Appl. Catal.* 306 (2006) 120.
- [3] S. Rana, J. Rawat, R.D.K. Misra, *Acta Biomat.* 1 (2005) 691.
- [4] B. O'Regan, M. Gratzel, "A low-cost, high-efficiency solar cell based on dye sensitized colloidal TiO₂ Films", *Nature*, 353, 737, 1991.
- [5] Maen Ni, Micheal K.H. Leung, Dennis Y.C. Leung, K. Sumathy, *Renewable and Sustainable Energy Reviews* 11 (2007) 401
- [6] William D. Callister Jr., "Materials Science and Engineering an Introduction", John Wiley & Sons Inc., 1996.
- [7] C.A. Grimes, O.K. Varghese, S. Ranjan, "Light, Water, Hydrogen The Solar Generation of Hydrogen by Water Photoelectrolysis", Springer, 2009.
- [8] H. de Lasa, B. Serrano, M. Salaices, "Photocatalytic Reaction Engineering", Springer, 2005.
- [9] W. Fu, H. Yang, L. Changa, Hari-Bala, M. Li, G. Zou, *Collo. And Surf. A* 289 (2006) 47.
- [10] Diebold, U., "The surface science of titanium dioxide", *Surface Science Reports*, 48, 53, 2003.

- [11] AB Sherrill, JW Medlin, JG Chen, MA Barteau, "NEXAFS investigations of cyclooctatetraene on TiO_2 (0 0 1) ", Surface Science, 492, 203, 2001.
- [12] VS Lusvardi, MA Barteau, JG Chen, J Eng, B Fruhberger, A Teplyakov. "An NEXAFS investigation of the reduction and reoxidation of $\text{TiO}_2(001)$ ", Surface Science, 397, 237, 1998.
- [13] MA Henderson, WS Epling, CL Perkins, CHF Peden, U Diebold, "Interaction of Molecular Oxygen with the Vacuum-Annealed TiO_2 (110) Surface: Molecular and Dissociative Channels", Journal of Physical Chemistry B, 103, 5328, 1999.
- [14] Henderson M. A., "The interaction of water with solid surfaces: fundamental aspects revisited", Surface Science Reports, 46, 1, 2002.
- [15] AB Sherrill, VS Lusvardi, J Eng, JGG Chen, MA Barteau, "NEXAFS investigation of benzaldehyde reductive coupling to form stilbene on reduced surfaces of TiO_2 (0 0 1)", Catalysis Today, 63, 43, 2000.
- [16] AB Sherrill, MA Barteau, JGG Chen, Abstracts of Papers of The American Chemical Society, 219, U532, 2000.
- [17] Erkan A., Bakir U., Karakas G., "Photocatalytic microbial inactivation over Pd doped SnO_2 and TiO_2 thin films", Journal of Photochemistry and Photobiology A: Chemistry, 184, 313, 2006.
- [18] MA Henderson, "Acetone and Water on TiO_2 (110): H/D Exchange", Langmuir, 21, 3451 - 3458, 2005.
- [19] MA Henderson, "Acetone Chemistry on Oxidized and Reduced TiO_2 (110)", Journal of Physical Chemistry B, 108, 18932, 2004.

- [20] M Calatayud, A Markovits, M Menetrey, B Mguig, C Minot, "Adsorption on perfect and reduced surfaces of metal oxides", *Catalysis Today*, 85, 125, 2003.
- [21] U Diebold, "Structure and properties of TiO₂ surfaces: a brief review", *Applied Physics A-Materials Science and Processing*, 76, 681, 2003.
- [22] MA Henderson, J Szanyi, CHF Peden, "Conversion of N₂O to N₂ on TiO₂ (1 1 0)", *Catalysis Today*, 85, 251, 2003.
- [23] M Bowker, P Stone, R Bennett, N Perkins, "Formic acid adsorption and decomposition on TiO₂ (1 1 0) and on Pd/TiO₂ (1 1 0) model catalysts", *Surface Science*, 511, 435, 2002.
- [24] U Diebold, M Li, O Dulub, ELD Hebenstreit, W. Hebenstreit, "The Relationship between Bulk and Surface Properties of Rutile TiO₂ (110)", *Surface Review and Letters*, 7, 613, 2000.
- [25] M Li, W Hebenstreit, U Diebold, MA Henderson, DR Jennison, "Oxygen-induced restructuring of rutile TiO₂(110) : formation mechanism, atomic models, and influence on surface chemistry", *Faraday Discussions*, 114, 245, 1999.
- [26] VS Lusvardi, KG Pierce, MA Barteau, "Steady-State Catalytic C-C Bond Formation on Reduced TiO₂ Surfaces", *Journal of Vacuum Science and Technology A-Vacuum Surfaces and Films*, 15, 1586, 1997.
- [27] KG Pierce, MA Barteau, "Cyclotrimerization of sterically hindered alkynes in ultrahigh vacuum: TPD of tert-butylacetylene on the reduced TiO₂(001) surface", *Surface Science*, 326, L473, 1995.
- [28] KG Pierce, MA Barteau, "Ketone Coupling on Reduced TiO₂ (001) Surfaces: Evidence of Pinacol Formation", *Journal of Organic Chemistry*, 60, 2405, 1995.

- [29] Y Yamaguchi, H Onishi, Y Iwasawa, "Catalytic Decomposition Reaction of Formic Acid on an Ar⁺-bombarded TiO₂ (110) Surface: Steady-State Kinetics and Microscopic Structure", *Journal of the Chemical Society Faraday Transactions*, 91, 1663, 1995.
- [30] H Idriss, MA Barteau, "Characterization of TiO₂ surfaces active for novel organic syntheses", *Catalysis Letters*, 26, 123, 1994.
- [31] H Idriss, MA Barteau, "Reductive Coupling of Cyclic Ketones on Reduced TiO₂ (001) single and Polycrystalline TiO₂", *Studies In Surface Science and Catalysis*, 78, 463, 1993.
- [32] H Idriss, M Libby, MA Barteau, "Carbon-Carbon bond formation on metal oxides: from single crystal toward catalysis", *Catalysis Letters*, 15, 13, 1992.
- [33] T Sahm, L Madler, A Gurlo, N Barsan, SE Pratsinis, U Weimar, "Flamespray synthesis of tin dioxide nanoparticles for gas sensing", *Sensors and Actuators B-Chemical*, 98, 148, 2004.
- [34] JR McCormick, JR Kitchin, MA Barteau, JG Chen, "A four-point probe correlation of oxygen sensitivity to changes in surface resistivity of TiO₂ (0 0 1) and Pd-modified TiO₂ (0 0 1)", *Surface Science*, 545, L741, 2003.
- [35] S. Semancik, R. E. Cavicchi, "The use of surface and thin film science in the development of advanced gas sensors", *Applied Surface Science* 70-71, 337, 1993.
- [36] Jiri Janata, *Principles of Chemical Sensors*, Plenum Pres, 1989.
- [37] W. Gopel, "Solid-state chemical sensors: Atomistic models and research trends", *Sensors and Actuators* 16, 167, 1989.
- [38] Rober J. Huber, Jiri Janata, editor, *Solid State Chemical Sensors*, Academic Press, 1985.

- [39] P. Cheng, M. Zheng, Y. Jin, Q. Huang, M. Gu, *Mater. Lett.* 57 (2003) 2989.
- [40] Y.V. Kolen'ko, B.R. Churagulov, M. Kunst, L. Mazerolles, C. Colbeau-Justin, "Photocatalytic Properties of Titania Powders Prepared by Hydrothermal Method", *Appl. Catal. B* 54 , 51, 2004.
- [41] G. Wang, "Hydrothermal synthesis and photocatalytic activity of nanocrystalline TiO₂ powders in ethanol–water mixed solutions", *Journal of Molecular Catalysis A: Chemical* 274, 185, 2007.
- [42] Jing I, Li S, Song S, Xue L, Fu H., "Investigation on the electron transfer between anatase and rutile in nano-sized TiO₂ by means of surface photovoltage technique and its effects on the photocatalytic activity.", *Solar Energy Mater. & Solar Cells*, 92, 1030, 2008.
- [43] Francisco M. y Mastelaro V., "Inhibition of the anatase-rutile phase transformation with addition of CeO₂ to CuO-TiO₂ system: Raman spectroscopy, X-ray diffraction, and textural studies.", *Chem Mater*, 14 (6), 2514, 2002.
- [44] J.G. Yu, X.J. Zhao, Q.N. Zhao, "Effect of surface structure on photocatalytic activity of TiO₂ thin films prepared by sol-gel method", *Thin Solid Films* 379, 7, 2000.
- [45] Kyriaki E., Karakitsou and Xenophon E. Verykios, "Effects of Altrivalent Cation Doping of TiO₂ on Its Performance as a Photocatalyst for Water Cleavage", *J . Phys. Chem.*, 97, 1184, 1993.
- [46] Rao, M. V.; Rajeshwar, K.; Pal Verneker, V. R.; DuBow, J., "Photosynthetic Production of H-2 And H₂O₂ On Semiconducting Oxide Grains In Aqueous-Solutions", *J. Phys. Chem.*, 84, 1987, 1980.

- [47] Yu J, Wang G, Cheng B, Zhou M., "Effects of hydrothermal temperature and time on the photocatalytic activity and microstructures of bimodal mesoporous TiO₂ powders.", *Appl Catal B: Environ*, 69, 171, 2007.
- [48] A.L. Linsebigler, G. Lu, J.T. Yates, "Photocatalysis on TiO₂ Surfaces - Principles, Mechanisms, and Selected Results", *Chem. Rev.*, 95, 735, 1995.
- [49] Hidalgo M, Aguilar M, Maicu M, Navio J, Colon G., "Hydrothermal Preparation of Highly Photoactive TiO₂ Nanoparticles.", *Catal Today*, 129 50, 2007.
- [50] Sahni S, Reddy B, Murty B., "Influence Parameters on The Synthesis of Nano-Titania by Sol-Gel Route.", *Mater Sci Eng A*, 452-453, 758, 2007.
- [51] S. Takeda, S. Suzuki, H. Odaka, H. Hosono, "Photocatalytic TiO₂ Thin Film Deposited Onto Glass by DC Magnetron Sputtering", *Thin Solid Films*, 392, 338, 2001.
- [52] A.P. Xagas, E. Androulaki, A. Hiskia, P. Falaras, "Preparation, Fractal Surface Morphology and Photocatalytic Properties of TiO₂ Films", *Thin Solid Films*, 357, 173, 1999.
- [53] G. Martra, "Lewis Acid And Base Sites At The Surface Of Microcrystalline TiO₂ Anatase: Relationships Between Surface Morphology and Chemical Behaviour", *Appl. Catal. A*, 200, 275, 2000.
- [54] Zhao L., Han M., Lian J., "Photocatalytic Activity of TiO₂ Films with Mixed Anatase and Rutile Structures Prepared by Pulsed Laser Deposition", *Thin Solid Films*, 516, 3394, 2008.
- [55] S. Valencia, J. M. Marin, G. Restrepo, "Study of the Bandgap of Synthesized Titanium Dioxide Nanoparticules Using the Sol-Gel Method and a Hydrothermal Treatment", *The Open Materials Science Journal*, 4, 9, 2010.

- [56] Welte A, Waldauf C, Brabec C, Wellmann P., "Application of Optical Absorbance for the Investigation of Electronic and Istructural Properties of Sol-Gel Processed TiO₂ Films.", *Thin Solid Films*, 516, 7256, 2008.
- [57] Reddy K, Manorama S, Redd A., "Bandgap Studies on Anatase Titanium Dioxide Nanoparticles", *Mater Chem Phys*, 78, 239, 2002.
- [58] Oliva F, Avalle L, Santos E, Camara O., "Photoelectrochemical Characterization of Nanocrystalline TiO₂ Films on Titanium Substrates", *J Photochem Photobiol A: Chem*, 146, 175, 2002.
- [59] A. Fujishima, X. Zhang and D. A. Tryk, "TiO₂ photocatalysis and related surface phenomena," *Surface Science Reports*, 63, 515, 2008.
- [60] C.-Yi. Wang, C. Bottcher, D.W. Bahnemann, J.K. Dohrmann, *J. Mater. Chem.* 13 (2003) 2322.
- [61] A. M. Peiró, C. Colombo, G. Doyle, J. Nelson, A. Mills and J. R. Durrant, "Photochemical Reduction of Oxygen Adsorbed to Nanocrystalline TiO₂ Films: A Transient Absorption and Oxygen Scavenging Study of Different TiO₂ Preparations," *Journal of Physical Chemistry B*, 110, 46, 23255, 2006.
- [62] T. Yoshihara, R. Katoh, A. Furube, Y. Tamaki, M. Murai, K. Hara, S. Murata, H. Arakawa and M. Tachiya, "Identification of Reactive Species in Photoexcited Nanocrystalline TiO₂ Films by Wide-Wavelength-Range (400–2500 nm) Transient Absorption Spectroscopy," *Journal of Physical Chemistry B*, 108, 12, 3817, 2004.
- [63] Fujima A., Rao T. N., Tryk D. A., "Titanium dioxide photocatalysis", *Journal of Photochemistry and Photobiology C: Photochemistry Reviews*, 1, 1, 2000.
- [64] M.R. Hoffman, S.T. Martin, W. Choi, D.W. Bahnemann, *Chem. Rev.* 95, 69, 1995

- [65] Murray C. B., Kagan C. R., Bawendi M. G., "Synthesis and Characterization of Monodisperse Nanocrystals and Close Packed Nanocrystal Assemblies", Annual Review of Material Science, 30, 545, 2000.
- [66] A. Yürüm, "The Synthesis of Titanium Dioxide Photocatalysts by Sol-Gel Method: The Effect of Hydrothermal Treatment Conditions and Use of Carbon Nanotube Template", PhD.Thesis, Middle East Technical University, 2009.
- [67] B. Bayram, "Photocatalytic Activity Of Titania – Silica Mixed Oxides Prepared With Co-Hydrolyzation", MS Thesis, Middle East Technical University, 2009
- [68] J. Rawat, S. Rana, R. Srivastava, R.D.K. Misra, Mater. Sci. Eng. C (2006)
- [69] Bamwenda GR, Tsubota S, Nakamura T, Haruta M., J Photochem Photobiol A: Chem 89(2) (1995) 177
- [70] Gurunathan K, Maruthamuthu P, Sastri VC., Int J Hydrogen Energy, 22 (1997) 57
- [71] Lee SG, Lee SW, Lee HI. Appl Catal A: Gen 207 (2001) 173
- [72] Li YX, Lu GX, Li SB. Chemosphere 52 (2003) 843
- [73] Kida T, Guan GQ, Yamada N, Ma T, Kimura K, Yoshida A. Int J Hydrogen Energy 29 (2004) 269
- [74] Wu NL, Lee MS. International Journal of Hydrogen Energy 29 (2004) 1601
- [75] Nada AA, Barakat MH, Hamed HA, Mohamed NR, Veziroglu TN., Int J Hydrogen Energy 30 (2005) 687

- [76] Peng SQ, Li YX, Jiang FY, Lu GX, Li SB., Chem Phys Lett 398 (2004) 235
- [77] Koca A, Sahin M. Int J of Hydrogen Energy 27 (2002) 363
- [78] Bamwenda GR, Arakawa H. Sol Energy Mater Sol Cells 70 (2001) 1
- [79] Abe R, Sayama K, Domen K, Arakawa H., Chem Phys Lett 344 (2001) 339
- [80] Sayama K, Mukasa K, Abe R, Abe Y, Arakawa H., J Photochem Photobiol A: Chem 148 (2002) 71
- [81] Lee K, Nam WS, Han GY. Int J Hydrogen Energy 29 (2004) 1343
- [82] Sayama K, Arakawa H., J Chem Soc, Chem Commun 2 (1992) 150
- [83] Sayama K, Arakawa H., J Photochem Photobiol A: Chem 77 (1994) 243
- [84] Sayama K, Arakawa H., J Photochem Photobiol A: Chem 94 (1996) 67
- [85] Sayama K, Arakawa H, Domen K., Catal Today 28 (1996) 175
- [86] Sayama K, Yase K, Arakawa H, Asakura K, Tanaka A, Domen K, et al., J Photochem Photobiol A: Chem 114 (1998) 125
- [87] Arakawa H, Sayama K., Res Chem Intermed 26 (2000) 145
- [88] Arakawa H, Sayama K., Catal Surv Jpn 4 (2000) 75
- [89] Abe R, Sayama K, Arakawa H., Chem Phys Lett 371 (2003) 360
- [90] John MR, Furgals AJ, Sammells AF. J Phys Chem 87 (1983) 801
- [91] Bamwenda GR, Tsubota S, Nakamura T, Haruta M., J Photochem Photobiol A: Chem 89 (1995) 177

- [92] Sakthivel S, Shankar MV, Palanichamy M, Arabindoo B, Bahnemann DW, Murugesan V., *Water Res* 39 (2004) 3001
- [93] Li FB, Li XZ., *Chemosphere* 48 (2002) 1103
- [94] Kim S, Choi W., *J Phys Chem B* 106 (2002) 13311
- [95] Jin S, Shiraishi F., *Chem Eng J* 97 (2004) 203
- [96] Subramanian V, Wolf EE, Kamat P., *J Am Chem Soc* 126 (2004) 4943
- [97] Subramanian V, Wolf E, Kamat P. *J Phys Chem B* 105 (2001) 11439
- [98] Subramanian V, Wolf E, Kamat P. *J Phys Chem B* 107 (2003) 7479
- [99] Jakob M, Levanon H, Kamat PV. *Nano Lett* 3 (2003) 353
- [100] Tseng IH, Chang WC, Wu JCS. *Appl Catal B: Environ* 37 (2002) 37
- [101] Tseng IH, Wu JCS, Chou HY. *J Catal* 221 (2004) 432
- [102] Poroshkov VP, Gurin VS. *Surf Sci* 331 (1995) 1520
- [103] Liu SX, Qu ZP, Han XW, Sun CL. *Catal Today* 93 (2004) 877
- [104] Kamat PV, Meisel D. *Curr Opin Colloid Interface Sci* 7 (2002) 282
- [105] Kamat PV, Flumiani M, Dawson A. *Colloids Surf A: Physiochem Eng Aspects* 202 (2002) 269
- [106] Bardos ES, Czili H, Horvath A. *J Photochem Photobiol A: Chem* 154 (2003) 195
- [107] J. Araña, J.M. Doña-Rodríguez, O. Gonzalez-Diaz, E. Tello Rendon, J.A. Herrera Melian, G. Colo'n, J.A. Navio, J. Pérez Peña, *J. Mol. Catal. A* 215 (2004) 153.

- [108] N.Serpone, D.Lawless, J.Disdier, J.M.Herrmann, Langmuir 10 (1994) 643.
- [109] C.G. Wu, C.C. Chao, F.T. Kuo, Catal. Today 97 (2004) 103.
- [110] P. Pichat, J.M. Herrmann, J. Disdier, M.N. Mozzanega, H. Courbon, Stud. Surf. Sci. Catal. 19 (1984) 319.
- [111] A.W. Xu, Y. Gao, H.-Q. Liu, J. Catal. 207 (2002) 151.
- [112] K.S. Rane, R. Mhalsiker, S. Yin, T. Sato, Kuk Cho, E. Dunbar, P. Biswas, J. Solid State Chem. 179 (2006) 3033.
- [113] Choi WY, Termin A, Hoffmann MR. J Phys Chem 84 (1994) 13669
- [114] Litter MI. Appl Catal B: Environ 23 (1999) 89
- [115] Dvoranova D, Brezova V, Mazur M, Malati M. Appl Catal B: Environ 37 (2002) 91
- [116] Hameed A, Gondal MA, Yamani ZH. Catal Commun 5 (2004) 715
- [117] Xu AW, Gao Y, Liu HQ. J Catal 207 (2002) 151
- [118] Paola AD, Marci G, Palmisano L, Schiavello M, Uosaki K, Ikeda S, et al. J Phys Chem B 206 (2002) 637
- [119] Yuan WH, Bi HQ, Wei CH. China Univ Technol (Nature Science Edition) 32 (2004) 29
- [120] Wilke K, Breuer HD. J Photochem Photobiol A: Chem 121 (1999) 49
- [121] Wang RH, Xin JHZ, Yang Y, Liu HF, Xu LM, Hu JH. Appl Surf Sci 227 (2004) 312
- [122] Xu JC, Shi YL, Huang JE, Wang B, Li HL. J Mol Catal A: Chem 219 (2004) 351

- [123] Ohta T. *Int J Hydrogen Energy* 25 (2000) 911
- [124] Ohta T. *Int J Hydrogen Energy* 25 (2000) 1151
- [125] Hitoki G, Takata T, Ikeda S, Hara M, Kondo JN, Kakihana M, et al. *Catal Today* 63 (2000) 175
- [126] Domen K, Ikeda S, Takata T, Tanaka A, Hara M, Kondo JN. *Appl Energy* 67 (2000) 159
- [127] Ohta T. *Appl Energy* 67 (2000) 3
- [128] Hara M, Kondo T, Komoda M, Ikeda S, Shinohara K, Tanaka A, et al. *Chem Commun* 3 (1998) 357
- [129] Ikeda S, Takata T, Kondo T, Hitoki G, Hara M, Kondo JN, et al. *Chem Commun* 20 (1998) 2185
- [130] Hara M, Komoda M, Hasei H, Yashima M, Ikeda S, Takata T, et al. *J Phys Chem B* 104 (2000) 780
- [131] Hara M, Hasei H, Yashima M, Ikeda S, Takata T, Kondo JN, et al. *Appl Catal A: Gen* 190 (2000)35
- [132] Ohta T. *Int J Hydrogen Energy* 25 (2000) 287
- [133] Takata T, Ikeda S, Tanaka A, Hara M, Kondo JN, Domen K. *Appl Catal A: Gen* 200 (2000) 255
- [134] Ohta T. *Appl Energy* 67 (2000) 181
- [135] Umabayashi T, Yamaki T, Itoh H, Asai K. *Appl Phys Lett* 81 (2002) 454
- [136] Ohno T, Akiyoshi M, Umabayashi T, Asai K, Mitsui T, Matsumura M. *Appl Catal A: Gen* 265 (2004) 115

- [137] Khan SUM, Al-Shahry Jr. M, BI W. *Science* 297 (2002) 2243
- [138] Okada M, Yamada Y, Jin P, Tazawa M, Yoshimura K. *Thin Solid Films* 442 (2003) 217
- [139] Hattori A, Yamamoto M, Tada H, Ito S. *Chem Lett* (1998) 707
- [140] Kobayakawa K, Murakami K, Sato Y. *Int J Photochem Photobiol A: Chem* 170 (2004) 177
- [141] Chen SZ, Zhang PY, Zhuang DM, Zhu WP. *Catal Commun* 5 (2004) 677
- [142] Torres GR, Lindgren T, Lu J, Granqvist CG, Lindquist SE. *J Phys Chem B* 108 (2004) 5995
- [143] Lindgren T, Mwabora JM, Avendano E, Jonsson J, Hoel A, Granqvist CG, et al. *J Phys Chem B* 107 (2003) 5709
- [144] Chen XB, Burda C. *J Phys Chem B* 108 (2004) 15446
- [145] Gole JL, Stout JD, Burda C, Lou YB, Chen XB. *J Phys Chem B* 108 (2004) 1230
- [146] Mrowetz M, Balcerski W, Colussi AJ, Hoffmann MR. *J Phys Chem B* 108 (2004) 17269
- [147] Yang Kuisheng, Xue Huili et. al. *J Rare Earths* 24 (2006) 175
- [148] Shalav A., Richards B.S., Green M.A. *Sol Energy Mater Sol Cells* 91 (2007) 829
- [149] Stümpel C, McCann M, et. al. *Sol Energy Mater Sol Cells* 91 (2007) 238
- [150] Richards B.S. *Sol Energy Mater Sol Cells* 90 (2006) 2329

- [151] Wang Weizhong, Qu Wanchun et. al. J Rare Earths 24 (2006) 187
- [152] Chao Liu, Jong Heo J Non-crystalline Solids 352 (2006) 5325
- [153] Huber G, Heumann E, Sandrock T, Petermann K J Luminescence 72 (1997) 1
- [154] Simpson D.A., Baxter G.W. et. al. J Non-crystalline Solids 352 (2006) 136
- [155] Kürk S, Dienning A, Heumann E et. al. J Alloys & Compounds 300 (2000) 65
- [156] Gejihu De, Weiping Qin, Jishen Zhang et. al. J Luminescence 122 (2007) 128
- [157] Liqiong An, Jian Zhang, Min Liu, Shiwei Wang J Luminescence 122 (2007) 125
- [158] Sun C.L., Li J.F., Hu C.H., Jiang H.M., Jiang Z.K. The European Phys J D 39 (2006) 303
- [159] Wenxiu Que, Buddhudu S., et. al. Mater Sci & Eng C 16 (2001) 153
- [160] Wenyue Su, Xianzhi Fu, et. al. Applied Catal. B: Environmental 77 (2008) 264
- [161] A. Amlouk et. al. Mater Sci & Eng B 146 (2008) 74
- [162] Juan Yang, Jun Dai, Jiantong Li, Appl Surf Sci 257 (2011) 8965
- [163] K.T. Ranjit, I. Willner, S.H. Bossmann, A.M. Braun, Environ Sci Technol 35 (2001) 1544
- [164] Chatterjee D., Dasgupta S., Journal of Photochemistry and Photobiology C: Photochemistry Review, 6, 186, 2005.

- [165] Shchukin D. G., Sviridov D. V., "Photocatalytic processes in spatially confined micro- and nanoreactors", *Journal of Photochemistry and Photobiology C: Photochemistry Review*, 7, 23, 2006.
- [166] Shephard G. S., Stockenstrom S., de Villiers D., Engelbrecht W. J., Sydenham E. W., Wessels G. F. S., "Degradation of microcystin toxins in a falling film photocatalytic reactor with immobilized titanium dioxide catalyst", *Water Research*, 36, 140, 2002.
- [167] Sonawane R. S., Hegde S. G., Dongare M. K., "Preparation of titanium(IV) oxide thin film photocatalyst by sol-gel dip coating", *Materials Chemistry and Physics*, 77, 744, 2002.
- [168] Sunada K., Watanabe T., Hashimoto K., "Studies on photokilling of bacteria on TiO₂ thin film", *Journal of Photochemistry and Photobiology A: Chemistry*, 156, 227, 2003.
- [169] Shioya Y., Ikeue K., Ogawa M., Anpo M., "Synthesis of transparent Ti-containing mesoporous silica thin film materials and their unique photocatalytic activity for the reduction of CO₂ with H₂O", *Applied Catalysis A: General*, 254, 251, 2003.
- [170] Arana J., Rendon E.T, Rodriguez J. M. D., "High concentrated phenol and 1,2-propylene glycol water solutions treatment by photocatalysis: Catalyst recovery and re-use", *Applied Catalysis B: Environmental*, 30, 1, 2001.
- [171] Scotti R., D'Arienzo M., Testino A., Morazzoni F., "Photocatalytic mineralization of phenol catalyzed by pure and mixed phase hydrothermal titanium dioxide", *Applied Catalysis B: Environmental*, 2008.
- [172] Tasai S., Cheng S., "Effect of TiO₂ crystalline structure in photocatalytic degradation of phenolic contaminants", *Catalysis Today*, 33, 227, 1997.

- [173] Para S., Olivero J., Pacheco L., Pulgarin C., "Structural properties and photoreactivity relationships of substituted phenols in TiO₂ suspensions", *Applied Catalysis B: Environment*, 43, 293, 2003.
- [174] Aaron Ortiz-Gomez, Benito Serrano-Rosales, Hugo de Lasa, "Enhanced mineralization of phenol and other hydroxylated compounds in a photocatalytic process assisted with ferric ions", *Chemical Engineering Science*, 63, 2, 520, 2008.
- [175] Aaron Ortiz-Gomez, Benito Serrano-Rosales, Miguel Salaices, Hugo de Lasa, "Photocatalytic Oxidation of Phenol: Reaction Network, Kinetic Modeling, and Parameter Estimation", *Ind. Eng. Chem. Res.*, 46, 23, 7394, 2007.
- [176] Mills A., Wang J., "Photobleaching of methylene blue sensitised by TiO₂: an ambiguous system?", *Journal of Photochemistry and Photobiology A: Chemistry*, 127, 123, 1999.
- [177] Zhu J, Yang J, Bian Z, et al., "Nanocrystalline Anatase TiO₂ Photocatalysis Prepared via a Facile Low Temperature Nonhydrolytic Sol-Gel Reaction of TiCl₄ and Benzyl Alcohol.", *Appl Catal B: Environ*, 76, 82, 2007.
- [178] L. Znaidi, R. Séraphimova, J.F. Bocquet, C. Colbeau-Justin, C. Pommier, "A Semi-Continuous Process For The Synthesis Of Nanosize TiO₂ Powders And Their Use As Photocatalysts", *Mater. Res. Bull.*, 36, 811, 2001.
- [179] B Roig, C Gonzalez, O Thomas, "Monitoring Of Phenol Photodegradation By Ultraviolet Spectroscopy", *Spectrochimica Acta Part A: Molecular and Biomolecular Spectroscopy*, 59, 303, 2003.
- [180] A. Santos, P. Yustos, A. Quintanilla, S. Rodríguez, F. García-Ochoa, "Route Of The Catalytic Oxidation Of Phenol In Aqueous Phase", *Applied Catalysis B: Environmental*, 39, 97, 2002.

- [181] Li Y., Li X., Li J., Yin J., "Photocatalytic degradation of methyl orange by TiO₂-coated activated carbon and kinetic study", *Water Research*, 40, 1119, 2006.
- [182] Neppolian B., Choi H. C., Sakthivel S., "Solar/UV-induced photocatalytic degradation of three commercial textile dyes", *Journal of Hazardous Material B*, 89, 303, 2002.
- [183] Auguliaro V., Baiocchi C., Prevot A. B., "Azo-dyes photocatalytic degradation in aqueous suspension of TiO₂ under solar irradiation", *Chemosphere*, 49, 1223, 2002.
- [184] Lachheb H., Puzenat E., Houas A., Ksibi M., Elaloui E., Guillard C., Herrmann J.-M., "Photocatalytic degradation of various types of dyes (Alizarin S, Crocein Orange G, Methyl Red, Congo Red, Methylene Blue) in water by UV-irradiated titania", *Applied Catalysis B: Environmental* 39, 75, 2002.
- [185] J.H. Schattka, D.G. Shchukin, J. Jia, M. Antonietti, R.A. Caruso, "Photocatalytic Activities of Porous Titania and Titania/Zirconia Structures Formed by Using a Polymer Gel Templating", *Chem. Mater.*, 14, 5103, 2002.
- [186] S. Jockusch, N. J. Turro, "Aggregation of Methylene Blue Adsorbed on Starburst Dendrimers", *Macromolecules*, 28, 7416-7418, 1995.
- [187] K. Murugan, T. N. Rao, A. S. Gandhi, B.S. Murty, "Effect of aggregation of methylene blue dye on TiO₂ surface in self-cleaning studies", *Catalysis Communications*, 11, 518–521, 2010.
- [188] Vohra M. S., Davis A. P., "TiO₂-Assisted photocatalysis of lead-EDTA", *Water Research*, 34, 952, 2000.
- [189] Zhang R., Gao L., "Photodegradation of surfactants on the nanosized TiO₂ prepared by hydrolysis of the alkoxide titanium", *Chemosphere*, 54, 405, 2004.

- [190] Kataoka S., Lee E., Tejedor M. I., Anderson M. A., "Photocatalytic degradation of hydrogen sulfide and in situ FT-IR analysis of reaction products on surface of TiO₂", *Applied Catalysis B: Environmental*, 61, 159, 2005.
- [191] A. Fujishima and K. Honda, "Electrochemical Photolysis of Water at a Semiconductor Electrode," *Nature*, 37, 1972.
- [192] A. J. Bard and M. A. Fox, "Artificial Photosynthesis: Solar Splitting of Water to Hydrogen and Oxygen," *Accounts of Chemical Research*, 28, 141, 1995.
- [193] K. Hirano, E. Suzuki, A. Ishikawa, T. Moroi, H. Shiroishi and M. Kaneko, "Sensitization of TiO₂ particles by dyes to achieve H₂ evolution by visible light," *Journal of Photochemistry and Photobiology A: Chemistry*, 136, 157, 2000.
- [194] M. Kitano, K. Tsujimaru and M. Anpo, "Decomposition of water in to separate evolution of hydrogen and oxygen using visible light-responsive TiO₂ thin film photocatalysts: Effect of work function of the substrates on the yield of the reaction," *Applied Catalysis A: General*, 314, 179, 2006.
- [195] J. H. Park, S. Kim and A. J. Bard, "Novel Carbon-Doped TiO₂ Nanotube Arrays with Aspect Ratios for Efficient Solar Water Splitting," *Nano Letters*, 6, 1, 24-28, 2006.
- [196] J. Nowotny, T. Bak, M. Nowotny and L. Sheppard, "Titanium dioxide for solar-hydrogen I. Functional properties," *International Journal of Hydrogen Energy*, 32, 2609, 2007.
- [197] R. Dholam, N. Patel and A. Miotello, "Physically and chemically synthesized TiO₂ composite thin films for hydrogen production by photocatalytic water splitting," *International Journal of Hydrogen Energy*, 33, 6896, 2008.

- [198] R. Navarro, M. Sanchez-Sanchez, M. Alvarez-Galvan, F. del Valle and J. Fierro, "Hydrogen production from renewable sources: biomass and photocatalytic opportunities," *Energy and Environmental Science*, 2, 35, 2008.
- [199] Wang R., Hashimoto K., Fujishima A., Chikuni, M., Kojima E., Kitamura A., Shimohigoshi M., Watanabe T., "Light-induced amphiphilic surfaces", *Nature*, 388, 431, 1997.
- [200] Wang R., Hashimoto K., Fujishima A., Chikuni, M., Kojima E., Kitamura A., Shimohigoshi M., Watanabe T., "Photogeneration of Highly Amphiphilic TiO₂ Surfaces", *Advanced Materials*, 10, 135, 1998.
- [201] Bems B., Jentoft F. C., Schlögl R., "Photoinduced decomposition of nitrate in drinking water in the presence of titania and humic acids", *Applied Catalysis B: Environmental*, 20, 155, 1999.
- [202] Furuzono T., Iwasaki M., Yasuda S., Korematsu A., Yoshioka T., Ito S., "Photoreactivity and cell adhesiveness of amino-group-modified titanium dioxide nano-particles on silicone substrate coated by covalent linkage", *Journal of Materials Science Letters*, 22, 1737, 2003.
- [203] Stevenson M., Bullock K., Lin W. Y., Rajeshwar K., "Sonolytic enhancement of the bactericidal activity of irradiated titanium dioxide suspensions in water", *Research on Chemical Intermediates*, 23, 311, 1997.
- [204] Su C, Tseng C, Chen L, You B, Hsu B, Chen S., "Sol Hydrothermal and Photocatalysis of Titanium Dioxide.", *Thin Solid Films*, 498, 256, 2006.
- [205] Brinker C. J., Scherer G. W., "Sol-Gel Science: The Physics and Chemistry of Sol-Gel Processing", Academic Press, 1990.
- [206] C. Su, B.-Y. Hong, C.-M. Tseng, *Catal Today* 96 (2004) 119

- [207] M. Wu, G. Lin, D. Chen, G. Wang, D. He, S. Feng, R. Xu, *Chem Mater* 14 (2002) 1974
- [208] Zhang Y. X., Li G. H., Zhang, “Hydrothermal synthesis and photoluminescence of TiO₂ nanowires”, *Chemical Physics Letters*, 365, 300, 2002.
- [209] Nakaso K., Fujimoto T., Seto T. Shimada M., Okuyama K., Lunden M.M., “Size distribution change of titania nano-particle agglomerates generated by gas phase reaction, agglomeration and sintering”, *Aerosol Science and Technology*, 35, 929, 2001.
- [210] Nakaso K., Okuyama K., Shimada M., Pratsinis S.E., “Effect of reaction temperature on CVD-made TiO₂ primary particle diameter”, *Chemical Engineering Science*, 58, 3327, 2003.
- [211] Kim C. S., Okuyama K., Nakaso K., Shimada M., “Direct measurement of nucleation and growth modes in titania nanoparticles generation by a CVD method”, *Journal of Chemical Engineering of Japan*, 37, 1379, 2004.
- [212] Adachi M., Okuyama K., Fujimoto T., “Film Formation by a New Chemical Vapor Deposition Process Using Ionization of Tetraethylorthosilicate”, *Japanese Journal of Applied Physics*, 34, 1148, 1995.
- [213] Van de Krol R., Goossens A., Schoonman J., “Mott-Schottky analysis of nanometer-scale thin-film anatase TiO₂”, *Journal of Electrochemical Society*, 144, 1723, 1997.
- [214] Swihart M. T., “Vapor-phase synthesis of nanoparticles”, *Current Opinion in Colloid and Interface Science*, 8, 127, 2003.
- [215] S. Lee, J. Drwiega, D. Mazyck, C.-Y. Wu, W.M. Sigmund, *Mater. Chem. Phys.* 96 (2006) 483.

- [216] O. Carp, C.L. Huisman, A. Reller, Prog. Solid State Chem. 32 (2004) 33.
- [217] B.D. Cullity, "Elements of X-ray diffraction", Addison-Wesley Publ. Comp. Inc., 1967.
- [218] Jing Wu, Qingju Liu, Pan Gao, Zhongqi Zhu, "Influence of praseodymium and nitrogen co-doping on the photocatalytic activity of TiO₂", Materials Research Bulletin 46, 1997, 2011.
- [219] Wen B, Liu C, Liu Y., "Optimization of the Preparation Methods Synthesis of Meso Structures TiO₂ with High Photocatalytic Activities.", J Photochem Photobiol A: Chem, 173, 7, 2005.
- [220] P. Babelon, A.S. Dequiedt, H. Mostéfa-Sba, S. Bourgeois, P. Sibillot, M. Sacilotti, "SEM and XPS studies of titanium dioxide thin films grown by MOCVD", Thin Solid Films 322, 63, 1998.
- [221] U. Diebold, "TiO₂ by XPS", Surface Science Spectra, 4, 3, 227, 1997.
- [222] M. Sawangphruk, J. S. Foord, "Localized electrodeposition of praseodymium oxide on boron-doped diamond", Diamond & Related Materials 19, 885, 2010.
- [223] A. Fissel, J. Dabrowski, H. J. Osten, "Photoemission and ab initio theoretical study of interface and film formation during epitaxial growth and annealing of praseodymium oxide on Si(001)", Journal of Applied Physics, 91, 11, 8986, 2002.
- [224] S. Lütkehoff, M. Neumann, A. Slebarski, "3d and 4d x-ray-photoelectron spectra of Pr under gradual oxidation", PHYSICAL REVIEW B, 52, 19, 808, 1995.

- [225] H. Ogasawara, A. Kotani, R. Potze, G. A. Sawatzky, B. T. Thole, "Praseodymium 3d- and 4d-core photoemission spectra of Pr_2O_3 ", *PHYSICAL REVIEW B*, 44, 11, 5465, 1991.
- [226] G.-M. Rignanese, A. Pasquarello, J. C. Charlier, X. Gonze, R. Carr, "Nitrogen Incorporation at Si(001)- SiO_2 Interfaces: Relation between N 1s Core-Level Shifts and Microscopic Structure", *PHYSICAL REVIEW LETTERS*, 79, 25, 5174, 1997.
- [227] D.D. Sarma, C.N.R. Rao, "XPES studies of oxides of second- and third-row transition metals including rare earths", *Journal of Electron Spectroscopy and Related Phenomena*, 20, 1, 25, 1980.
- [228] M.K. Dalai, R. Kundu, P. Pal, M. Bhanja, B.R. Sekhar, C. Martin, "XPS study of $\text{Pr}_{1-x}\text{Ca}_x\text{MnO}_3$ ($x = 0.2, 0.33, 0.4$ and 0.84)", *Journal of Alloys and Compounds*, 509, 7674, 2011.
- [229] Hossain F, Sheppard L, Nowotny J, Murch G., "Optical Properties of Anatase and Rutile Titanium Dioxide: Ab Initio Calculations For Pure And Anion-Doped Material.", *J Phys Chem Solids*, 69, 1820, 2008.
- [230] M. Liu, L. Piao, L. Zhao, S. Ju, Z. Yan, T. He, C. Zhoua, W. Wang, "Anatase TiO_2 Single Crystals with Exposed {001} and {110} Facets: Facile Synthesis and Enhanced Photocatalysis", *Chem. Commun.*, 46, 1664, 2010.
- [231] J. Zhang, Y. Zhang, Y. Leia, C. Pan, "Photocatalytic and Degradation Mechanisms of Anatase TiO_2 : a HRTEM Study", *Catal. Sci. Technol.*, 1, 273, 2011.
- [232] S. Watson, D. Beydoun, R. Amal, *J. Photochem. and Photobio. A:Chem.* 148 (2002) 303
- [233] D. Beydoun, R. Amal, *Mater. Sci. Eng. B* 94 (2002) 71.

- [234] D. Beydoun, R. Amal, G. Low, S. McEvoy, *J. Mol. Catal. A* 180 (2002) 193.
- [235] Y.S. Chung, S.B. Park, K. Duk-Won, *Mater. Chem. Phys.* 86 (2004) 375.
- [236] M. Ma, Y. Zhang, X. Li, D. Fu, H. Zhang, N. Gu, *Collo. And Surf. A* 224 (2003) 207.
- [237] T. Matsunaga, R. Tomoda, T. Nakajima, H. Wake, *FEMS Microbiol. Lett.* 29 (1985) 211.
- [238] D. Beydoun, R. Amal, G.K.-C. Low, S. McEvoy, *J. Phys. Chem.* (2000) 104
- [240] C.N. Rao, J. Gopalakrishnan, "New directions in the solid state Chemistry", 2nd edition, Cambridge University Press, Cambridge, 1997
- [241] A.D. McQuillan, M.K. McQuillan, "'Titanium" Metallurgy of Rarer Metals", Butterworths Sci. Publ., London, 1956
- [242] A. Wold, K. Dwight, "Solid State Chemistry", Chapman & Hall Inc., 1993
- [243] A.F. Wells "Structural Inorganic Chemistry", 5th edition, Oxford Science Publ., Oxford, 1984
- [244] R.J.H. Clark, "The Chemistry of Titanium and Vanadium", Elsevier Publ. Co., Newyork, 1968
- [245] M.I. Badawy, H.Y. Ghaly, M.E.M. Ali, *Desalination* 267 (2011) 250

APPENDIX A

CALIBRATION STUDY OF UV_VIS SPECTROPHOTOMETER

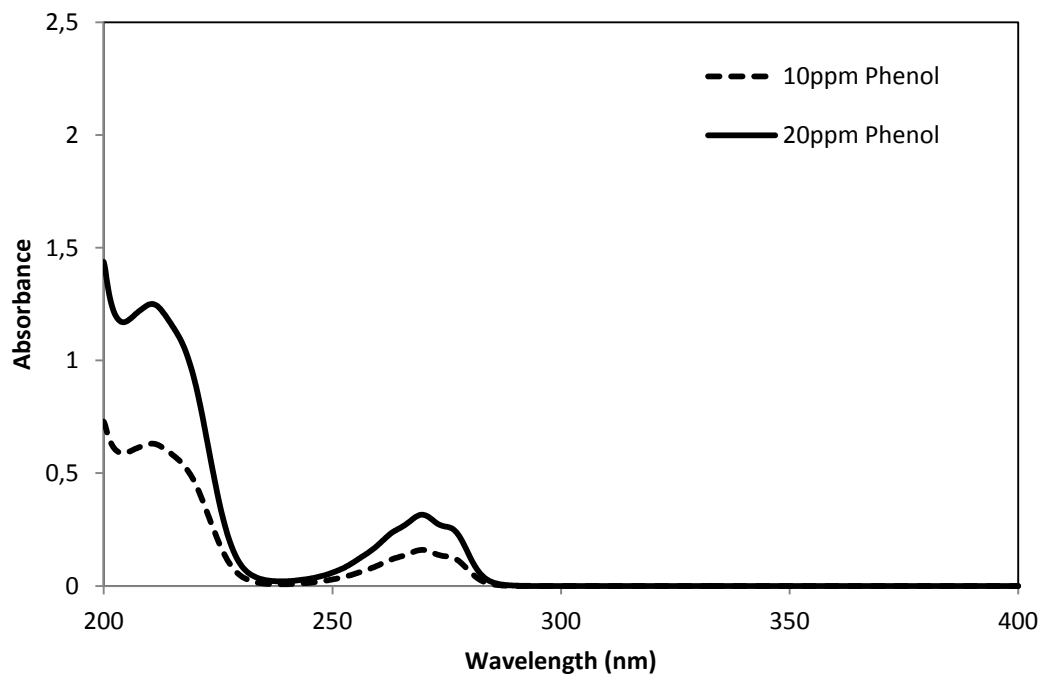


Figure 67: 10, 20ppm aqueous phenol solutions' UV-Vis spectrum

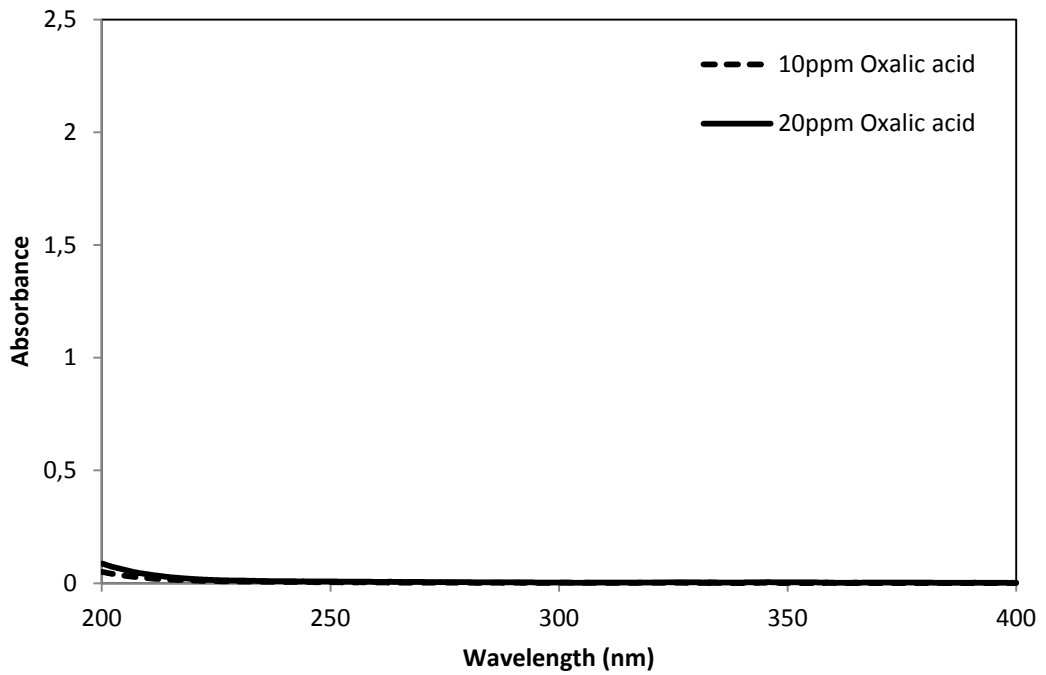


Figure 68: 10, 20ppm aqueous oxalic acid solutions' UV-Vis spectrum

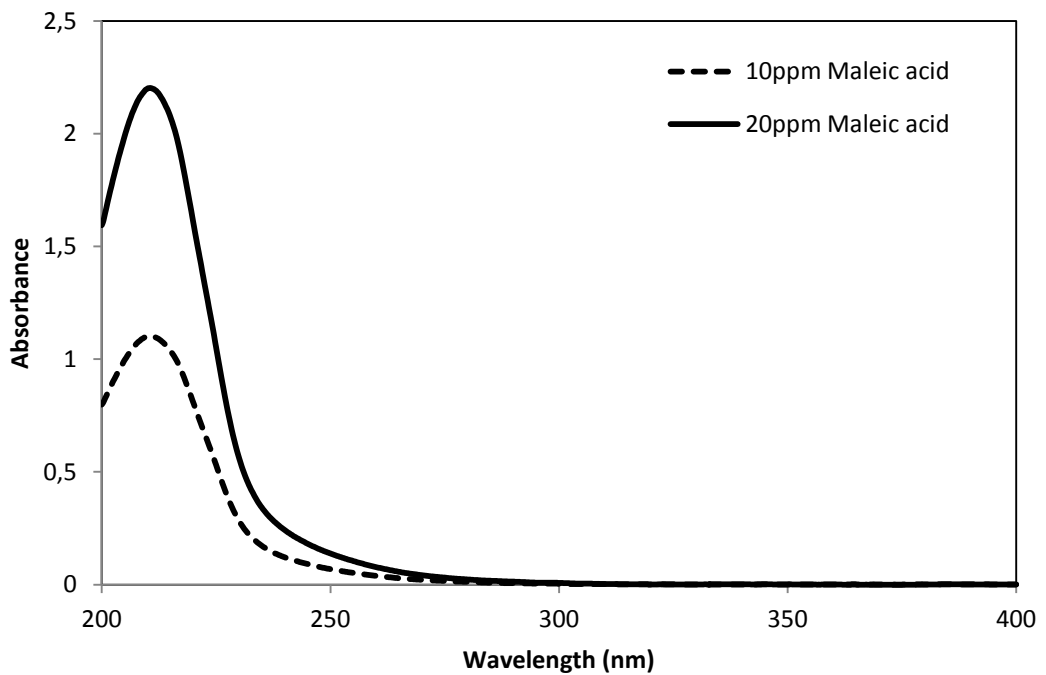


Figure 69: 10, 20ppm aqueous maleic acid solutions' UV-Vis spectrum

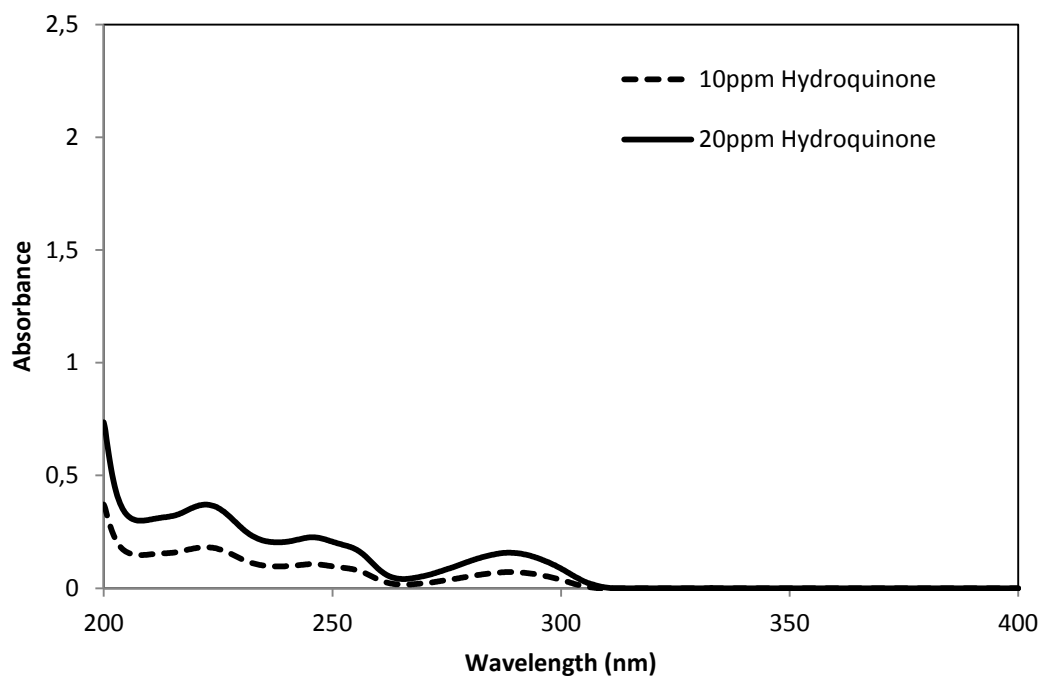


Figure 70: 10, 20ppm aqueous hydroquinone solutions' UV-Vis spectrum

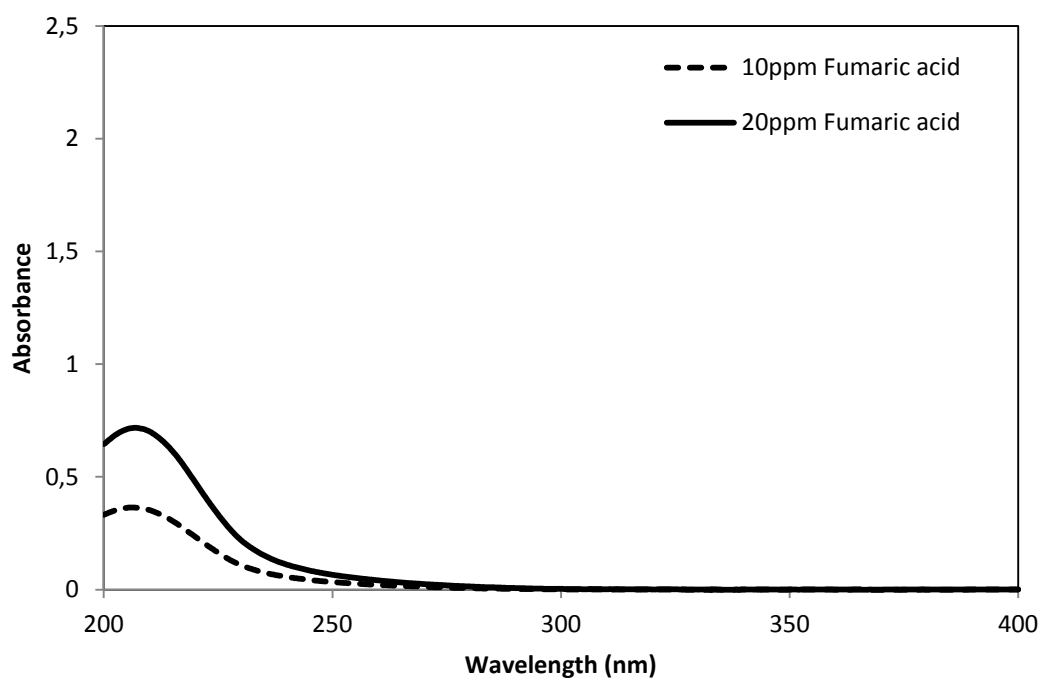


Figure 71: 10, 20ppm aqueous fumaric acid solutions' UV-Vis spectrum

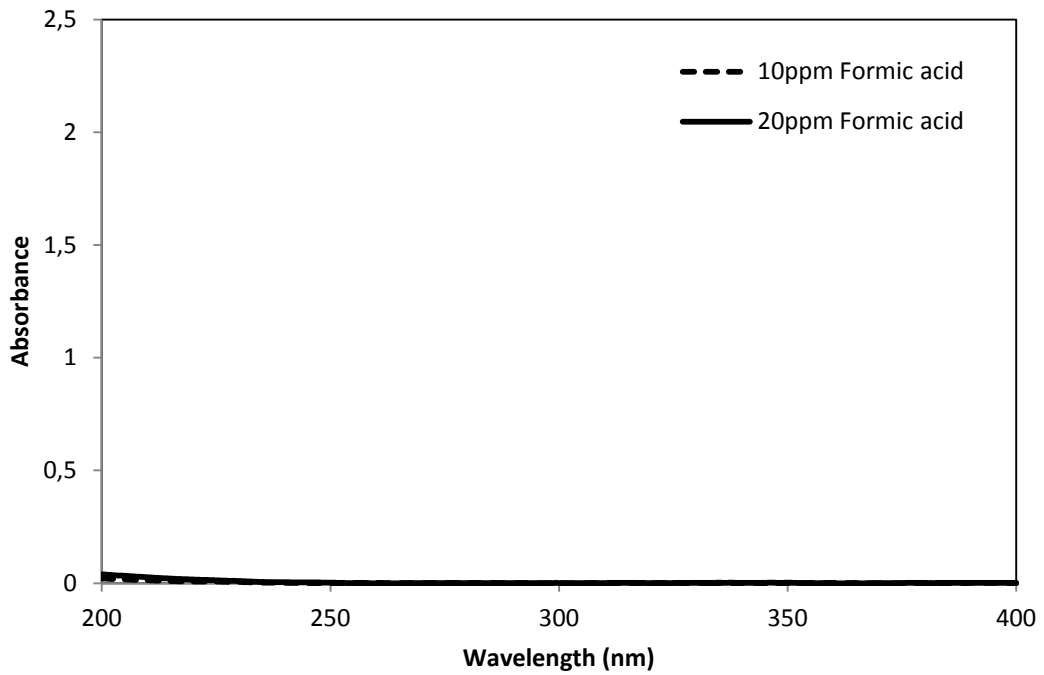


Figure 72: 10, 20ppm aqueous formic acid solutions' UV-Vis spectrum

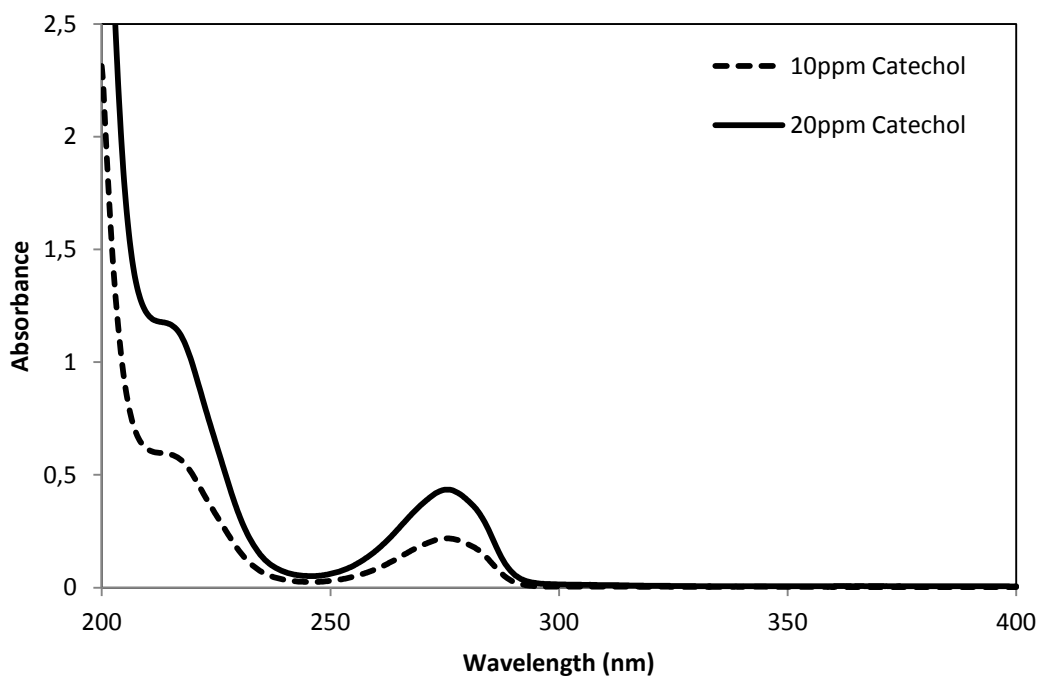


Figure 73: 10, 20ppm aqueous catechol solutions' UV-Vis spectrum

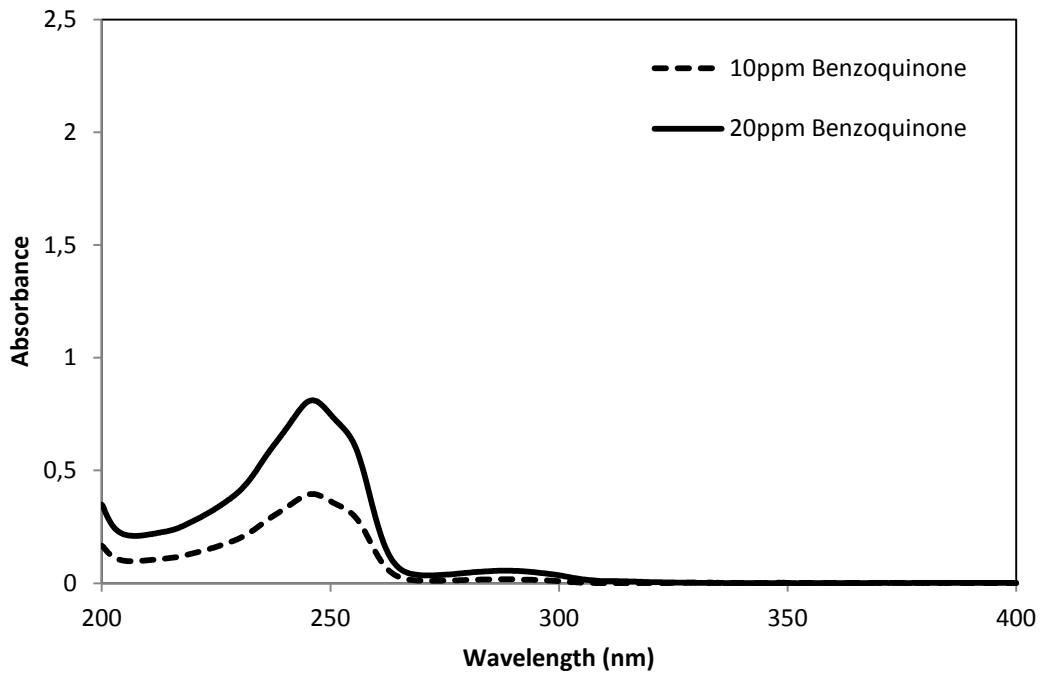


Figure 74: 10, 20ppm aqueous benzoquinone solutions' UV-Vis spectrum

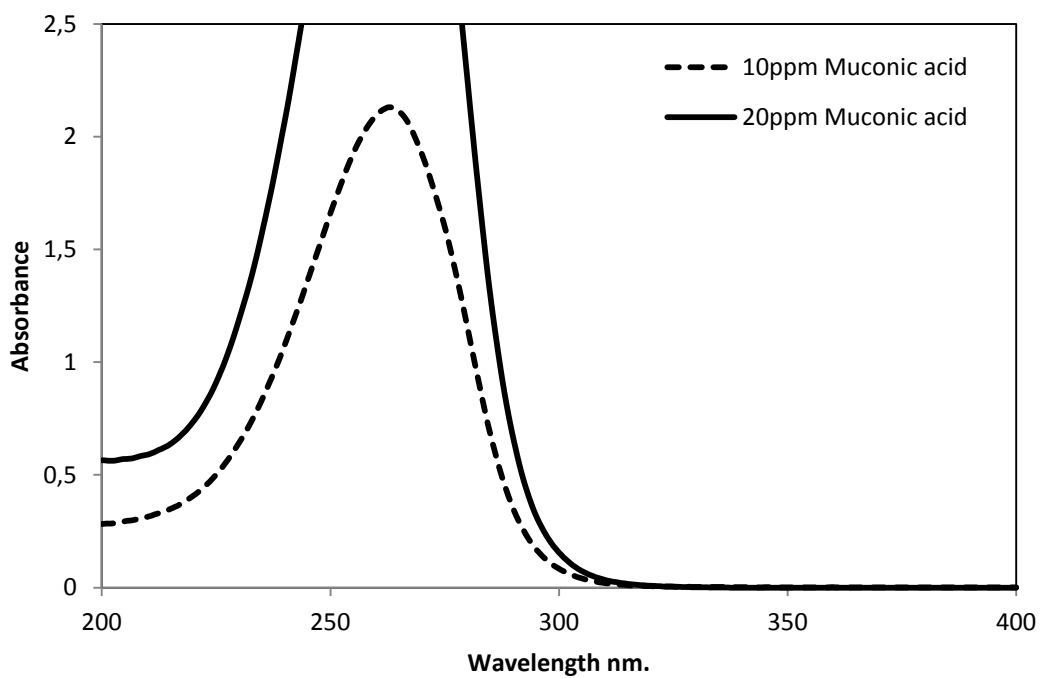


Figure 75: 10, 20ppm aqueous muconic acid solutions' UV-Vis spectrum

Below absorbance formula according to the concentrations of each species is presented:

Phenol

| | | | |
|-------|---|--------|---------------------|
| 270 | : | 0.0158 | C_{Phenol} |
| 271.5 | : | 0.0150 | C_{Phenol} |
| 264 | : | 0.0124 | C_{Phenol} |
| 289 | : | 0.0002 | C_{phenol} |
| 222.5 | : | 0.0328 | C_{Phenol} |
| 207 | : | 0.0603 | C_{Phenol} |
| 211 | : | 0.0624 | C_{Phenol} |
| 246 | : | 0.0018 | C_{Phenol} |

Benzoquinone

| | | | |
|-------|---|--------|---------------------------|
| 270 | : | 0.0018 | $C_{\text{Benzoquinone}}$ |
| 271.5 | : | 0.0018 | $C_{\text{Benzoquinone}}$ |
| 264 | : | 0.0045 | $C_{\text{Benzoquinone}}$ |
| 289 | : | 0.0028 | $C_{\text{Benzoquinone}}$ |
| 222.5 | : | 0.0151 | $C_{\text{Benzoquinone}}$ |
| 207 | : | 0.0105 | $C_{\text{Benzoquinone}}$ |
| 211 | : | 0.0109 | $C_{\text{Benzoquinone}}$ |
| 246 | : | 0.0406 | $C_{\text{Benzoquinone}}$ |

Catechol

| | | | |
|-------|---|--------|-----------------------|
| 270 | : | 0.0185 | C_{Catechol} |
| 271.5 | : | 0.0198 | C_{Catechol} |
| 264 | : | 0.0121 | C_{Catechol} |
| 289 | : | 0.0043 | C_{Catechol} |
| 222.5 | : | 0.0404 | C_{Catechol} |
| 207 | : | 0.0705 | C_{Catechol} |
| 211 | : | 0.0596 | C_{Catechol} |
| 246 | : | 0.0026 | C_{Catechol} |

Fumaric Acid

| | | | |
|-------|---|--------|---------------------------|
| 270 | : | 0.0013 | $C_{\text{Fumaric Acid}}$ |
| 271.5 | : | 0.0012 | $C_{\text{Fumaric Acid}}$ |
| 264 | : | 0.0017 | $C_{\text{Fumaric Acid}}$ |
| 289 | : | 0.0004 | $C_{\text{Fumaric Acid}}$ |
| 222.5 | : | 0.0202 | $C_{\text{Fumaric Acid}}$ |
| 207 | : | 0.0359 | $C_{\text{Fumaric Acid}}$ |
| 211 | : | 0.0345 | $C_{\text{Fumaric Acid}}$ |
| 246 | : | 0.0041 | $C_{\text{Fumaric Acid}}$ |

Hydroquinone

| | | | |
|-------|---|--------|---------------------------|
| 270 | : | 0.0027 | C _{Hydroquinone} |
| 271.5 | : | 0.0031 | C _{Hydroquinone} |
| 264 | : | 0.0022 | C _{Hydroquinone} |
| 289 | : | 0.0079 | C _{Hydroquinone} |
| 222.5 | : | 0.0186 | C _{Hydroquinone} |
| 207 | : | 0.0151 | C _{Hydroquinone} |
| 211 | : | 0.0154 | C _{Hydroquinone} |
| 246 | : | 0.0113 | C _{Hydroquinone} |

Maleic Acid

| | | | |
|-------|---|--------|--------------------------|
| 270 | : | 0.0021 | C _{Maleic Acid} |
| 271.5 | : | 0.0019 | C _{Maleic Acid} |
| 264 | : | 0.0031 | C _{Maleic Acid} |
| 289 | : | 0.0007 | C _{Maleic Acid} |
| 222.5 | : | 0.0667 | C _{Maleic Acid} |
| 207 | : | 0.1053 | C _{Maleic Acid} |
| 211 | : | 0.1101 | C _{Maleic Acid} |
| 246 | : | 0.0086 | C _{Maleic Acid} |

Muconic Acid

| | | | |
|-------|---|--------|---------------------------|
| 270 | : | 0.1923 | C _{Muconic Acid} |
| 271.5 | : | 0.1837 | C _{Muconic Acid} |
| 264 | : | 0.2135 | C _{Muconic Acid} |
| 289 | : | 0.0397 | C _{Muconic Acid} |
| 222.5 | : | 0.0456 | C _{Muconic Acid} |
| 207 | : | 0.0305 | C _{Muconic Acid} |
| 211 | : | 0.0327 | C _{Muconic Acid} |
| 246 | : | 0.1421 | C _{Muconic Acid} |

Oxalic Acid

| | | | |
|-------|---|--------|--------------------------|
| 270 | : | 0.0003 | C _{Oxalic Acid} |
| 271.5 | : | 0.0003 | C _{Oxalic Acid} |
| 264 | : | 0.0003 | C _{Oxalic Acid} |
| 289 | : | 0.0002 | C _{Oxalic Acid} |
| 222.5 | : | 0.0008 | C _{Oxalic Acid} |
| 207 | : | 0.0025 | C _{Oxalic Acid} |
| 211 | : | 0.0019 | C _{Oxalic Acid} |
| 246 | : | 0.0004 | C _{Oxalic Acid} |

Those formulas are gathered according to the same wavelength and eight different equations were obtained:

General Formula:

$$A_{\text{Total}} = A_{\text{Phenol}} + A_{\text{Benzoquinone}} + A_{\text{Catechol}} + A_{\text{Fumaric Acid}} + A_{\text{Hydroquinone}} + A_{\text{Maleic Acid}} + A_{\text{Oxalic Acid}} + A_{\text{Muconic Acid}}$$

270 nm

$$A = 0.0158 C_{\text{Phenol}} + 0.0018 C_{\text{Benzoquinone}} + 0.0185 C_{\text{Catechol}} + 0.0013 C_{\text{Fumaric Acid}} + 0.0027 C_{\text{Hydroquinone}} + 0.0021 C_{\text{Maleic Acid}} + 0.0003 C_{\text{Oxalic Acid}} + 0.1923 C_{\text{Muconic Acid}}$$

271.5 nm

$$A = 0.0150 C_{\text{Phenol}} + 0.0018 C_{\text{Benzoquinone}} + 0.0198 C_{\text{Catechol}} + 0.0012 C_{\text{Fumaric Acid}} + 0.0031 C_{\text{Hydroquinone}} + 0.0019 C_{\text{Maleic Acid}} + 0.0003 C_{\text{Oxalic Acid}} + 0.1837 C_{\text{Muconic Acid}}$$

264 nm

$$A = 0.0124 C_{\text{Phenol}} + 0.0045 C_{\text{Benzoquinone}} + 0.0121 C_{\text{Catechol}} + 0.0017 C_{\text{Fumaric Acid}} + 0.0022 C_{\text{Hydroquinone}} + 0.0031 C_{\text{Maleic Acid}} + 0.0003 C_{\text{Oxalic Acid}} + 0.2135 C_{\text{Muconic Acid}}$$

289nm

$$A = 0.0002 C_{\text{phenol}} + 0.0028 C_{\text{Benzoquinone}} + 0.0043 C_{\text{Catechol}} + 0.0004 C_{\text{Fumaric Acid}} + 0.0079 C_{\text{Hydroquinone}} + 0.0007 C_{\text{Maleic Acid}} + 0.0002 C_{\text{Oxalic Acid}} + 0.0397 C_{\text{Muconic Acid}}$$

222.5 nm

$$A = 0.0328 C_{\text{Phenol}} + 0.0151 C_{\text{Benzoquinone}} + 0.0404 C_{\text{Catechol}} + 0.0202 C_{\text{Fumaric Acid}} + 0.0186 C_{\text{Hydroquinone}} + 0.0667 C_{\text{Maleic Acid}} + 0.0008 C_{\text{Oxalic Acid}} + 0.0456 C_{\text{Muconic Acid}}$$

207 nm

$$A = 0.0603 C_{\text{Phenol}} + 0.0105 C_{\text{Benzoquinone}} + 0.0705 C_{\text{Catechol}} + 0.0359 C_{\text{Fumaric Acid}} + 0.0151 C_{\text{Hydroquinone}} + 0.1053 C_{\text{Maleic Acid}} + 0.0025 C_{\text{Oxalic Acid}} + 0.0305 C_{\text{Muconic Acid}}$$

211 nm

$$A = 0.0624 C_{\text{Phenol}} + 0.0109 C_{\text{Benzoquinone}} + 0.0596 C_{\text{Catechol}} + 0.0345 C_{\text{Fumaric Acid}} + 0.0154 C_{\text{Hydroquinone}} + 0.1101 C_{\text{Maleic Acid}} + 0.0019 C_{\text{Oxalic Acid}} + 0.0327 C_{\text{Muconic Acid}}$$

246 nm

$$A = 0.0018 C_{\text{Phenol}} + 0.0406 C_{\text{Benzoquinone}} + 0.0026 C_{\text{Catechol}} + 0.0041 C_{\text{Fumaric Acid}} + 0.0113 C_{\text{Hydroquinone}} + 0.0086 C_{\text{Maleic Acid}} + 0.0004 C_{\text{Oxalic Acid}} + 0.1421 C_{\text{Muconic Acid}}$$

APPENDIX B

TABULATED RESULTS OF EACH RUN

Table 15: Calculated amounts of species formed during phenol mineralization reaction with TiO₂ calcined at 500°C

| T500 | | | | | | | | |
|--------------|------|------|------|------|------|------|------|------|
| Time(min) | 0 | 30 | 60 | 90 | 120 | 180 | 240 | 300 |
| Phenol | 20.0 | 19.8 | 17.6 | 16.8 | 15.9 | 13.9 | 12.2 | 10.6 |
| Catechol | ND | ND | ND | ND | ND | ND | ND | ND |
| Hydroquinone | ND | ND | 0.1 | 0.4 | 0.6 | 1.0 | 1.2 | 1.3 |
| Benzoquinone | ND | 0.04 | ND | ND | 0.02 | ND | 0.01 | 0.06 |
| Muconic Acid | ND | ND | 0.02 | 0.02 | 0.02 | 0.02 | 0.04 | 0.03 |
| Maleic Acid | ND | 0.08 | 0.22 | 0.19 | 0.04 | 0.04 | 0.17 | 0.05 |
| Fumaric Acid | ND | ND | ND | ND | ND | ND | ND | ND |
| Formic Acid | ND | ND | ND | ND | ND | ND | ND | ND |
| Oxalic Acid | ND | 3.7 | 2.7 | 3.3 | 4.7 | 2.9 | ND | ND |

Table 16: Calculated amounts of species formed during phenol mineralization reaction with 1%Pr-TiO₂ calcined at 500°C

| P500 | | | | | | | | |
|--------------|------|------|------|------|------|------|------|------|
| Time(min) | 0 | 30 | 60 | 90 | 120 | 180 | 240 | 300 |
| Phenol | 20.0 | 19.5 | 16.9 | 15.6 | 14.7 | 12.7 | 10.8 | 9.0 |
| Catechol | ND | ND | ND | ND | ND | ND | ND | ND |
| Hydroquinone | ND | 2.8 | 3.4 | 3.8 | 4.2 | 6.1 | 6.5 | 7.7 |
| Benzoquinone | ND | ND | ND | ND | ND | ND | ND | ND |
| Muconic Acid | ND | 0.07 | 0.10 | 0.11 | 0.11 | 0.14 | 0.16 | 0.18 |
| Maleic Acid | ND | 0.36 | 0.54 | 0.58 | 0.55 | 0.54 | 0.63 | 0.63 |
| Fumaric Acid | ND | ND | ND | ND | ND | ND | ND | ND |
| Formic Acid | ND | ND | ND | ND | ND | ND | ND | ND |
| Oxalic Acid | ND | 9.8 | 8.2 | 9.8 | 10.2 | 12.2 | 9.2 | 8.8 |

Table 17: Calculated amounts of species formed during phenol mineralization reaction with TiO₂ calcined at 600°C

| T600 | | | | | | | | |
|--------------|------|------|------|------|------|------|------|------|
| Time(min) | 0 | 30 | 60 | 90 | 120 | 180 | 240 | 300 |
| Phenol | 20.0 | 20.7 | 19.0 | 18.6 | 17.8 | 16.5 | 15.2 | 13.6 |
| Catechol | ND | ND | ND | ND | ND | ND | ND | ND |
| Hydroquinone | ND | ND | ND | ND | ND | ND | ND | ND |
| Benzoquinone | ND | 0.8 | 1.0 | 1.5 | 1.8 | 2.1 | 2.6 | 2.5 |
| Muconic Acid | ND | ND | 0.01 | 0.03 | 0.06 | 0.10 | 0.14 | 0.18 |
| Maleic Acid | ND | ND | ND | ND | ND | 0.01 | 0.03 | 0.28 |
| Fumaric Acid | ND | ND | ND | ND | ND | ND | ND | ND |
| Formic Acid | ND | ND | ND | ND | ND | ND | ND | ND |
| Oxalic Acid | ND | 6.9 | 6.0 | 5.5 | 9.3 | 8.2 | 12.8 | 10.3 |

Table 18: Calculated amounts of species formed during phenol mineralization reaction with 1%Pr-TiO₂ calcined at 600°C

| P600 | | | | | | | | |
|--------------|------|------|------|------|------|------|------|------|
| Time(min) | 0 | 30 | 60 | 90 | 120 | 180 | 240 | 300 |
| Phenol | 20.0 | 15.9 | 14.0 | 12.6 | 11.5 | 8.8 | 6.6 | 4.4 |
| Catechol | ND | ND | ND | ND | ND | ND | ND | ND |
| Hydroquinone | ND | 0.14 | 0.13 | 0.12 | 0.15 | 0.05 | 0.03 | ND |
| Benzoquinone | ND | ND | ND | ND | ND | ND | ND | ND |
| Muconic Acid | ND | ND | ND | ND | ND | ND | ND | ND |
| Maleic Acid | ND | 1.14 | 1.07 | 1.00 | 0.89 | 0.80 | 0.60 | 0.56 |
| Fumaric Acid | ND | ND | ND | ND | ND | ND | ND | ND |
| Formic Acid | ND | ND | ND | ND | ND | ND | ND | ND |
| Oxalic Acid | ND | 7.4 | 6.2 | 5.1 | 3.9 | 4.5 | 4.9 | 5.9 |

Table 19: Calculated amounts of species formed during phenol mineralization reaction with TiO₂ calcined at 650°C

| T650 | | | | | | | | |
|--------------|------|------|------|------|------|------|------|------|
| Time(min) | 0 | 30 | 60 | 90 | 120 | 180 | 240 | 300 |
| Phenol | 20.0 | 19.7 | 17.9 | 17.0 | 16.0 | 14.5 | 13.0 | 11.4 |
| Catechol | ND | ND | ND | ND | ND | ND | ND | ND |
| Hydroquinone | ND | 1.1 | 1.5 | 1.9 | 2.1 | 2.4 | 2.4 | 2.2 |
| Benzoquinone | ND | ND | ND | ND | ND | ND | ND | ND |
| Muconic Acid | ND | 0.02 | 0.08 | 0.10 | 0.12 | 0.19 | 0.24 | 0.30 |
| Maleic Acid | ND | ND | 0.07 | 0.10 | 0.19 | 0.41 | 0.57 | 0.88 |
| Fumaric Acid | ND | ND | ND | ND | ND | ND | ND | ND |
| Formic Acid | ND | ND | ND | ND | ND | ND | ND | ND |
| Oxalic Acid | ND | 17.3 | 17.7 | 19.9 | 22.2 | 19.0 | 19.8 | 18.2 |

Table 20: Calculated amounts of species formed during phenol mineralization reaction with 1%Pr-TiO₂ calcined at 650°C

| P650 | | | | | | | | |
|--------------|------|------|------|------|------|------|------|------|
| Time(min) | 0 | 30 | 60 | 90 | 120 | 180 | 240 | 300 |
| Phenol | 20.0 | 19.1 | 17.3 | 15.9 | 14.7 | 12.4 | 11.2 | 9.2 |
| Catechol | ND | ND | ND | ND | ND | ND | ND | ND |
| Hydroquinone | ND | 3.9 | 4.9 | 6.5 | 7.4 | 8.1 | 7.4 | 8.1 |
| Benzoquinone | ND | ND | ND | ND | ND | ND | ND | ND |
| Muconic Acid | ND | 0.05 | 0.07 | 0.09 | 0.10 | 0.14 | 0.11 | 0.14 |
| Maleic Acid | ND | 0.12 | 0.20 | 0.28 | 0.30 | 0.56 | 0.45 | 0.62 |
| Fumaric Acid | ND | ND | ND | ND | ND | ND | ND | ND |
| Formic Acid | ND | ND | ND | ND | ND | ND | ND | ND |
| Oxalic Acid | ND | 7.5 | 6.4 | 5.4 | 3.0 | 3.5 | 3.8 | 2.8 |

APPENDIX C

ANALYSIS OF REACTION TEST RESULTS IN TERMS OF REACTION RATE

Table 21: $-\ln(C/C_0)$ vs. time data for phenol

| Time(min) | 0 | 30 | 60 | 90 | 120 | 180 | 240 | 300 |
|--------------------------------------|---|-------|-------|-------|-------|-------|-------|--------|
| TiO ₂ calc. at 500°C | 0 | 0.010 | 0.128 | 0.174 | 0.229 | 0.364 | 0.494 | 0.635 |
| TiO ₂ calc. at 600°C | 0 | 0 | 0.051 | 0.073 | 0.117 | 0.192 | 0.274 | 0.386 |
| TiO ₂ calc. at 650°C | 0 | 0.015 | 0.111 | 0.163 | 0.223 | 0.322 | 0.431 | 0.562 |
| 1%Pr-TiO ₂ calc. at 500°C | 0 | 0.025 | 0.168 | 0.248 | 0.308 | 0.454 | 0.616 | 0.799 |
| 1%Pr-TiO ₂ calc. at 600°C | 0 | 0.229 | 0.357 | 0.462 | 0.553 | 0.821 | 1.109 | 1.5140 |
| 1%Pr-TiO ₂ calc. at 650°C | 0 | 0.046 | 0.145 | 0.229 | 0.308 | 0.478 | 0.580 | 0.777 |

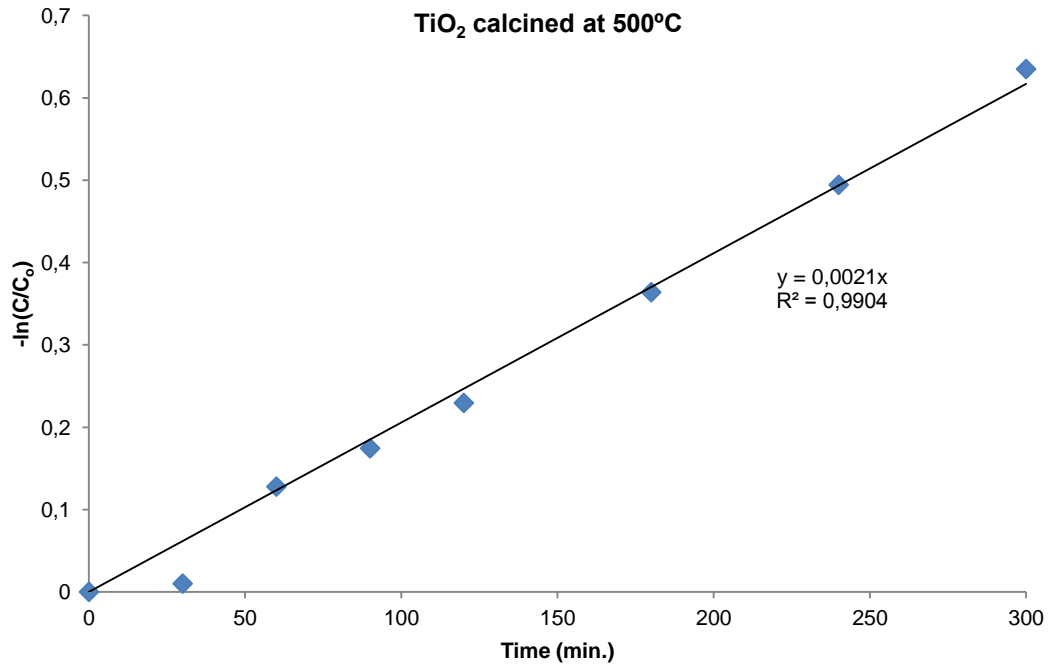


Figure 76: $-\ln(C/C_0)$ vs. time graph for phenol of TiO₂ calcined at 500°C

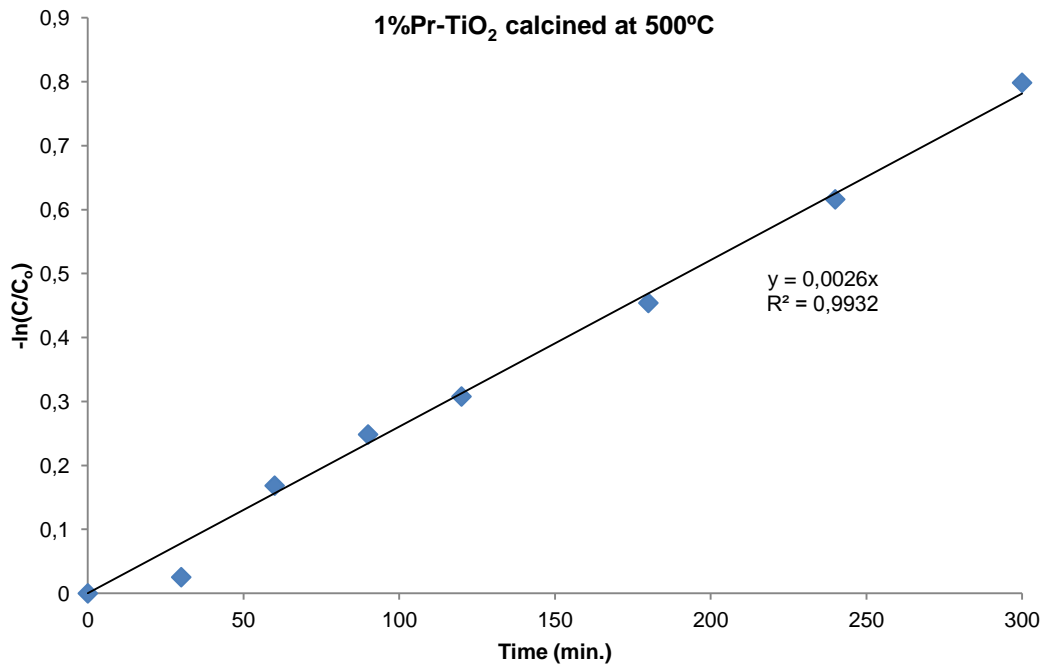


Figure 77: $-\ln(C/C_0)$ vs. time graph for phenol of 1%Pr-TiO₂ calcined at 500°C

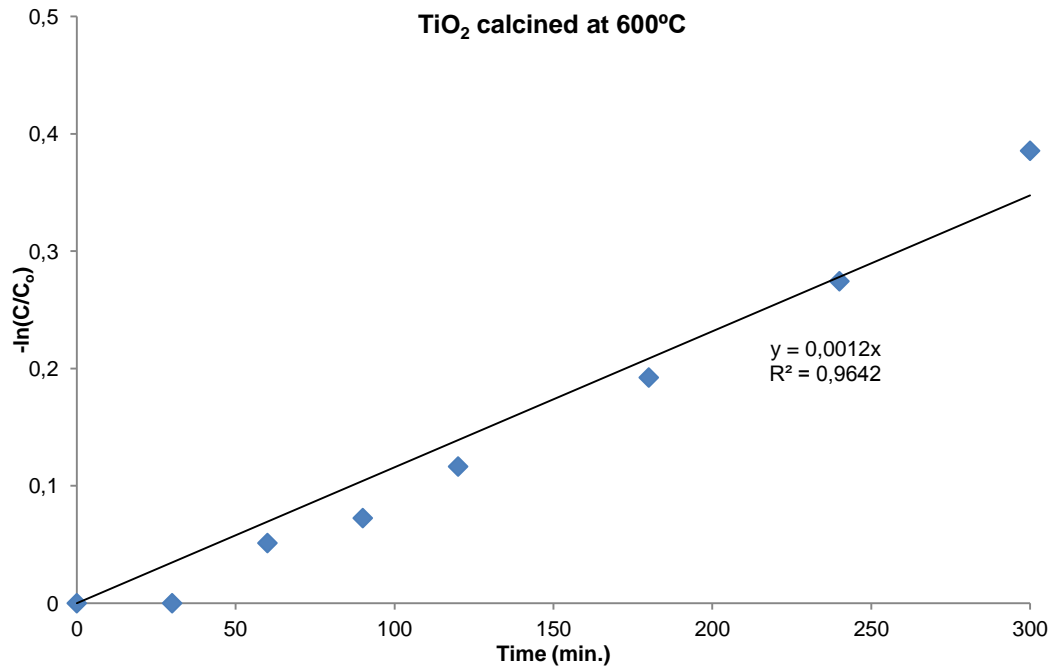


Figure 78: $-\ln(C/C_0)$ vs. time graph for phenol of TiO₂ calcined at 600°C

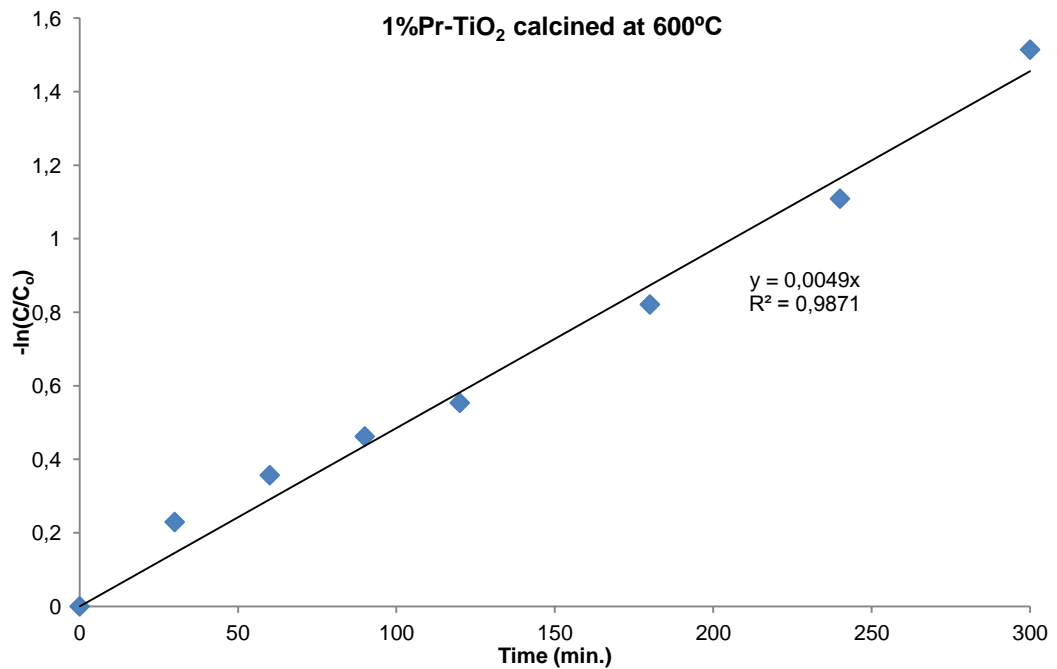


Figure 79: $-\ln(C/C_0)$ vs. time graph for phenol of 1%Pr-TiO₂ calcined at 600°C

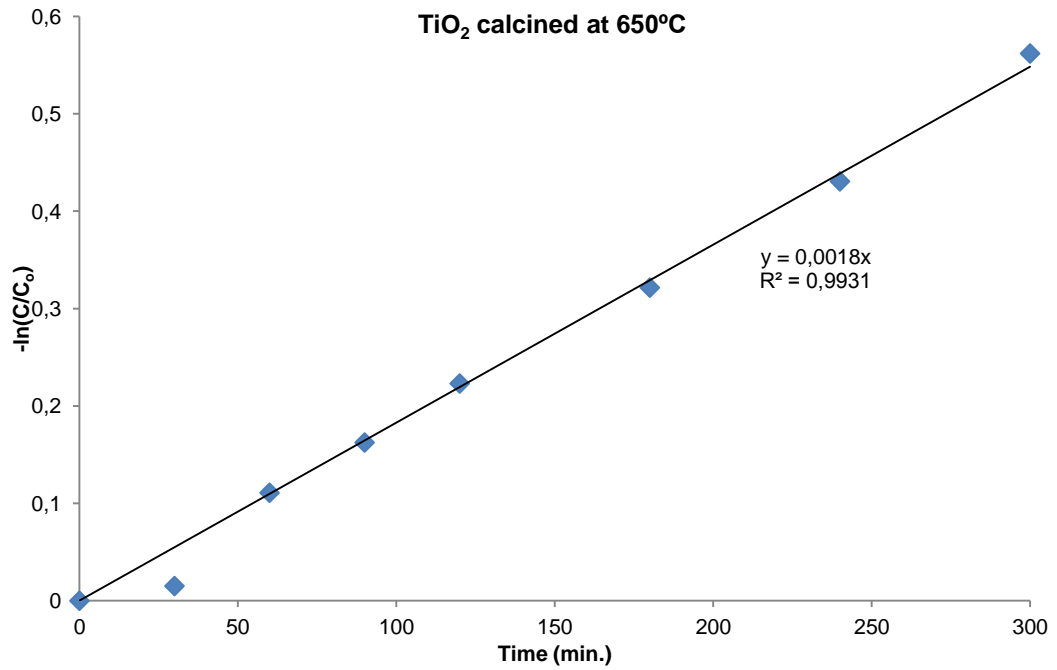


Figure 80: $-\ln(C/C_0)$ vs. time graph for phenol of TiO₂ calcined at 650°C

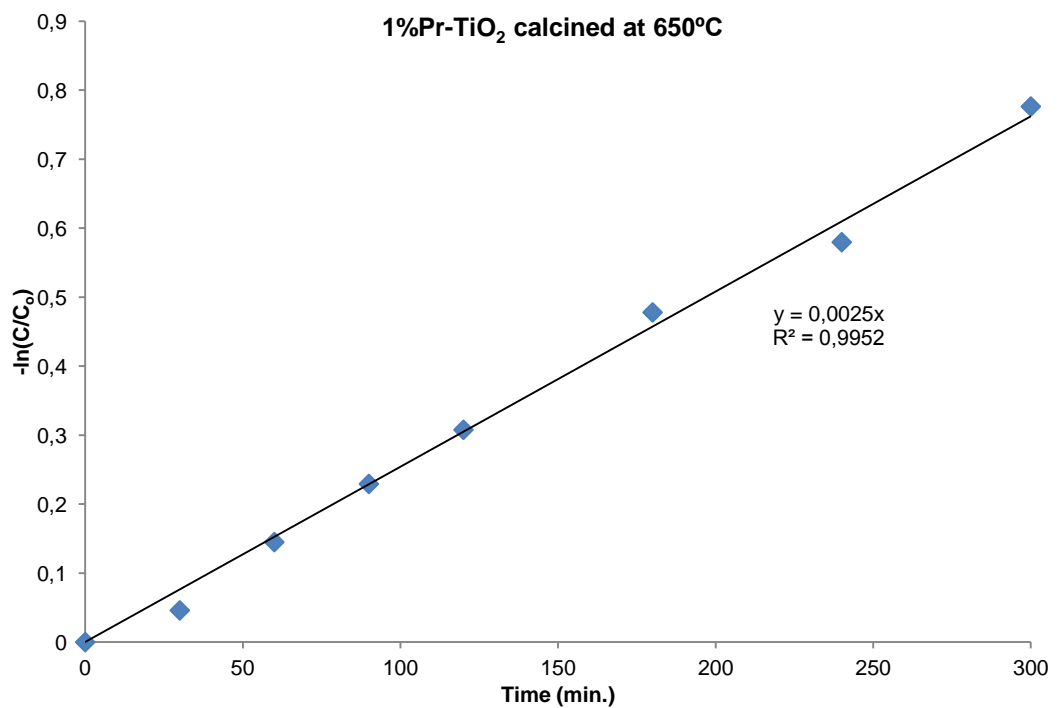


Figure 81: $-\ln(C/C_0)$ vs. time graph for phenol of 1%Pr-TiO₂ calcined at 650°C

CURRICULUM VITAE

PERSONAL INFORMATION

Surname, Name: Dođu, Doruk

Nationality: Turkish (TC)

Date and Place of Birth: 26 November 1980, Ankara

Marital Status: Married

Phone: +90 312 210 43 55

E-mail: dorukd@gmail.com

EDUCATION

| Degree | Institution | Year of Graduation |
|---------------|----------------------------------|---------------------------|
| MS | METU Metallurgical and Mat. Eng. | 2005 |
| BS | METU Metallurgical and Mat. Eng. | 2002 |
| High School | METU D.F. Private High School | 1998 |

WORK EXPERIENCE

| Year | Place | Enrollment |
|-------------|----------------------------------|--------------------|
| 2009-cont. | Vestel Defence Industry | R&D Engineer |
| 2002-2009 | METU Metallurgical and Mat. Eng. | Research Assistant |
| 2001 July | TUBITAK Marmara Research Center | Trainee |
| 2000 July | Turkish Aerospace Industry | Trainee |

IN PREPARATION PUBLICATIONS

1. D. Doğu, B. Ögel, G. Karakaş, "Photocatalytic properties of praseodymium doped titanium dioxide"

PUBLICATIONS/PRESENTATIONS:

1. D. Doğu, G. Karakaş, "Photocatalytic Properties of Pr Doped TiO₂", 4th National Catalysis Conference, March 2012, Kocaeli, Turkey.
2. A.D. Deniz, D. Doğu, İ. Pamuk, "Hydrogen Production by Reforming of JP-8 Fuel for Auxilary Power Unit Developed for Military Vehicles", 5th Defence Technologies Conference, June 2010, Ankara, Turkey.
3. F. Şen, D. Doğu, S. Aksongur, M.D. Mat, "Current Collector Materials for Solid Oxide Fuel Cells", 5th Defence Technologies Conference, June 2010, Ankara, Turkey.
4. D. Doğu, G. Karakaş, "Effects of Doping Photocatalytic TiO₂ with Photon Up-Conversion Nanocrystals of Pr", 3rd National Catalysis Conference, April 2010, Zonguldak, Turkey.
5. A.D. Deniz, D. Doğu, "Reforming JP-8 to Produce Hydrogen for Solid Oxide Fuel Cells", 3rd National Catalysis Conference, April 2010, Zonguldak, Turkey.
6. A.D. Deniz, D. Doğu, "Producing Hydrogen for Solid Oxide Fuel Cells by Steam Reforming of JP-8 Fuel", 6th East Mediterranean Chemical Engineering Conference, March 2010, Antalya, Turkey.
7. D. Doğu, G. Karakaş, "Effect of Doping Titania with Praseodymium", 6th East Mediterranean Chemical Engineering Conference, March 2010, Antalya, Turkey.
8. D. Doğu, B. Korkmaz Erdural, G. Karakaş, "Impoving the Photocatalytic Activity of TiO₂ by Photon Up-Conversion", 2nd National Catalysis Conference, June 2008, Erzurum, Turkey.